PHYSICAL LAYER SOLUTIONS FOR ULTRA-BROADBAND WIRELESS COMMUNICATIONS IN THE TERAHERTZ BAND

A Dissertation
Presented to
The Academic Faculty

By

Chong Han

In Partial Fulfillment
of the Requirements for the Degree
Doctor of Philosophy
in
Electrical and Computer Engineering

School of Electrical and Computer Engineering
Georgia Institute of Technology
May 2016

PHYSICAL LAYER SOLUTIONS FOR ULTRA-BROADBAND WIRELESS COMMUNICATIONS IN THE TERAHERTZ BAND

Approved by:

Dr. Ian F. Akyildiz, Advisor
Ken Byers Chair Professor, School of Electrical and Computer Engineering
Georgia Institute of Technology

Dr. Raghupathy Sivakumar
Wayne J. Holman Chair Professor, School of Electrical and Computer Engineering
Georgia Institute of Technology

Dr. Geoffrey Ye Li
Professor, School of Electrical and Computer Engineering
Georgia Institute of Technology

Dr. Josep Miquel Jornet
Assistant Professor, Department of Electrical Engineering
University at Buffalo, The State University of New York

Dr. Mary Ann Weitnauer
Professor, School of Electrical and Computer Engineering
Georgia Institute of Technology

Date Approved: March 10, 2016

To my family, for their endless love, support and encouragement.

ACKNOWLEDGMENT

I would like to express my deepest gratitude to my advisor, Dr. Ian F. Akyildiz, for giving me the life-reshaping opportunity to work under his supervision, as well as his trust, support and encouragement throughout my entire Ph.D.. I am also thankful to him for his passion and enthusiasm, which guided me to steadily advance towards the successful completion of this thesis, and inspired me to embrace for my career. I also greatly appreciate Dr. Akyildiz to be my mentor, whose precious life lessons to me will guide me and influence me throughout my whole life.

I would also like to express my appreciation to all the academic members of the School of Electrical and Computer Engineering at the Georgia Institute of Technology for their helpful and critical reviews throughout the Ph.D. program. Special thanks go to Dr. Geoffrey Ye Li and Dr. Mary Ann Weitnauer, who provided me valuable and constructive suggestions on my work, and also kindly serve in my Ph.D. Defense Reading Committee. Moreover, I am thankful to Dr. Josep Miquel Jornet (from SUNY Buffalo) and Dr. Raghupathy Sivakumar who kindly serve in my Ph.D. Defense Committee. All of their valuable comments have helped me complete my Ph.D. and achieve a solid research path towards this thesis.

I would also like to thank all current and former members of the Broadband Wireless Networking (BWN) Lab, for their constant support and true friendship since the very beginning. I keep a vivid memory of all my days in the lab and all the fantastic people that I have met throughout these years. To all of you, thank you for the unique atmosphere we have had in the lab.

I cannot find the words to express my gratitude to my family, and in particular my parents and my wife. This achievement would have not been possible without their love, support and encouragement.

SUMMARY

In recent years, the wireless data traffic grew exponentially, which was further accompanied by an increasing demand for higher data rates. Towards this aim, Terahertz band (0.1-10 THz) communication is envisioned as one of the key wireless technologies of the next decade. The THz band will help to overcome the spectrum scarcity problems and capacity limitations of current wireless networks, by providing an unprecedentedly large bandwidth. In addition, THz band communication will enable a plethora of long-awaited applications ranging from instantaneous massive data transfer among nearby devices in ultra-high-speed wireless personal and local area networks, to ultra-high-definition content streaming over mobile devices in 5G and beyond small cells.

The objective of the thesis is to establish the physical layer foundations of the ultra-broadband communication in the THz band. First, a unified multi-path propagation channel is modeled in the THz band, based on ray-tracing techniques. The wideband characterization are analyzed, which include the distance-varying spectral windows, the delay spread, the wideband capacity and the temporal broadening effects. Second, a multi-wideband waveform design for the THz band is proposed to improve the distance and support ultra-high-speed transmissions. Third, two algorithms for timing acquisition in the pulse-based wireless systems are developed, namely the low-sampling-rate (LSR) algorithm, and the maximum likelihood (ML)-based approach. Fourth, the distance-aware bandwidth resource allocation schemes for the single-user and multi-user THz band networks are developed. Fifth, a three-dimensional (3-D) end-to-end model is developed and characterized, which includes the responses of the graphene-based reflectarray antenna and the 3-D multi-path propagation. The provided physical layer analysis in this thesis lays out the foundation for reliable and efficient ultra-high-speed wireless communications in the THz band.

TABLE OF CONTENTS

LIST OF FIGURES

CHAPTER 1

INTRODUCTION

Over the last decade, wireless data traffic has drastically grown due to a change in the way today's society creates, shares and consumes information. This change has been accompanied by an increasing demand for higher speed wireless communications anywhere, anytime. Following this trend, wireless ultra-broadband links at 100 Giga-bit-per-second (Gbps) or even Terabit-per-second (Tbps) are expected to become a reality within five to ten years. Advanced physical layer solutions and, more importantly, new spectral bands will be required to support this high data rate for future wireless communications. Amongst others, Terahertz band (0.1-10 THz) communication (see Fig. 1) is envisioned as a key wireless technology that can satisfy this demand [1, 2, 3, 4, 5, 6, 7, 8].

1.1 Motivation for THz Band Communications

Besides THz-band communication, several alternatives are currently being considered to meet this demand:

- In communication systems at frequencies below 5 GHz, advanced digital modulations and sophisticated communication schemes are being used to achieve very high spectral efficiencies. However, the scarcity of the available bandwidth limits the achievable data rates. For example, in Long-Term Evolution Advanced networks,

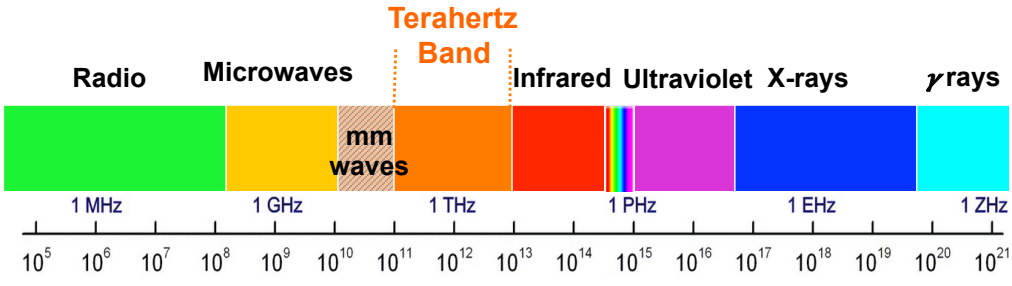

Figure 1. Terahertz band (0.1 - 10 THz) in the electromagnetic spectrum.

the peak data rates in the order of 1 Gbps are feasible over 100 MHz of aggregated bandwidth [9]. These are three orders of magnitude below the expected needs for Tbps links.

- Millimeter-wave communication systems, such as those at 60 GHz, have gained a lot of attention in the last few years due to their ability to support very high data rates, in the order of 10 Gbps, at the cost of a limited transmission distance [10]. The path to improve these data rates involves the development of more complex transceiver architectures able to implement physical layer solutions with much higher spectral efficiency. However, ultimately, the usable bandwidth is limited to be less than 10 GHz, which effectively poses an upper bound on the achievable data rates.

- Free Space Optical (FSO) communication systems, which operate at infrared (IR) frequencies and above, are being explored as a way to improve the achievable data rates in wireless networks. The intrinsically very large available bandwidth at such very high frequencies plays to their advantage. However, low transmission power budget due to the eye-safety limits, the impact of several atmospheric effects on the signal propagation (e.g., fog, rain, dust or pollution), and the size and need of strict alignment between transmitter and receiver [3], limit the achievable data rates [11] or the practicality [12] of FSO systems for mobile and personal wireless networks.

On the contrary, the THz band offers a much larger bandwidth, which ranges from tens of GHz up to several THz depending on the transmission distance [1]. The available bandwidth is more than one order of magnitude above state-of-art mm-wave systems, while the frequency of operation is at least one order of magnitude below that of FSO systems. The technology required to make THz band communication a reality is also rapidly advancing. In addition to all these reasons, the THz band is not yet regulated. In terms of broader impact, THz technology has been recently identified by DARPA as one of the four major research areas that could eventually have an impact on our society larger than the Internet

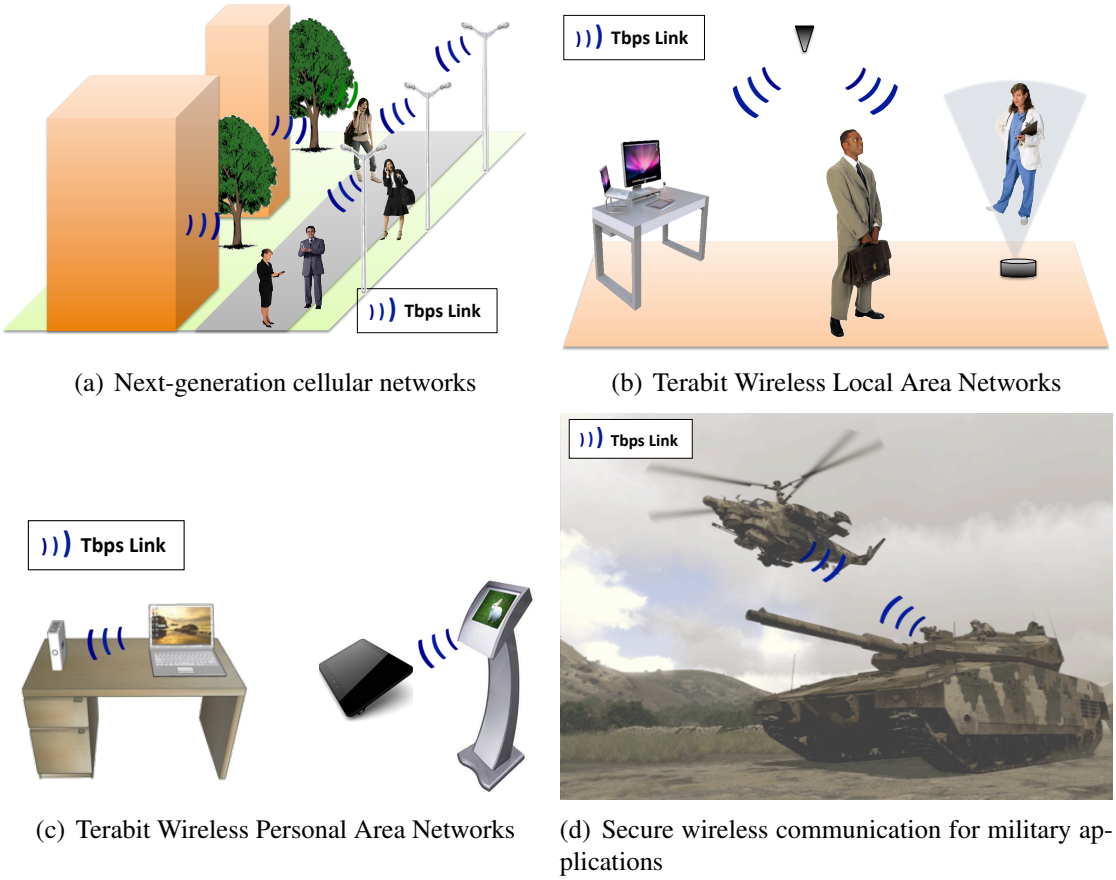

(a) Next-generation cellular networks

(b) Terabit Wireless Local Area Networks

(c) Terabit Wireless Personal Area Networks

(d) Secure wireless communication for military applications

Figure 2. Terahertz band applications at the macro-scale.

itself [13]. Therefore, it is the right time for the telecommunications community to jointly define and pave the way for the future of this novel communication paradigm.

1.2 Applications

The very large bandwidth provided by the THz band opens the door to a variety of applications which demand ultra-high data rates and allows the development of a plethora of novel applications in classical macro-scale networking scenarios as well as in new nano-scale communication paradigms. Some of these applications can already be foreseen and others will undoubtedly emerge as the technology progresses.

1.2.1 Macro-scale Applications

The envisioned applications of THz band communication at the macro-scale are, among others:

- **Next-geration Cellular Networks:** THz band communication can be used in next generation small cells, i.e., as a part of hierarchical cellular networks or heterogeneous networks [14]. The THz band will provide small cells with ultra-high-speed data communication within coverage areas of up to 10 meters. The operational environment of these small cells includes static and mobile users, both in indoor and outdoor scenarios. Specific applications are ultra-high-definition multimedia streaming to smartphones, or ultra-high-definition video conferencing (Figure 2(a)). In addition, directional THz band links can be used to provide an ultra-high-speed wireless backhaul to the small cells.

- **Terabit Wireless Local Area Networks (T-WLAN):** THz band communication enables the seamless interconnection between ultra-high-speed wired networks, e.g., fiber optical links, and personal wireless devices such as laptops and tablet-like devices (no speed difference between wireless and wired links). This will facilitate the use of bandwidth-intensive applications across static and mobile users, mainly in indoor scenarios. Some specific applications are high-definition holographic video conferencing (Figure 2(b)) or ultra-high-speed wireless data distribution in data centers [15, 16].

- **Terabit Wireless Personal Area Networks (T-WPAN):** Tbps links among devices in close proximity are possible with THz band communication. The operational environment is mainly indoor and usually on a desk. Specific applications include multimedia kiosks and ultra-high-speed data transfer between personal devices (Figure 2(c)). For example, to transfer the equivalent content of a blue-ray disk to a tablet-like device could take less than one second with a 1 Tbps link, boosting the

data-rates of existing technologies such as WiFi Direct, Apple Airplay or Miracast.

- **Secure Terabit Wireless Communication:** The THz band can also enable ultra-broadband secure communication links in the military and defense fields (Figure 2(d)). The very high atmospheric attenuation at THz band frequencies and the use of very large antenna arrays to overcome the limited communication distance result in very narrow, almost razor-sharp, beams, which drastically limit the eavesdropping probability. Spread spectrum techniques can also be used over the ultra-broad channel bandwidth to prevent and overcome common jamming attacks.

1.2.2 Nano-scale Applications

The THz band will also enable wireless communication among nanoscale machines or nanomachines, i.e., very small functional devices which are able to perform simple tasks at the nanoscale, such as computing, data storage, actuation or sensing. Each component of a nanomachine is up to a few hundred cubic nanometers in size, and the size of the entire device is in the order of a few cubic micrometers at most. The state of the art in nanoscale transceivers and antennas points to the THz band as their frequency range of operation [17, 18, 19, 20]. It is not that nanomachines are purposely developed to communicate in the Terahertz band, but the very small size and unique properties of nano-antennas and nano-transceivers enable nanomachines to communicate at this very high frequency. Some specific applications are:

- **Health Monitoring Systems:** Sodium, glucose and other ions in blood [21], cholesterol [22], cancer biomarkers [23] or the presence of different infectious agents [24] can be monitored by means of nanoscale sensors or nanosensors. Several nanosensors distributed around the body, defining a human body nanosensor network (Figure 3(a)), could be used to collect relevant data about the patient's health. A wireless interface between these nanosensors and a micro-device such as a cellphone or specialized medical equipment could be used to collect all these data and forward them

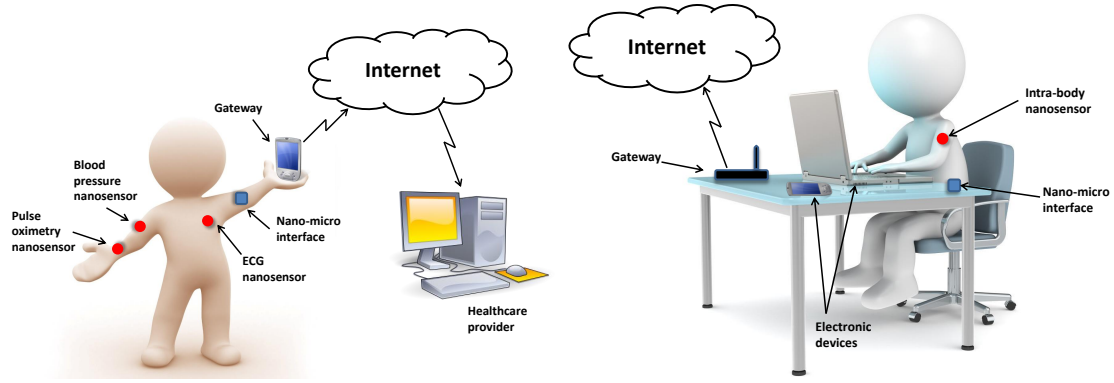

(a) Wireless Nano-Sensor Networks for health monitoring

(b) The Internet of Nano-Things

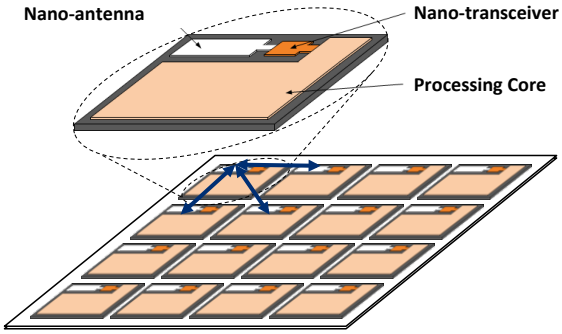

(c) Wireless on-chip communication

Figure 3. Terahertz band applications at the nano-scale.

to the healthcare provider.

- **Nuclear, Biological and Chemical Defenses:** Chemical and biological nanosensors can be used to detect harmful chemicals and biological weapons in a distributed manner. One of the main benefits of using nanosensors rather than classical chemical sensors is that the presence of a chemical composite can be detected in a concentration as low as one molecule and much faster than classical microscale sensors [17]. However, taking into account that these sensors need direct contact with the molecules, having a network with a very large number of nanosensor nodes becomes necessary. By means of distributed spectroscopy, a wireless nanosensor network will be able to converge the information of the molecular composition of the air in a specific location to a macro-device in a very short time.

- **The Internet of Nano-things:** The interconnection of nanoscale machines with existing communication networks and ultimately Internet defines a truly cyber-physical system which known as the Internet of Nano-Things (IoNT) [25]. The IoNT enables new interesting applications that will impact also in the way we work. For example, in an interconnected office (Figure 3(b)), a nano-transceiver and nano-antenna can be embedded in every single object to allow them to be permanently connected to the Internet. As a result, a user can keep track of all its professional and personal item in an effortless fashion.

- **Ultra-high-speed On-chip Communication:** The THz band can provide efficient and scalable means of inter-core communication in wireless on-chip networks [26], by using planar nano-antennas to create ultra-high-speed links (Figure 3(c)). This novel approach will expectedly fulfill the stringent requirements of the area-constraint and communication-intensive on-chip scenario by virtue of both its high bandwidth and extremely low area overhead. More importantly, the use of graphene-based THz band communication [27] would deliver inherent multicast and broadcast communication capabilities at the core level.

1.3 Challenges and Research Objectives

On the way to pave for the realization of THz band communications, there still exist research challenges from the communication perspectives that require innovative solutions and even the revision of well-established concepts in wireless communications [1]. As the focus of this thesis, one of the main challenges is imposed by the very high path loss at THz band frequencies, which poses a major constraint on the communication distance. Additional challenges range from the characterization of the frequency-selective path loss of the THz band channel, to the development of novel modulations, synchronization schemes, and resource allocation model tailored to the peculiarities of this paradigm. Many of these challenges are common but more difficult than mm-wave communication systems and as a

result, the solutions proposed in this thesis can also benefit those systems.

The objective of the thesis is to address these challenges and establish the physical layer foundations of the ultra-broadband wireless communication in the THz band. In the following, the challenges and developed solutions at the physical layer are overviewed.

1.3.1 Multi-path Channel Model

For the realization of optimal wireless communication networks in the THz band, it is imperative to develop a unified channel model which accurately characterizes the Terahertz spectrum peculiarities. The challenges and requirements to be addressed for the analysis and design of THz band channels can be summarized as follows: i) *Modeling the multi-ray propagation*: The multi-ray propagation is present in many common scenarios. A unified multi-ray model for the entire Terahertz spectrum needs to be developed, which incorporates the accurate characterization of the line-of-sight (LoS), reflected, scattered and diffracted paths. ii) *Analyzing the channel characteristics*: The channel parameters of the Terahertz spectrum such as the path gain, the wideband channel capacity, the rms delay spread and the temporal broadening effects need to be accurately investigated. These parameters are influenced by multiple factors including the operating frequency, communication distance and the material properties of the environment. These challenges need to be addressed to realize the design of efficient and reliable ultra-high-speed wireless communications in the THz band.

The first contribution of this thesis (Chapter 2) is the development of a unified multi-ray channel model in the THz band based on ray tracing techniques using a bottom-up approach. This multi-path channel incorporates the propagation models for the LoS, reflected, scattered and diffracted paths, is validated by the experimental measurements. Using the developed propagation models, we present an in-depth analysis on the channel characteristics in the THz band. Specifically, we analyze the distance-varying and frequency-selective nature of the Terahertz channel. Moreover, we study the coherence bandwidth, and point

out the significance of the delay spread. Furthermore, we characterize the wideband channel capacity using flat and water-filling power allocation strategies. Additionally, we analyze the temporal broadening effects of the Terahertz channel. Finally, we advocate for distance-adaptive and multi-carrier transmissions to best benefit from the unique relationship between distance and bandwidth.

1.3.2 Multi-Wideband Waveform Design

In the waveform design in the THz band, the channel uniqueness needs to be best-exploited, which includes the distance-varying spectral windows, the large coherence bandwidth due to the delay spread and the temporal broadening effects [28]. Hence, the waveform for transmission needs to be tailored for the channel. The additional challenges and requirements to be addressed for the THz band waveform design remain and can be summarized as follows [2]. First, the transmission distance for ultra-high-speed communication is very limited due to the very high path loss. Moreover, the spectral windows are highly distance-dependent. Hence, an adaptive modulation scheme needs to be adopted to improve the transmission range and support ultra-high-speed links. Second, the ultra-broad bandwidth of the individual spectral window at the order of tens of GHz, which motivates the multi-wideband transmission by dividing each spectral window into a set of sub-windows or sub-bands. However, the interference, including the inter-symbol and inter-band interferences of the multi-band systems, need to be investigated throughly and incorporated in the performance evaluation.

The second contribution of this thesis (Chapter 3) is that we propose a multi-wideband waveform design for the distance-adaptive THz band communication, which includes the features of the pseudo-random time-hopping sequence and the polarity randomization. To cope with the unique characteristics and improve the distance, the pulse waveform design in the distance-adaptive multi-wideband system for the THz band includes the development of the waveform model and the dynamical adaptation of the rate and the transmit power on each sub-window. Furthermore, we analyze the inter-symbol interference (ISI)

between the consecutive symbols and inter-band interference (IBI) among the neighboring frequency sub-bands associated with the developed multi-wideband system, which need to be considered for the distance improvement. We further provide the close-form expressions for the signal-to-interference-plus-noise-per-bit (SINR-per-bit) and the bit-error-rate (BER) to analyze the system performance. Moreover, we formulate an optimization framework to solve for the multi-wideband waveform design parameters of the transmit power and sub-window rate (i.e., the number of frames for each symbol), based on the system model and the waveform design. The aim is to maximize the communication distance while satisfying the rate and the transmit power constraints. To avoid solving the non-convex optimization problem with the prohibitive computational complexity, four sub-optimal solutions are proposed and compared for the optimization problem. An extensive numerical analysis is performed to evaluate the multi-wideband system performance.

1.3.3 Timing Acquisition

Synchronization provides accurate timing information of the received signal to accomplish demodulation at the receiver, and it becomes a challenging problem in ultra-high-speed wireless communication networks in the THz band. Timing errors as small as picoseconds can seriously degrade the system performance. As a result, timing acquisition, which is one part of the synchronization, constitutes an important but yet unexplored topic in the THz band system design to date. The unique challenges and requirements for the THz band synchronization are summarized as follows: i) THz band communication and propagation peculiarities. The THz band channel is highly frequency-selective, and is characterized by severe attenuation as well as distortion of the transmitted pulses [28]. Moreover, the severe frequency-selectivity causes temporal broadening effects of the transmitted signals [28] and hence, increases the difficulties for timing acquisition drastically. ii) Demand of ultra-high sampling rates. Given the very broad bandwidth of the THz band signaling (ranging from tens of GHz up to several THz), the digital synchronization, which has the advantages

of cost-efficiency, full integration, and robustness [29, 30], requires multi-hundreds-Giga-samples-per-second (Gs/s) and even Tera-samples-per-second (Ts/s) sampling rates, while the fastest sampling rate to date is not exceeding 100 Gs/s [31, 32].

The third contribution of this thesis (Chapter 4) is that we propose and analyze two timing acquisition algorithms for pulse-based THz band communications. First, we extend the theory of sampling signals with finite rate of innovation [33, 34, 35, 36] from compressive sampling in signal processing to the communication context, and propose a low-sampling-rate (LSR) algorithm for timing acquisition in the THz band. In this LSR algorithm, the features of annihilating filters [37, 38] are exploited in the framework of the THz pulse-based communication. We tailor the algorithm to the THz band synchronization to cope with the unique channel characteristics at the THz frequencies and the more challenging requirements for the reduction of the sampling rate. Furthermore, this LSR works well when the SNR is high, i.e., above 10 dB. Complementary to the LSR approach, a maximum likelihood (ML) approach for timing acquisition is proposed in the low SNR case for THz band communications. This algorithm adopts a two-step acquisition procedure to derive the timing acquisition solutions based on the ML criterion [39, 40, 41]. Furthermore, the resulting BER sensitivity to the timing errors in the two algorithms are both analytically and numerically studied.

1.3.4 Distance-aware Bandwidth-adaptive Resource Allocation

For the realization of ultra-high-speed wireless communication networks in the THz band, it is imperative to develop a novel communication scheme that can address the unique challenges and requirements, which are summarized as follows. First, the transmission distance for ultra-high-speed communication is very limited due to the very high path loss. An advanced communication scheme needs to be developed with the object to improve the transmission distance to support single or even multiple ultra-high-speed links simultaneously [1]. Second, the physical properties in the channel need to be taken into account. For example, the very strong relationship between the distance and the bandwidth in the THz

band requires adaption of the utilizing bandwidth as a function of the distance. Moreover, the delay spread and temporal broadening [28] affect the physical parameters design in the communication scheme. Third, the enormous usable bandwidth in the THz band needs to be fully and efficiently exploited in multi-user networks. In particular, a strategic spectrum utilization design is demanded to simultaneously support multiple ultra-high-speed links in the THz band.

The fourth contribution of this thesis (Chapter 5) is that we develop a distance-aware bandwidth-adaptive resource allocation scheme in THz band communication networks, with the objective to improve the communication distance. The proposed resource allocation scheme captures the unique channel peculiarities including the relationship between the distance and the bandwidth, and strategically utilizes the spectrum to enable multiple ultra-high-speed links in long-range networks. In particular, we develop a distance-aware bandwidth-adaptive resource allocation scheme in the THz band communication network, which captures the peculiarities of distance-varying spectral windows and efficiently exploits the Terahertz spectrum. The solutions to the bandwidth utilization, the spectrum allocation, the modulation techniques, and the transmit power are jointly derived. Moreover, we propose a strategic spectrum allocation principle for the multi-user network, to intelligently allocate the center spectrum of the spectral windows to the long-distance users first, and then the side spectrum to the short-distance users. Theoretical bounds on the network data rate are analyzed. This principle is evaluated to effectively improve the spectrum utilization and enables multiple ultra-high-speed links in the THz band networks.

1.3.5 Three-Dimensional End-to-End Modeling and Analysis

An accurate three-dimensional (3-D) channel model is demanded to accurately characterize the Terahertz spectrum peculiarities in both the elevation and azimuth planes. In realistic application scenarios, the multi-path rays arrive the receiver from both the azimuth and elevation planes, which is the result of the 3-D radiation diagram of the antennas and the 3-D propagation of the electromagnetic waves. These facts introduce an angular spread in

the elevation plane, and influence the channel physical peculiarities. Moreover, graphene-based antennas to operate in the THz band are suggested in [42, 43, 44, 45, 27], due to the fact that graphene supports the propagation of surface plasmon polariton (SPP) waves. The main merit of using graphene-based antennas is that the equivalent electrical size is much larger than its physical dimensions due to the much lower speed of SPP waves in a graphene-based antenna compared to that of free-space electromagnetic waves in a metallic antenna [27]. To overcome the very high path loss at THz frequencies, reflectarray antenna technologies [46] are very attractive among others, by taking advantages of parabolic reflectors and phased arrays. This approach is especially fruitful to provide high directivity gain with low losses at high frequencies such as the THz band. In the literature, reflectarray antennas have been studied in microwave and millimeter-wave bands [47], and more recently experimentally demonstrated [48] and theoretically analyzed at THz frequencies [49, 50], from the antenna design perspective. However, the integration of the graphene-based reflectarray antenna response into the THz band channel model, and the influences on the channel peculiarities have not been characterized from the communication perspective.

The fifth contribution of this thesis (Chapter 6) is that we develop an analytical 3-D end-to-end model in the THz band, which includes the responses of the graphene-based reflectarray antenna and the 3-D multi-path propagation channel. In particular, the architecture of a graphene-based reflectarray antenna is investigated and the 3-D radiation pattern is modeled. Moreover, a 3-D THz channel model is developed based on ray tracing techniques, as a superposition of the LoS, reflected and scattered paths. Using the developed model, we present an in-depth analysis on the 3-D channel characteristics and the influence of directivity from graphene-based reflectarray antennas in the THz band. In particular, we thoroughly characterize the antenna gain and the beamwidth, the delay spread and the coherence bandwidth, the 3-D angular spread, the wideband channel capacity, and the beam misalignment influence.

1.4 Organization of the Thesis

The rest of the thesis is organized as follows. A unified multi-path propagation channel is modeled and the wideband characterizations are analyzed, in Chapter 2. Then, a multi-wideband waveform design for the THz band is proposed to improve the distance and support ultra-high-speed transmission, in Chapter 3. Moreover, two algorithms for timing acquisition in the pulse-based wireless systems are proposed in Chapter 4. In addition, a distance-aware bandwidth resource allocation scheme for the single-user and multi-user THz band networks is developed in Chapter 5. As an extension of the multi-path model, a 3-D end-to-end model is analyzed in Chapter 6, which includes the graphene-based antenna response and the 3-D propagation phenomena. Finally, the research contributions are summarized in Chapter 7.

CHAPTER 2

MULTI-PATH CHANNEL MODELING AND WIDEBAND CHARACTERIZATION

For the realization of optimal wireless communication networks in the THz band, it is imperative to develop a unified channel model which accurately characterizes the Terahertz spectrum peculiarities. In this chapter, we develop a unified multi-ray channel model in the THz band (0.06 - 10 THz) based on ray tracing techniques using a bottom-up approach. The developed theoretical model is validated with the experimental measurements from the literature. Using the developed propagation models, we present an in-depth analysis on the channel characteristics in the THz band. Specifically, we analyze the distance-varying and frequency-selective nature of the Terahertz channel. Moreover, we study the coherence bandwidth, and point out the significance of the delay spread. Furthermore, we characterize the wideband channel capacity using flat and water-filling power allocation strategies. Additionally, we analyze the temporal broadening effects of the Terahertz channel. Finally, we advocate for distance-adaptive and multi-carrier transmissions to best benefit from the unique relationship between distance and bandwidth.

2.1 Motivation and Related Work

The existing channel models for the lower frequency bands such as 60 GHz [51] do not capture the behavior of the THz band, such as the very high molecular absorption loss or the very high reflection loss. The few channel models in the THz band to date [8, 52, 53, 54] are aimed at characterizing the multi-path channel at 0.3 THz, as the experimental measurements are readily available. These models capture the peculiarities of the EM wave transmission in the THz band, including the molecular absorption effect of direct ray propagation and the scattering loss of rough surfaces in indirect ray communication. However, they are mainly based on measurements, which are strictly subject to the specific

indoor environment settings. Moreover, a stochastically 0.3 THz indoor channel model is introduced in [55], which provides a scenario-specific parameter set for the considered environment. Nevertheless, the thorough analysis for the wideband channel characteristics is missing. Hence, there is a need for a unified multi-ray propagation model with thorough understanding and analysis of the entire Terahertz spectrum to lay out the foundation for reliable and efficient wireless communications in the THz band.

2.2 Electromagnetic Wave Propagation in the THz Band: A Multi-ray Model

We use the ray tracing techniques to develop the multi-ray channel model, by utilizing the principles of geometric optics to trace the propagation of LoS, reflected, diffusely scattered and diffracted EM waves. The very short wavelength in the THz band allows accurate modeling with this ray optical approach. In particular, ray tracing methods have been proved to enable very good prediction capabilities at 60 GHz as well as low Terahertz frequency at 0.3 THz [8].

Since the frequency dependency appears in the propagation channel and antennas in the THz band, we develop a multi-ray propagation model in the THz band as the combination of many individual sub-bands. Each sub-band is considered to be narrow enough to have flat frequency response. In the i^{th} frequency sub-band, the narrowband channel impulse response is expressed as a superposition of N_i rays, among which the n^{th} ray experiences frequency-dependent attenuation $\alpha_{i,n}$. For any fixed transmitter and receiver locations and stationary environment, by denoting τ as the propagation delay, the channel response of the multi-ray model is given by

$$h_i(\tau) = \sum_{n=1}^{N_i} \alpha_{i,n} \delta(\tau - \tau_n). \tag{1}$$

The multi-ray propagation consists of LoS, reflected, scattered, and diffracted paths, which are demonstrated in Fig. 4. If there are $N_{\text{Ref}}^{(i)}$ reflected rays, $N_{\text{Sca}}^{(i)}$ scattered rays, and $N_{\text{Dif}}^{(i)}$ diffracted rays in the i^{th} frequency sub-band, the multi-ray channel model can be

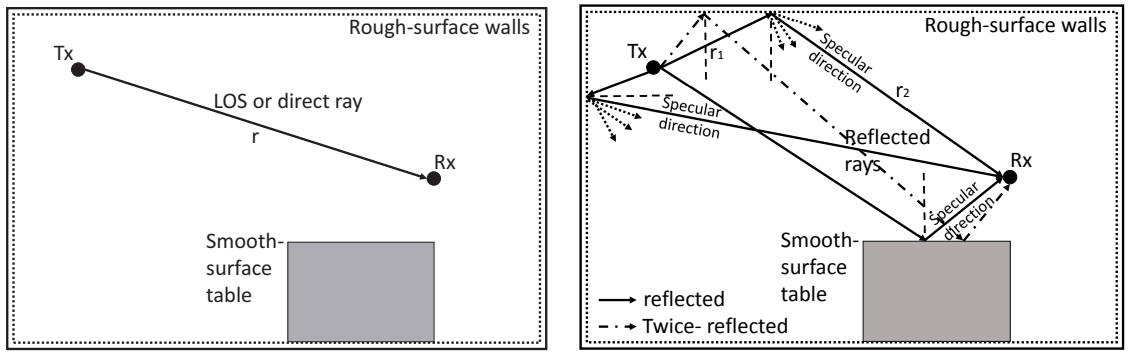

(a) Line-of-sight or direct ray propagation (b) Reflected ray propagation

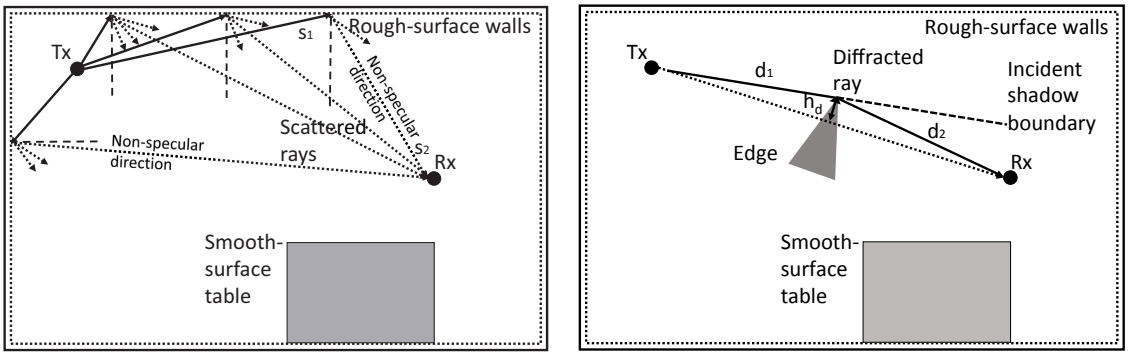

(c) Scattered ray propagation (d) Diffracted ray propagation

Figure 4. Propagation models between the transmitter (Tx) and the receiver (Rx).

described as

$$h_i(\tau) = \alpha_{\mathrm{LoS}}^{(i)}\delta(\tau - \tau_{\mathrm{LoS}})\mathbb{1}_{\mathrm{LoS}} + \sum_{p=1}^{N_{\mathrm{Ref}}^{(i)}} \alpha_{\mathrm{Ref}}^{(i,p)}\delta(\tau - \tau_{\mathrm{Ref}}^{(p)}) + \sum_{q=1}^{N_{\mathrm{Sca}}^{(i)}} \alpha_{\mathrm{Sca}}^{(i,q)}\delta(\tau - \tau_{\mathrm{Sca}}^{(q)}) + \sum_{u=1}^{N_{\mathrm{Dif}}^{(i)}} \alpha_{\mathrm{Dif}}^{(i,u)}\delta(\tau - \tau_{\mathrm{Dif}}^{(u)}), \tag{2}$$

where $\mathbb{1}_{\mathrm{LoS}}$ is the indicator function that is equal to 1 or 0 for the presence of LoS path or not. For the LoS path, $\alpha_{\mathrm{LoS}}^{(i)}$ refers to the attenuation, and τ_{LoS} stands for the delay. For the p^{th} reflected path, $\alpha_{\mathrm{Ref}}^{(i,p)}$ is the attenuation and $\tau_{\mathrm{Ref}}^{(p)}$ is the delay. Similarly for the q^{th} scattered path and u^{th} diffracted path, the attenuations are expressed as $\alpha_{\mathrm{Sca}}^{(i,q)}$ and $\alpha_{\mathrm{Dif}}^{(i,u)}$, while the delays are denoted by $\tau_{\mathrm{Sca}}^{(q)}$ and $\tau_{\mathrm{Dif}}^{(u)}$, respectively.

By invoking the Wiener-Khinchin theorem, the attenuations and delays in the i^{th} frequency sub-band can be written as

$$\left(\alpha_{\mathrm{LoS}}^{(i)}, \alpha_{\mathrm{Ref}}^{(i,p)}, \alpha_{\mathrm{Sca}}^{(i,q)}, \alpha_{\mathrm{Dif}}^{(i,u)}\right)^T = \left(\left|H_{\mathrm{LoS}}(f_i)\right|, \left|H_{\mathrm{Ref}}^{(p)}(f_i)\right|, \left|H_{\mathrm{Sca}}^{(q)}(f_i)\right|, \left|H_{\mathrm{Dif}}^{(u)}(f_i)\right|\right)^T, \tag{3}$$

where H_{LoS}, $H_{\text{Ref}}^{(p)}$, $H_{\text{Sca}}^{(q)}$ and $H_{\text{Dif}}^{(u)}$ are the transfer functions for the LoS, reflected, scattered and diffracted propagation paths, respectively.

2.3 Multi-path Propagation Effects

The transfer functions for the LOS (Fig. 4(a)), reflected (Fig. 4(b)), scattered (Fig. 4(c)) and diffracted (Fig. 4(d)) ray propagation are described here. A major challenge in non-line-of-sight propagation is the rough surface roughness. In the THz band, any surface with roughness comparable to the wavelength (i.e., millimeter or sub-millimeter) scatters the EM wave. As a result, surfaces that are considered smooth at lower-frequencies wireless communication become rough in the THz band.

LoS Propagation: The LoS channel transfer function, H_{LoS}, consists of the spreading loss function, H_{Spr}, and the molecular absorption loss function, H_{Abs}, as

$$H_{\text{LoS}}(f) = H_{\text{Spr}}(f)H_{\text{Abs}}(f)\mathrm{e}^{-j2\pi f\tau_{\text{LoS}}}. \tag{4}$$

The transfer function due to the spreading loss is given by

$$H_{\text{Spr}}(f) = \frac{c}{4\pi \cdot f \cdot r}. \tag{5}$$

The transfer function of the molecular absorption loss has the form

$$H_{\text{Abs}}(f) = \mathrm{e}^{-\frac{1}{2}k(f)r}, \tag{6}$$

where c denotes the speed of light, r stands for the distance between the transmitter and the receiver, and $\tau_{\text{LoS}} = r/c$ equals to the time-of-arrival of the LoS propagation. In particular, k is the frequency-dependent medium absorption coefficient, and depends on the composition of the transmission medium at a molecular level [56].

Reflected Ray Propagation: If we denote R as the the reflection coefficient, r_1 as the distance between the transmitter and the reflector, and r_2 as the distance between the reflector and the receiver, then the frequency-dependent transfer function of the reflected ray

propagation, H_{Ref}, is given by

$$H_{\text{Ref}}(f) = \left(\frac{c}{4\pi \cdot f \cdot (r_1 + r_2)}\right) \mathrm{e}^{-j2\pi f \tau_{\text{Ref}} - \frac{1}{2}k(f)(r_1+r_2)} \cdot R(f), \tag{7}$$

where $\tau_{\text{Ref}} = \tau_{\text{LoS}} + (r_1 + r_2 - r)/c$ is the time-of-arrival of the reflected ray. We use the Kirchhoff theory to capture the reflection loss, and the reflection coefficient for a rough surface can be obtained by multiplying the smooth surface reflection coefficient derived from the Fresnel equations, γ_{TE}, with the *Rayleigh roughness factor*, ρ, as

$$R\,(f) = \gamma_{\text{TE}}\,(f) \cdot \rho\,(f)\,. \tag{8}$$

The Fresnel reflection coefficient for TE polarized waves on a smooth surface is

$$\begin{aligned}
\gamma_{\text{TE}}\,(f) &= \frac{\cos(\theta_{\text{i}}) - n_t\sqrt{1 - \left(\frac{1}{n_t}\sin(\theta_{\text{i}})\right)^2}}{\cos(\theta_{\text{i}}) + n_t\sqrt{1 - \left(\frac{1}{n_t}\sin(\theta_{\text{i}})\right)^2}} \\
&\approx -\left(1 + \frac{-2\cos(\theta_{\text{i}})}{\sqrt{n_t^2 - 1}}\right) \\
&\approx -\exp\left(\frac{-2\cos(\theta_{\text{i}})}{\sqrt{n_t^2 - 1}}\right),
\end{aligned} \tag{9}$$

where θ_{i} is the angle of incident wave and can be computed using the law of cosine and to the locations of the transmitter, the receiver and the reflection point. Moreover, n_t refers to the refractive index, which varies with the frequencies and medium material [57]. The roughness effect is characterized by a Rayleigh factor [57], as

$$\rho(f) = \exp\left(-\frac{8\pi^2 \cdot f^2 \cdot \sigma^2 \cdot \cos^2(\theta_{\text{i}})}{c^2}\right), \tag{10}$$

where σ is the Gaussian-distributed rough surface height standard deviation.

Scattered Ray Propagation Model: In the THz band, the wavelength is at the order of millimeters or below, which results in diffuse scattering very critical in channel modeling. The impact of scattering increases with higher roughness level. Similarly in the specular reflected model, we consider the scattering on a surface with a Gaussian-like height distribution, where sharp irregularities are not present if the correlation length of the rough

surface, L, is larger than the wavelength. We denote S as the the scattering coefficient for a rough surface, s_1 as the distance between the transmitter and the scattering point, and s_2 as the distance between the scattering point and the receiver. Then the transfer function of the scattered ray propagation, H_{Sca}, is given by

$$H_{\text{Sca}}(f) = \left(\frac{c}{4\pi \cdot f \cdot (s_1 + s_2)}\right) \mathrm{e}^{-j2\pi f \tau_{\text{Sca}} - \frac{1}{2}k(f)(s_1+s_2)} \cdot S(f), \tag{11}$$

where $\tau_{\text{Sca}} = \tau_{\text{LoS}} + (s_1 + s_2 - r)/c$ is the time-of-arrival of the scattered ray. The scattering geometry is considered on the tangent plane (the incident azimuth angle ϕ_1 is π), and θ_1 stands for the zenith angle of the incident wave. In addition, θ_2 and ϕ_2 denote the zenith and azimuth angle of the scattered wave, respectively. The scattering coefficient of rough surfaces according to the modified Beckmann-Kirchhoff theory [58] and Taylor's approximation is given by

$$S(f) \approx -\exp\left(\frac{-2\cos(\theta_1)}{\sqrt{n_t^2 - 1}}\right) \cdot \sqrt{\frac{1}{1 + g + \frac{g^2}{2} + \frac{g^3}{6}}} \cdot \sqrt{\rho_0^2 + \frac{\pi\cos(\theta_1)}{100}\left(g\mathrm{e}^{-v_s} + \frac{g^2}{4}\mathrm{e}^{-v_s/2}\right)} \tag{12}$$

Detailed computations for the parameters including $g, \rho_0, l_x, l_y, v_x, v_y, v_s$ can be found in [58].

Diffracted Ray Propagation Model: We use the Fresnel Knife Edge Diffraction (KED) theory to provide approximated characterization for diffraction. By incorporating the diffraction loss, $L(f)$, the diffraction channel transfer function, H_{Dif}, is given by

$$H_{\text{Dif}}(f) = \left(\frac{c}{4\pi \cdot f \cdot (d_1 + d_2)}\right) \mathrm{e}^{-j2\pi f \tau_{\text{dif}} - \frac{1}{2}k(f)(d_1+d_2)} \cdot L(f), \tag{13}$$

where d_1 as the distance between the transmitter and the diffracting point, d_2 as the distance between the diffracting point and the receiver, and $\tau_{\text{Dif}} = \tau_{\text{LoS}} + \triangle d/c$ is the time-of-arrival of the diffracted ray. In a common diffraction geometry where h_{d} (see Fig. 4(d)) is small relative to d_1 and d_2, the diffracted signal travels an additional distance relative to the LoS path approximately as $\triangle d = \frac{h_{\text{d}}^2(d_1+d_2)}{2d_1d_2}$. If we define $\nu(f) = \sqrt{\frac{2f\triangle d}{c}}$, the diffraction coefficient

can be obtained by an approximation to the Fresnel integral, as

$$L(f) = \begin{cases} \mu_1(f) \cdot \left(0.5\mathrm{e}^{-0.95\nu(f)}\right) & 0 < \nu \leq 1, \\ \mu_2(f) \cdot \left(0.4 - \sqrt{0.12 - (0.38 - 0.1\nu(f))^2}\right) & 1 < \nu \leq 2.4, \\ \mu_3(f) \cdot (0.225/\nu(f)) & \nu > 2.4, \end{cases} \tag{14}$$

where the frequency-dependent parameters μ_1, μ_2, μ_3 are chosen to best fit the empirical data in [59].

2.4 Overall Multi-ray Model for THz Band Wireless Communication

By combining the aforementioned models in (4), (7), (11) and (13), the multi-ray model in the i^{th} frequency sub-band in (2) can be rearranged in (15).

$$\begin{aligned} h_i(\tau) = & \left| \frac{c}{4\pi \cdot f_i \cdot r} \mathrm{e}^{-\frac{1}{2}k(f_i)r} \right| \cdot \delta(\tau - \tau_{\text{LoS}}) \mathbb{1}_{\text{LoS}} \\ & + \sum_{p=1}^{N_{\text{Ref}}^{(i)}} \left| \left(\frac{c}{4\pi \cdot f_i \cdot (r_1 + r_2)} \right) \mathrm{e}^{-\frac{1}{2}k(f_i)(r_1+r_2)} \cdot \left(-\mathrm{e}^{\frac{-2\cos(\theta_1)}{\sqrt{n_t^2-1}}} \right) \mathrm{e}^{-\frac{8\pi^2 \cdot f^2 \cdot \sigma^2 \cdot \cos^2(\theta_1)}{c^2}} \right|_p \cdot \delta(\tau - \tau_{\text{Ref}}^{(p)}) \\ & + \sum_{q=1}^{N_{\text{Sca}}^{(i)}} \left| \left(\frac{c}{4\pi \cdot f_i \cdot (s_1 + s_2)} \right) \mathrm{e}^{-\frac{1}{2}k(f_i)(s_1+s_2)} \cdot \left(-\mathrm{e}^{\frac{-2\cos(\theta_1)}{\sqrt{n_t^2-1}}} \right) \cdot \sqrt{\frac{1}{1 + g + \frac{g^2}{2} + \frac{g^3}{6}}} \right|_q \\ & \qquad \cdot \left| \sqrt{\rho_0^2 + \frac{\pi \cos(\theta_1)}{100} \left(g\mathrm{e}^{-\nu_s} + \frac{g^2}{4} \mathrm{e}^{-\nu_s/2} \right)} \right|_q \cdot \delta(\tau - \tau_{\text{Sca}}^{(q)}) \\ & + \sum_{u=1}^{N_{\text{Dif}}^{(i)}} \left| \left(\frac{c}{4\pi \cdot f_i \cdot (d_1 + d_2)} \right) \mathrm{e}^{-\frac{1}{2}k(f_i)(d_1+d_2)} \cdot L(f_i) \right|_u \cdot \delta(\tau - \tau_{\text{Dif}}^{(u)}). \end{aligned} \tag{15}$$

2.5 Validation of Multi-Ray Model with Experimental Measurements

In this section, we validate the developed multipath channel model with the existed experimental measurements, at 60 GHz [51], and 0.3 THz [57, 60, 59]. The developed multi-ray channel model is unified in the THz Band (0.1- 10 THz), although the validation and evaluation are up to 1 THz limited by the available parameter measurements.

The received signal in a multi-ray channel is contributed by not only the LoS path, but also non-line-of-sight (NLoS), which includes the reflected, scattered and diffracted rays.

As a result, the coefficients for reflection, scattering and diffraction from our derivations, are validated with the measured data first. Ultimately, the sub-band multi-ray model is validated.

2.5.1 Reflection Coefficient

The reflection coefficients for the plaster are characterized, as a function of the incident angle and the frequency, respectively, in Fig. 5(a) and 5(b). In particular, more energy is lost as the incident wave approaches the perpendicular to the surface, i.e., incident angle approaches zero. Moreover, the reflection loss is more severe for larger frequencies, because the level of roughness rises as the wavelength drops. In these figures, the theoretical model in (8), the approximation using (133), and the measured data from [57] are plotted for comparison. Furthermore, the mean square error (MSE) between the theoretical model and its approximation is computed to quantitatively evaluate the approximation. These results show very good accuracy of modeling and approximation have been obtained, particularly for large incident angles.

2.5.2 Scattering Coefficient

The theoretical models and the approximation for scattering coefficients are verified. By fixing the frequency at 0.3 THz, incident zenith angle at $\theta_1 = 30^\circ$ and the scattered azimuth angle at $\phi_2 = 0^\circ$, the scattering coefficient for the plaster is shown as a function of the scattered zenith angle θ_2, in Figure 5(c). The parameter values used in (12) include: the refractive index $n_t = 2.24 - j0.025$, the rough surface height standard deviation $\sigma = 0.088$ mm, and the correlation length $L = 0.18$ mm [60]. The approximation shows a reasonable agreement with the theoretical model and the measurements. Next, by fixing the scattered zenith angle, the scattering loss rises with the frequency non-monotonically up to 0.7 THz, as shown in Fig. 5(d). The scattering angles are selected as $\theta_1 = 30^\circ, \theta_2 = 45^\circ$, and $\phi_2 = 0^\circ$. The approximation in (12) has very small MSE of 0.2 dB over the frequency range up to 0.7 THz, compared to the theoretical model by modified Beckmann-Kirchhoff theory.

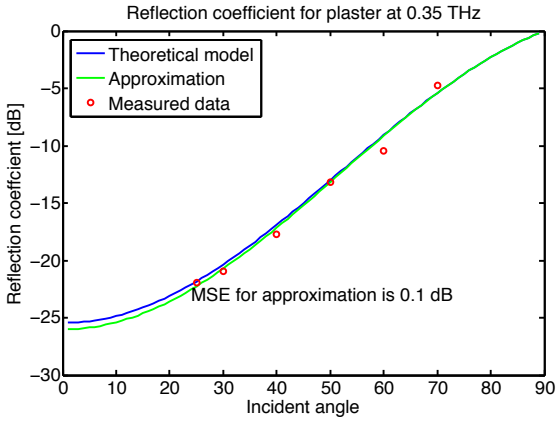

(a) Reflection coefficient vs. incident angle. Measured data is from [57].

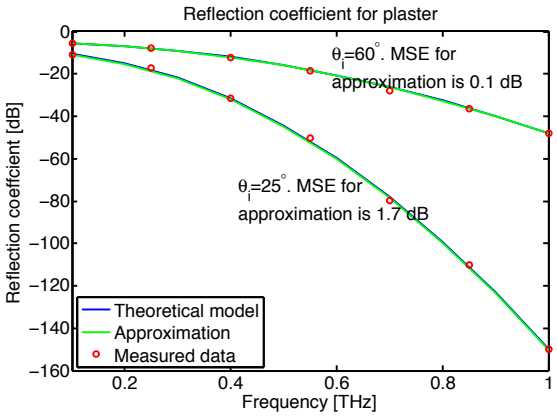

(b) Reflection coefficient vs. frequency. Measured data is from [57].

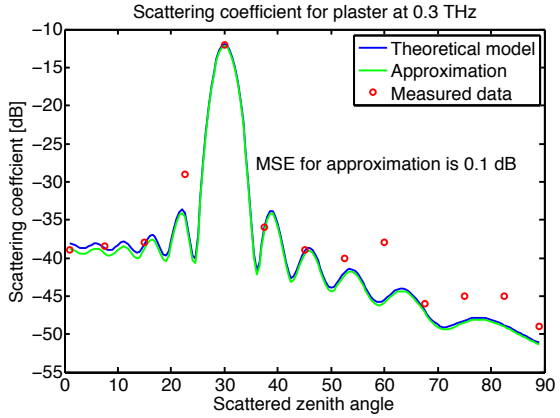

(c) Scattering coefficient vs. scattered zenith angle. Measured data is from [60].

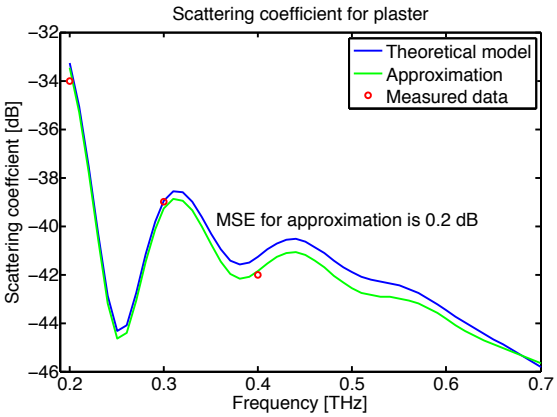

(d) Scattering coefficient vs. frequency. Measured data is from [60].

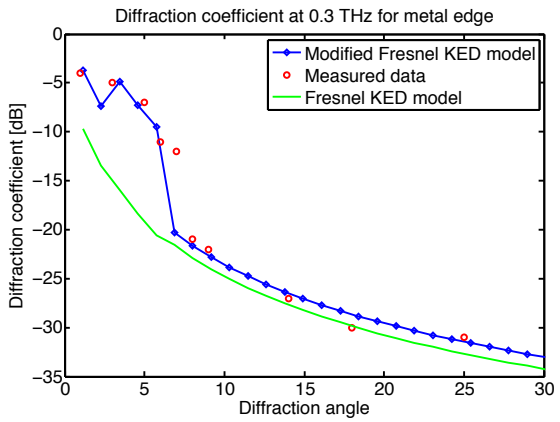

(e) Diffraction coefficient for metal edge. Measured data is from [59].

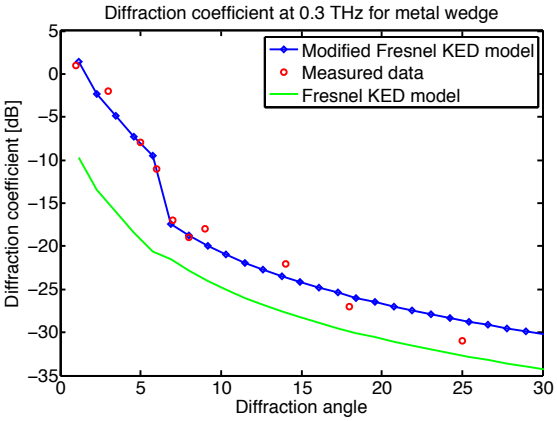

(f) Diffraction coefficient for metal wedge. Measured data is from [59].

Figure 5. Validation for reflection, scattering and diffraction coefficients.

2.5.3 Diffraction Coefficient

The diffraction coefficients are evaluated using the modified KED model in (14), the measured data [59] and the KED model. In Fig. 5(e) and 5(f), the diffraction coefficients for the metal edge and the metal wedge are plotted individually. Because of the lacking for consideration of material properties, the KED model is not as accurate as the modified KED model in (14). In particular, we compute the parameters $[\mu_1, \mu_2, \mu_3]$ as $[2, 3.6, 1.15]$ for the metal edge, and $[3.6, 3.6, 1.6]$ for the metal wedge, which are obtained based on the empirical experiments. The increasing of diffraction loss for larger diffraction angle α_{d} is well captured by the modified KED model.

2.5.4 Multi-ray Model

Ultimately, we validate our multi-ray propagation model in (15) with the experimental measurements conducted in a room of dimensions 5m×2.75m×2.5m, in which there are two tables separated by a screen [60]. The transmitter Tx is placed under the ceiling to obtain a large coverage of the room, located at (0.25m,2.5m,2.3m), while the two receivers are placed on the two tables separately.

In Case 1, the receiver Rx_1 has LoS path available and is placed at (1.375m, 0.625m, 0.75m). By contrast, in Case 2, the receiver Rx_2 has no LoS, and is placed at (3.625m, 0.625m, 0.75m). The walls and the ceiling are covered by plaster, where its refractive index up to 1 THz can be found in [57]. The simulation results are summarized in Table 1, which include the type of arrival path, the path gain and the delay. These results are validated with the measured at 0.3 THz in [60, 59]. The observations are summarized as follows.

- *Case 1: LoS is present*. The distance between Tx and Rx_1 is 3m. When $f_i = 0.3$ THz, the LoS ray arrives at 8.94ns with the power -90.6 dB. The total gain reaches -86.5 dB, which suggests a 4.1 dB improvement to have multi-path propagation. In this simulation, the LoS, the once-reflected, the twice-reflected and the scattered rays are included.

Table 1. The significant arrival rays at 0.3 THz.

	Case 1, when LoS is present		Case 2, when LoS is absent	
Arrival path	**Path Gain [dB]**	**Delay [ns]**	**Path Gain [dB]**	**Delay [ns]**
LoS	-90.6	8.94	—	—
Reflected ray 1	-102.1	9.14	-102.2	14.01
Reflected ray 2	-103.4	9.77	-101.8	14.43
Reflected ray 3	-116.7	10.01	-111.3	14.58
Scattered ray 1	-125.8	9.80	-134.7	14.45
Scattered ray 2	-144.2	10.27	-134.8	14.61
Scattered ray 3	-141.7	11.08	152.5	15.66
Scattered ray 4	-134.1	12.74	-143.5	22.48
Dffracted ray 1	—	—	-125.9	14.03

- *Case 2: LoS is absent.* The distance between Tx and Rx_2 is 4m. The once-reflected, the twice-reflected, the relevant scattered and the diffracted rays are included in this simulation. The strongest reflected ray travels through the ceiling, arriving at 14.43ns with the path gain -101.8 dB. The total gain by including multi-path propagation is -94.2 dB, which is 7.6 dB improvement compared to the single NLoS transmission. Moreover, the diffracted path is included in our simulation, having a delay of 14.03ns and a path gain of -125.9 dB.

2.5.5 Discussion

The developed narrowband channel model considers that the system bandwidth is narrow enough so that the frequency response can be treated as a complex valued scalar over the whole bandwidth, the so-called frequency-flat channel. Then, we develop a multi-ray propagation model in the THz band as a combination of these individual sub-bands. In each sub-band, the multi-ray model is a superposition of the LoS, reflected, scattered and diffracted paths.

The principles to develop efficient multi-ray model are summarized here. When LoS is available, the direct ray dominates the received signal energy, while the reflected rays play a dominant role when LoS is absent. As the operating frequency increases, the surface is seen to be rougher and hence, more power is scattered out of the specular direction. Hence,

scattered rays are very important and have to be included in the ray tracing model for both LoS and NLoS conditions. Furthermore, the diffraction path can be ignored in general, only except when the receiver is in the very closed region near the incident shadow boundary.

In our analysis of the two study cases, the number of specular reflected rays is up to 6, which may include: one from the table, one from the ceiling, and four from the four walls. Moreover, the number of dominant scattered rays is 60. For each dominant reflected ray, i.e., on the table, ceiling and four walls, we consider 10 scattered rays surrounding the each reflection point. Lastly, when LoS is not available, and there is a screen or a wedge between the transmitter and the receiver, the number of diffracted ray is 1. Otherwise, the diffracted rays are negligible.

2.6 Wideband Characterization

Using the developed propagation models, a detailed analysis on the wideband channel characteristics in the THz band is presented here. Specifically, we thoroughly characterize the distance-varying spectral windows, the wideband channel capacity, the rms delay spread and the coherence bandwidth, and the temporal broadening effects in this section.

2.6.1 Distance-varying Spectral Windows

Due to the molecular absorption effect, path loss peaks are created, and the spectral windows between these peaks are investigated, as shown in Fig. 6. In particular, three spectral windows between 0.06 THz and 1 THz can be recognized, which are 0.06 - 0.54 THz, 0.57 - 0.74 THz and 0.76 - 0.97 THz, respectively. As the material properties of reflection, the scattering and the diffraction properties being measured at higher Terahertz frequencies (e.g., 1 - 10 THz), more spectral windows can be identified in the future.

The path gain and the width of the spectral windows vary with the center frequency and the distance. First, as the center frequency increases, the channel path gain values drop, and the width of the spectral windows dwindles. The path gain separation among different distances increase for larger center frequencies. Second, the relationship between

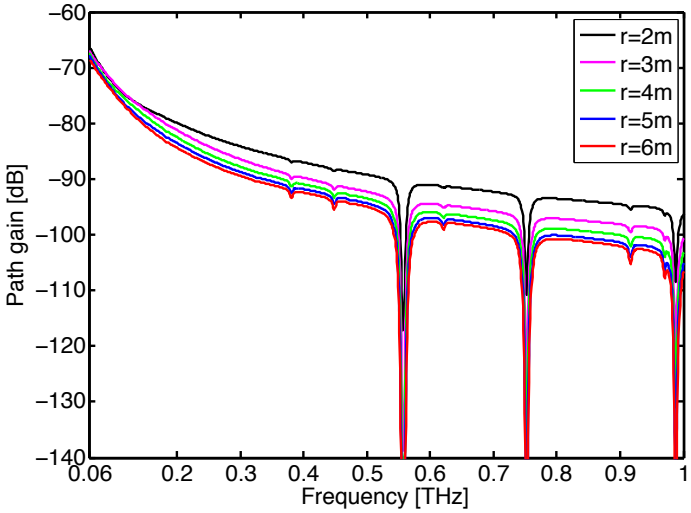

Figure 6. Path gain as a function of frequency.

the distance and the path gain is very close, particularly for short distances. For example, when distance changes from 2m to 3m, the average path gain decreases from -88.3 dB to -91.4 dB. On the contrary, by increasing the distance from 5m to 6m, the path gain difference is only 1 dB, from -94.6 to -95.6 dB. Third, the available spectrum for communication reduces rapidly as the distance increases. For example, when the distance is 6m, only the frequency bands (0.06 - 0.54 THz) and (0.58 - 0.73 THz) have path loss values below 100 dB. This close relationship between the distance and the spectral windows motivates the design of distance-aware communication schemes [61].

2.6.2 Wideband Channel Capacity

To evaluate the wideband channel capacity in the THz band, we can decompose the received signal as a sum of the sub-bands, where each sub-band channel is narrow and has a flat-band response. In particular, the i^{th} sub-band is defined as $\Delta f_i = f_{i+1} - f_i$ with power P_i under the constraint $\sum_{i=1}^{N_B} P_i \leq P$, where N_B refers to the total number of sub-bands, and P stands for the total transmit power. In the i^{th} narrowband, the sub-band capacity, C_i, is expressed as

$$C_i = \Delta f_i \log\left(1 + \frac{|h_i|^2 P_i}{\Delta f_i S_N(f_i)}\right) \tag{16}$$

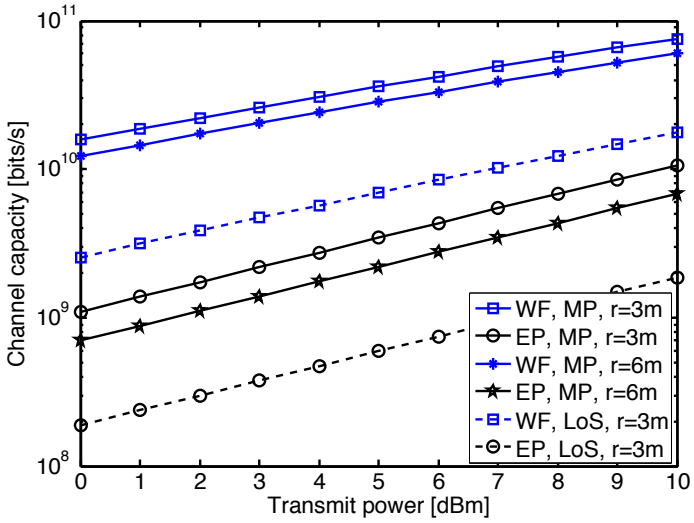

Figure 7. Wideband channel capacity for different propagation channels and distances.

where S_N is the power spectral density of the additive white Gaussian noise. h_i is given in (15). Then, the wideband channel capacity in the THz band can be found as the sum of the capacities of each sub-band [56], as

$$C = \sum_{i=1}^{N_B} \Delta f_i \log\left(1 + \frac{|h_i|^2 P_i}{\Delta f_i S_N(f_i)}\right). \tag{17}$$

By varying the total transmit power from 0 to 10 dBm, the channel capacity is numerically computed and shown in Fig. 7, for different transmission distances, different power allocation strategies and different propagation. We assume the utilized frequency band is from 0.06 THz to 1 THz, and the distance between the transmitter and the receiver is 3m and 6m. Using the water-filling (WF) power allocation strategy, the multi-path (MP) capacity increases with the transmit power and reaches 75 Gbps at $P = 10$ dBm and $r = 3$m. The mean capacity under these conditions is 39.9 Gbps. On the contrary, the mean capacity reduces by 89% and becomes 4.4 Gbps if the equal power (EP) allocation scheme is adopted. This suggests an importance of the intelligent resource allocation in exploiting the Terahertz spectrum due to the very high frequency-selectivity. On the other hand, the capacity decreases as the distance increases. In particular, at $r = 6$m, the average MP capacity based on WF strategy equals to 31.4 Gbps. Furthermore, as the multi-path propagation has over 4 dB gain over the LoS, the mean capacity of the multi-ray channel is 4.8 times that

of the LoS path solely. However, this improvement of total path gain and capacity of the multi-path propagation are at the costs of the increased delay spread and consequently, the restricted coherence bandwidth to avoid ISI in practice.

2.6.3 RMS Delay Spread and Coherence Bandwidth

We provide an analytical expression to compute the rms delay spread, which is a measure of how dispersive the channel is. This temporal parameter relates to the performance degradation caused by ISI and useful for the physical system design. The rms delay spread is computed as [62]

$$\sigma_i = \sqrt{\overline{\tau_i^2} - (\overline{\tau_i})^2}, \tag{18}$$

where

$$\overline{\tau_i} = \frac{\sum_{n=1}^{N} |\alpha_{i,n}|^2 \tau_n}{\sum_{n=1}^{N} |\alpha_{i,n}|^2}, \tag{19}$$

and

$$\overline{\tau_i^2} = \frac{\sum_{n=1}^{N} |\alpha_{i,n}|^2 \tau_n^2}{\sum_{n=1}^{N} |\alpha_{i,n}|^2}, \tag{20}$$

are the first moment (or called the mean excess delay) and second moments of the instantaneous power-delay profile, respectively. $\alpha_{i,n}$ is the amplitude of the n^{th} path in the i^{th} sub-band, as given in (1).

Regarding the power delay profile of Case 1 in Table 1, the rms delay spread is calculated as 0.19ns for $r = 3$m. This value suggests that the symbol rate is limited to $0.1/\sigma_i = 0.53$ Gbit/s to avoid ISI for linearly-modulated signals. Moreover, the coherence bandwidth, that is defined as the range of frequencies over which channel correlation exceeds 50%, is given by $0.2/\sigma_i = 1.06$ GHz. The increasing frequency would lead to multi-path effect dwindling, due to the very high loss for the NLoS paths. This results in a smaller rms delay spread and hence, larger coherence bandwidth, as shown in Fig. 8. In particular, when the distance is 3m and the center frequency is 0.7 THz, the rms delay spread drops to 51.7ps, and the coherence bandwidth grows to 3.87 GHz.

As the simulation dimensions and the distance between the transmitter and the receiver

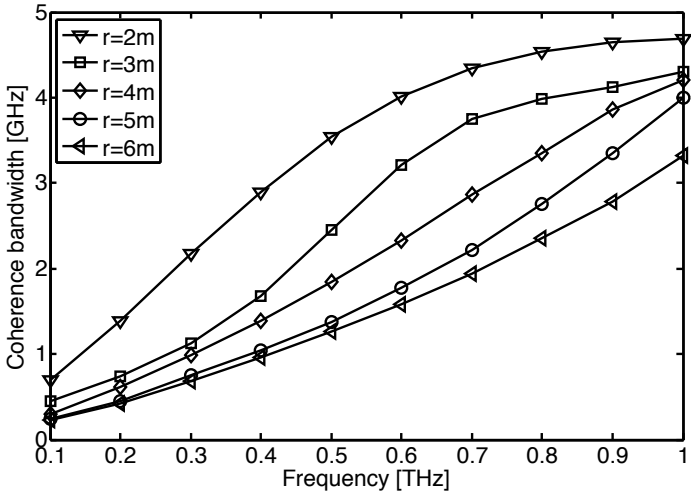

Figure 8. Coherence bandwidth at different center frequencies.

increase, the ray inter-arrival times are extended. This leads to the larger rms delay spread in the multi-ray channel and therefore, the smaller coherence bandwidth in the THz band. The average of the coherence bandwidth drops from 3.42 GHz, to 2.56 GHz, 2.17 GHz, 1.75 GHz and 1.47 GHz, as the distance varies from 2m, to 3m, 4m, 5m, and 6m, respectively. Moreover, as the distance increases, the convergence of the coherence bandwidth at each center frequency can be observed.

2.6.4 Temporal Broadening

The transmitted signal experiences the frequency-selectivity in the THz wideband channel, as shown in (15) and Fig. 6. This frequency-selective attenuation causes broadening effects on the transmitted signals, which restricts the minimum spacing between consecutive pulses and hence the data rates. Therefore, in this section, we present an extensive investigation of the temporal broadening effects in the THz band. Similar broadening effects have been observed in ultra-wideband (UWB) systems [63, 64]. However, in the THz band, the broadening effects are much stronger due to the much higher level of frequency selectivity.

An illustration of this broadening effect is shown in Fig. 9 and explained as follows. In order to occupy the Terahertz spectrum, a very short pulse or for simplicity, a Dirac

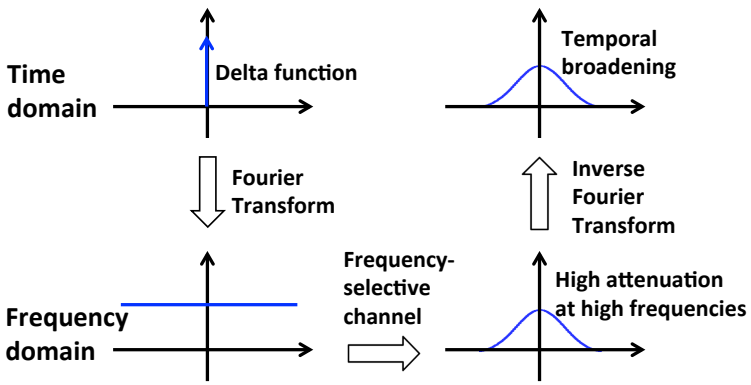

Figure 9. An illustration for the temporal broadening effects.

delta function in the time domain is transmitted through the frequency-selective Terahertz channel. The Fourier transform of the dirac delta function is flat in the frequency domain. Then, by passing through channel, the transmitted signal experiences increasing path loss at higher frequencies. As the received signal is transformed back to the time domain using inverse Fourier transform, the broadening effect appears clearly, in contrast to the originally transmitted delta function.

In order to quantitatively characterize the broadening effects in the THz band, the auto-correlation of signals is needed. We define the *pulse duration*, t_d, as the time after which the auto-correlation stays below 0.1% of its maximum, which is equivalent to -30 dB interference to neighboring signals. This pulse duration suggests the minimum separation between consecutive pulses of transmission, in order to avoid ISI. Furthermore, we define the *broadening factor*, η, as the ratio between the pulse duration of the received pulse and that of the transmitted pulse. We analyze the broadening effects for both LoS and NLoS propagation, by transmitting raised-cosine pulses. This investigation is particularly useful when high-directivity antennas are being deployed and LoS path or directed NLoS is guaranteed. In general, the broadening factor increases for higher center frequency, wider pulse bandwidth and longer communication distance. Under these conditions, the level of frequency-selectivity in the channel increases. The quantitative observations are discussed as follows.

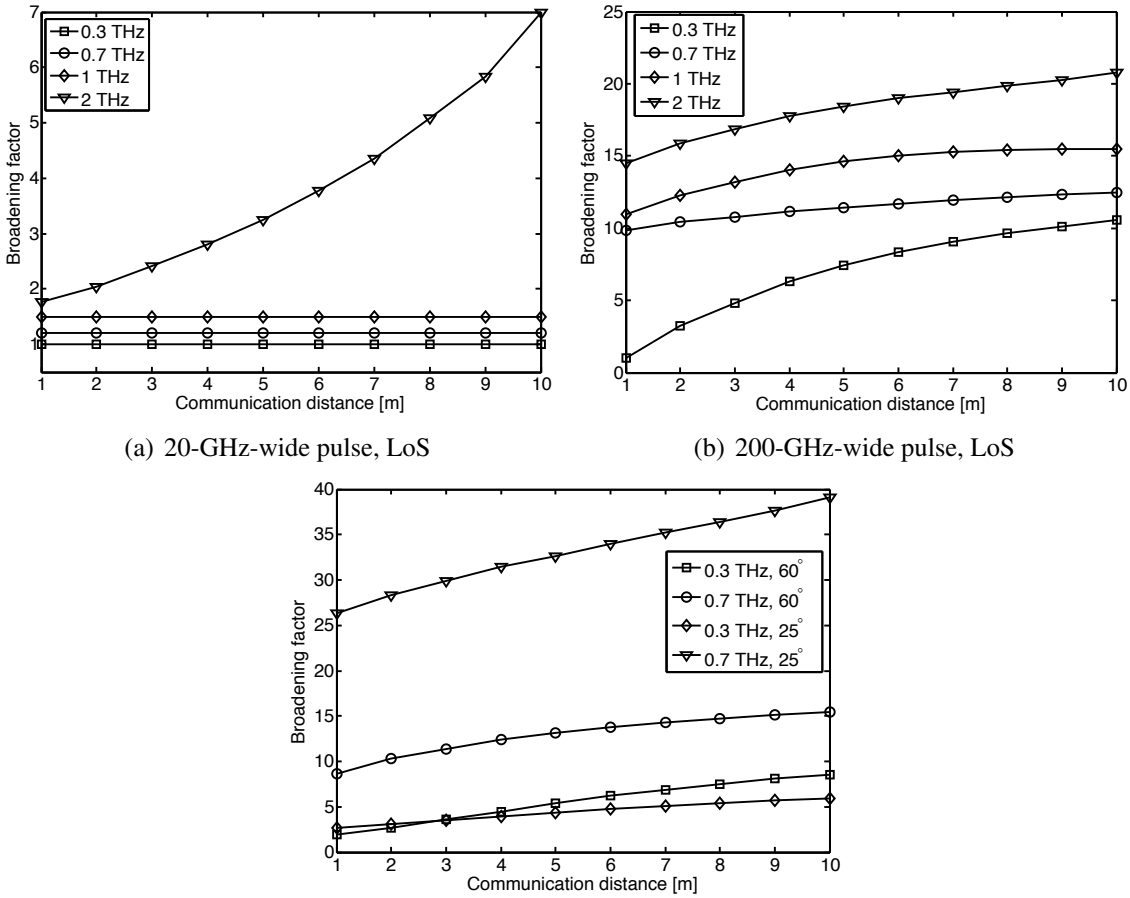

(a) 20-GHz-wide pulse, LoS

(b) 200-GHz-wide pulse, LoS

(c) 200-GHz-wide pulse, reflected NLoS

Figure 10. Broadening factor analysis.

- The broadening factor is closely related to the transmitted signal. In Fig. 10(a), the transmitted pulse occupies a bandwidth of 20 GHz and the pulse duration is $t_d = 120.4$ps. The frequency-selective attenuation has broadening effects, and the broadening factor is smaller than 10. In Fig. 10(b), the 200-GHz-wide raised-cosine pulse with the duration $t_d = 10.6$ps is transmitted. This wide pulse experiences a more severe frequency-selectivity and the resulting η exceeds 10 easily.

- The broadening factor depends on the center frequency. As the carrier frequencies increases from 0.3 THz to 0.7 THz, 1 THz and 2 THz, the broadening factors increase, because of more severe frequency-selectivity at higher frequencies in the THz band. For example in Fig. 10(a), the average η is below 2 for $f_i = 0.3, 0.7$ and 1 THz. On the contrary, the average broadening factor is 3.75 when $f_i = 2$ THz. This suggests that to avoid ISI, a minimal 0.45ns separation is required for the transmission of 20 GHz-wide pulses centered at 2 THz.

- As the communication distance increases, the frequency-selectivity in the THz band becomes stronger and hence, more severe distortion arises on the received signals, as shown in Fig. 10(b). At $f_i = 0.3$ THz and 1m, the broadening factor increases from 1.04 to 10.57, when the distance varies from 1m to 10m. Consequently, to avoid ISI, at least 0.11ns spacing is needed between consecutive transmission, when the distance is 10m, the center frequency is 0.3 THz and the transmitted raised-cosine pulse has a width of 200 GHz.

- The NLoS propagation affects the temporal broadening, as shown in Fig. 10(c). Without loss of generality, the reflected NLoS transmission is considered. For the same traveling distances and transmitted pulses, the reflection introduces additional loss as well as distortion on transmitted signals, particularly at higher frequencies. At 0.7 THz and $\theta_{\mathrm{i}} = 25^{\circ}$, the reflection loss is -80 dB and the average broadening factor almost triples, increasing from 11.5 (see Fig. 10(b)) to 33.1.

2.6.5 Impact on Communication Techniques in the THz Band

These wideband channel characteristics coupled with the technology limitations, strongly affect the transmission techniques in the THz band. The classical modulation schemes can be used for THz band communication, but they will not be able to fully benefit the THz band channel properties, such as the strong relationship between the distance and the bandwidth. In particular, three communication schemes are covered here, namely *impulse radio*, *distance-adaptive modulation*, and *multi-carrier transmission*.

First, the impulse radio techniques are developed for THz band nano-networks [65], for its ultra-low complexity design. However, they are impractical for macro-scale applications, for the following reasons. By occupying the frequency spectrum up to several THz, this baseband scheme would interfere with the existing cellular networks operating in dedicated bands. Moreover, the occupation of the THz-wide bandwidth causes severe wideband broadening effects (as discussed in Sec. 2.6.4), which strictly restrict the pulse rates. In particular, by occupying the entire THz band, this impulse radio scheme experiences extreme frequency-selectivity. Although the pulse duration is 0.15ps, the average broadening factor is 1319, which indicates a minimum separation of 0.19ns between the neighboring pulses. This would result in the maximal pulse rate of 5.05×10^9 pulses-per-second to avoid ISI. Additionally, the synchronization for the extreme short pulses operating in the THz band is extremely challenging, since it may require very high sampling rates (e.g., over multi-giga- or tera-samples per second).

Second, for distances longer than 1m, the molecular absorption defines multiple transmission windows, in which each window has a strongly distance-dependent bandwidth (as discussed in Sec. 2.6.1). In order to utilize the advantages of the strong relationship between the bandwidth and the distance, a new distance-aware adaptive modulation solution appears as an interesting path to explore. In this context, we developed a new modulation solution that allows the nodes to intelligently share the channel by adapting the modulation scheme dependent on the transmission distance [61]. In particular, a node can adaptively

choose modulations based on the transmission distance in order to occupy either (i) the entire transmission bandwidth, (ii) the central part of the transmission window (this information reaches both close and far nodes), or (iii) the sides of the transmission window (the information only reaches nearby devices).

Third, the multi-carrier modulation permits adaptive transmissions of different symbols on non-overlapping sub-bands in parallel. As a result, each carrier occupies a smaller bandwidth (for example, 5 GHz as suggested in Sec. 2.6.3) and supports lower data rates. This effectively relaxes the design requirements of individual carriers, and is helpful for THz band communication to overcome ISI and can reach very high data rates. As compensation, many parallel modulators for different carriers and very fast signal generator to switch between carriers, are required to support multi-carrier modulation. Hence, the optimal sub-band width needs to be determined. However, the orthogonal frequency division multiplexing (OFDM) is not suitable for THz band communication currently, although it is suggested for 60 GHz systems to enhance the spectral efficiency [66]. The bandwidth is not scarce in the THz band. Furthermore, the very complex transceivers, high peak-to-average power ratio (PAPR), and strict requirements for frequency synchronization make the OFDM challenging and impractical in the THz band for the current technologies, where digital processors which can handle such high data rates are still not existing. Consequently, based on the channel characteristics in the THz band, distance-adaptive and multi-carrier transmissions are suggested to best benefit from the unique relationship between distance and bandwidth.

2.7 Conclusions

In this chapter, we developed a unified multi-ray channel model in the THz band by using ray tracing techniques. This multi-ray channel incorporates the propagation models for the LoS, reflected, scattered and diffracted paths, is validated by the experimental measurements (0.06 - 1 THz). Based on the developed propagation model, we presented a

thorough analysis on the channel characteristics in the THz band. Specifically, first, the spectral windows defined by the molecular absorption loss are distance-varying, and the width of these windows reduces as the distance increases. Second, the multi-path wide-band channel capacity can exceed 75 Gb/s with the use of 10 dBm transmit power and a water-filling power allocation strategy over 0.06 - 1 THz. This improvement of total path gain and capacity of the multi-path propagation over LoS are at the cost of the increased delay spread and consequently, the restricted coherence bandwidth to avoid ISI. Third, the rms delay spread is dependent on the distances and carrier frequencies. The resulting co-herence bandwidth is below 5 GHz, which decreases for longer distances and lower carrier frequencies. Fourth, the temporal broadening effects limit the minimum spacing between consecutive transmission and hence the data rate. The defined broadening factor increases for higher center frequency, wider pulse bandwidth, longer distance, and is affected by the propagation path. Fifth, in terms of communication techniques, distance-adaptive and multi-carrier transmissions are suggested to best benefit from the unique relationship be-tween distance and bandwidth. This work that addresses the unified multi-ray channel modeling and in-depth characteristic analysis lays out the foundation to design reliable and efficient communication systems in the THz band.

CHAPTER 3

MULTI-WIDEBAND WAVEFORM DESIGN FOR DISTANCE-ADAPTIVE WIRELESS SYSTEMS

In this chapter, a multi-wideband waveform design for the THz band is proposed, by exploiting the channel peculiarities including the distance-varying spectral windows, the delay spread and the temporal broadening effects. This scheme allows the dynamical variation of the rate and the transmit power on each sub-window and improves the distance. Moreover, the closed-form expressions of the SINR and BER for the multi-wideband waveform are derived, by considering the inter-symbol and inter-band interferences. Then, an optimization framework is formulated to solve for the multi-wideband waveform design parameters of the transmit power and the number of frames, with the aim to maximize the communication distance while satisfying the rate and the transmit power constraints. Four sub-optimal solutions are proposed and compared.

3.1 Motivation and Related Work

There are only few solutions which proposed on the way to design the THz signal waveform. In [65], a single-band pulse-based scheme is proposed at the THz frequencies. However, this modulation is mainly valid for very short transmission distances, e.g. nanonetworks, in which the distance-varying spectral windows do not appear. In our preliminary study, a multi-narrowband system is developed. However, the resulting number of subbands is quite large and the MQAM is complicated. Moreover, the interference in the multi-narrowband system is neglected [61]. Hence, there is a need for a multi-wideband waveform design to improve the distance and support ultra-high-speed transmission.

The design guidelines based on the channel characteristics according to Chapter 2 are highlighted as follows. The very strong relationship between the distance and the spectral windows at THz frequencies motivates the design to be distance-adaptive and in the

form of multi-wideband. Moreover, the utilization of the sub-bands needs to be intelligently selected to avoid spectrum with the path loss peaks. Specifically, in the multi-path propagation with d = 5m, the spectrum above 0.1 THz has significantly large path loss and cannot be used. In the directional propagation, the communication around 0.56 THz, 0.75 THz, and 0.98 THz needs to be prevented. In terms of the transmission over each sub-band, wideband pulses can be used, for the features of ultra-low power, compact-size and ultra-low complexity design. These pulses were firstly proposed for ultra-wideband communication [67] and then was tailored for THz band communication [65]. By occupying the bandwidth B_g, each sub-window experiences frequency-selective fading for multi-path propagation, while undergoes flat-fading for directional transmission with a much larger coherence bandwidth. Furthermore, in accordance with the temporal broadening, the minimum separation between the consecutive pulses to avoid the pulse overlapping is $5T_p$, where T_p denotes the pulse waveform duration.

3.2 Multi-Wideband Communications in the Terahertz Band

In this section, we first propose a multi-wideband waveform model for the distance-adaptive THz band communication by exploiting the channel peculiarities. Furthermore, we analyze the ISI between the consecutive symbols and IBI among the neighboring frequency sub-bands associated with the developed multi-wideband system. We further provide the close-form expressions for the SINR-per-bit and the BER to analyze the system performance.

3.2.1 Pulse Waveform Model

In the multi-wideband communication, each sub-window experiences frequency-selective fading, since the width of the sub-window is greater than the coherence bandwidth, as studied in Fig. 6. To increase the received SINR-per-bit, each information symbol on the sub-window is represented by a sequence of very short pulses, which provides the pulse combing gain. Within one sequence, the positions of the pulses are determined by a pseudo-random time-hopping sequence that is specific to each sub-window. Furthermore,

pulse-based polarity randomization is utilized to provide further robustness against the interference and help optimize the spectral shape [67, 68]. We tailor this pulse waveform to the THz band to cope with the unique characteristics at the THz frequencies and improve the SINR or equivalently, the distance.

For the transmission on the u^{th} sub-window, the baseband signal consists of different symbols. For the i^{th} information symbol, N_f^u frames are used to describe this symbol with one pulse in one frame. This is represented as

$$x_u(t) = \sqrt{P_u} \sum_i a_u^{(i)} \sum_{m=0}^{N_f^u-1} p_u^{(i,m)} \cdot g(t - iN_f^u T_f - mT_f - c_u^{(i,m)} T_p), \tag{21}$$

where T_f and T_p denote the time duration for one frame and one pulse, with their ratio defining the number of pulse positions in a frame, i.e., $N_p = T_f/T_p$. Additionally, P_u stands for the allocated power in the u^{th} sub-window, N_f^u is the number of frames to represent one information symbol. In the signal model with polarity randomization and time hopping [67], $a_u^{(i)} \in \{+1, -1\}$ is the i^{th} binary information symbol, $p_u^{(i,m)}$ denotes the random polarity code that takes ± 1 with equal probability, and $c_u^{(i,m)}$ refers to the time hopping code where $c_u^{(i,m)} \in \{0, 1, \cdots, N_p - 1\}$ with equal probability of the m^{th} frame. $g(t)$ is the transmitted wideband pulse with the duration T_p and unit energy.

By combining the signal model in (21) and the THz band channel model in (2), the received signal is described as

$$\begin{aligned}
y_u(t, d) &= x_u(t) * h_u(t, d) + w(t) \\
&= \alpha_{\text{LoS}}^{(u)}(d) \sqrt{P_u} \sum_i a_u^{(i)} \sum_{m=0}^{N_f^u-1} p_u^{(i,m)} \cdot g_r(t - iN_f^u T_f - mT_f - c_u^{(i,m)} T_p - t_{\text{LoS}}) \mathbb{1}_{\text{LoS}} \\
&+ \sqrt{P_u} \sum_{q=1}^{N_{\text{Ref}}^{(u)}} \alpha_{\text{Ref}}^{(u,q)}(d) \sum_i a_u^{(i)} \sum_{m=0}^{N_f^u-1} p_u^{(i,j)} \cdot g_r(t - iN_f^u T_f - mT_f - c_u^{(i,m)} T_p - t_{\text{Ref}}^{(q)}) + w(t) \\
&= \sqrt{P_u} \sum_i a_u^{(i)} \sum_{m=0}^{N_f^u-1} p_u^{(i,m)} \cdot \psi_u(t - iN_f^u T_f - mT_f - c_u^{(i,m)} T_p) + w(t),
\end{aligned} \tag{22}$$

where $w(t)$ is the Gaussian noise with the power spectral density S_w, and we define

$$\psi_u(t) = \alpha_{\text{LoS}}^{(u)}(d) g_r(t - t_{\text{LoS}}) \mathbb{1}_{\text{LoS}} + \sum_{q=1}^{N_{\text{Ref}}^{(u)}} \alpha_{\text{Ref}}^{(u,q)}(d) g_r(t - t_{\text{Ref}}^{(q)}), \tag{23}$$

with $\boldsymbol{\alpha}^{(u)} = [\alpha_{\text{LoS}}^{(u)}, \alpha_{\text{Ref}}^{(u,1)}, \ldots, \alpha_{\text{Ref}}^{(u,N_{\text{Ref}}^{(u)})}]$, and g_r is the received pulse with the unit energy, which includes the THz band channel effects on g, as defined in (21).

To combine the multi-path signals for the u^{th} sub-window, a Rake receiver is used with $\boldsymbol{\beta}^{(u)} = [\beta_{\text{LoS}}^{(u)}, \beta_1^{(u)}, \ldots, \beta_{N_{\text{Ref}}}^{(u)}]$ being the Rake combing weights. The output of the Rake receiver for the i^{th} binary information symbol can be obtained in the form of

$$r_u^{(i)}(d) = a_u^{(i)} \sqrt{P_u} N_f^u \alpha_{\text{LoS}}^{(u)}(d) \beta_{\text{LoS}}^{(u)} \mathbb{1}_{\text{LoS}} + a_u^{(i)} \sqrt{P_u} N_f^u \sum_{q=1}^{N_{\text{Ref}}^{(u)}} \alpha_{\text{Ref}}^{(u,q)}(d) \beta_q^{(u)} + ISI_u + IBI_u + w_u, \tag{24}$$

where the first term is due to the desired signal propagating through the LoS path, the second term is from the desired signals through the reflected paths, the third term is the ISI from the pulses in the adjacent frames due to the multi-path and temporal broadening effects, the fourth term describes the IBI from the surrounding sub-windows, and the last term refers to the output noise.

3.2.2 Interference

We analyze the two types of interference associated with the multi-wideband transmission as described in the previous section, namely, ISI and IBI, which account for the interference effects among different symbols and different sub-windows.

Inter-Symbol Interference (ISI): The interference for the i^{th} information symbol can be obtained as a sum of the interference effects on the individual pulses that consist of this symbol

$$ISI_u = \sqrt{P_u} \sum_{m=iN_f^u}^{(i+1)N_f^u - 1} I_u^{(i,m)}, \tag{25}$$

where the interference on the m^{th} pulse, $I_u^{(i,m)}$, is

$$I_u^{(i,m)} = p_u^{(i,m)} \sum_{n_1} \sum_{n_2=0}^{N_f^u - 1} p_u^{(n_1,n_2)} a_u^{(n_1)} \Psi_u[(n_1 - i)N_f^u T_f + (n_2 - m)T_f + (c_u^{(n_1,n_2)} - c_u^{(i,m)})T_p]. \tag{26}$$

Note that when $n_1 = i, n_2 = m$, $\Psi_u(0) = 0$. In the above equation, Ψ_u represents the cross-correlation between ψ_u and ψ'_u, as

$$\Psi_u(\tau) = \int_{-\infty}^{+\infty} \psi_u(t-\tau)\psi'_u(t)dt, \tag{27}$$

where ψ_u is given in (23), ψ'_u represents the weighted sum of the delayed version of the received pulse, in the form of

$$\psi'_u(t) = \beta^{(u)}_{\text{LoS}}(d)g_r(t - t_{\text{LoS}})\mathbb{1}_{\text{LoS}} + \sum_{q=1}^{N^{(u)}_{\text{Ref}}} \beta^{(u)}_q(d)g_r(t - t^{(q)}_{\text{Ref}}). \tag{28}$$

where the weights are the Rake receiver coefficients. The expected value of the interference is equal to zero due to the random polarity code that takes ± 1 with equal probability. The variance can be calculated from (26) and (27), as

$$E\left[I^{(i,m)^2}_u\right] = \frac{1}{N_p^2}\sum_{m=1}^{N_u-1} m\Bigg[\sum_{l=1}^{N_u-m} R_{g_r}(mT_p)\left(\boldsymbol{\beta}^{(u)}(l)\boldsymbol{\alpha}^{(u)}(l+m) + \boldsymbol{\alpha}^{(u)}(l)\boldsymbol{\beta}^{(u)}(l+m)\right)\Bigg]^2 \tag{29}$$

where $\boldsymbol{\alpha}^{(u)}$ is the vector of the channel attenuations and $\boldsymbol{\beta}^{(u)}$ is the vector of the Rake receiver weights. R_{g_r} denotes the auto-correlation function of g_r in (22).

In light of the results in (25) and (29), ISI_u for the multi-path propagation is approximately distributed as

$$ISI_u \sim \mathcal{N}\Bigg(0, \frac{P_u}{N_p^2}\sum_{m=1}^{N_u-1} m\Bigg[\sum_{l=1}^{N_u-m} R_{g_r}(mT_p)\left(\boldsymbol{\beta}^{(u)}(l)\boldsymbol{\alpha}^{(u)}(l+m) + \boldsymbol{\alpha}^{(u)}(l)\boldsymbol{\beta}^{(u)}(l+m)\right)\Bigg]^2\Bigg). \tag{30}$$

In (26), $p^{(i,m)}_u$ denotes the random polarity code and $a^{(i)}_u$ is the i^{th} binary information symbol, which both take ± 1 with equal probability. Moreover, the channel response in the u^{th} sub-window in (2) as a function of the distance, the Rake receiver coefficients and the number of frames are included in this expression.

As the distance increases, the delay spread and the temporal broadening effects increase. However, the increase of the distance reduces the path gains, particularly of the reflected paths since they travel through additional distances and suffer from the reflection loss. Hence, the resulting ISI becomes weaker. The above analysis for the ISI is for the

multi-path propagation. With the use of high-gain antennas, the beamwidth of the transmission is small and the number of the multi-path components reduces drastically. The delay spread with the 20-dB-gain antennas is negligible with $N_u = 1$. Furthermore, the temporal broadening effects are reduced thanks to the smaller path loss and frequency selectivity in the channel. Hence, the ISI effects can be neglected in the directional transmission.

Inter-Band Interference (IBI): The inter-band interference occurs in the multi-wideband systems which causes from the power leakage from the neighboring sub-windows. In the THz band, the number of sub-windows is at the order of multiple-tens. To model this interference, we invoke the central limit theorem to approximate the IBI with a Gaussian process. The IBI accounts for the power leakage from the surrounding sub-windows. It is shown in [69, 70, 71] that the interference from the adjacent frequency bands can be approximated as Gaussian distributed random variable. Hence, the distribution of the interference power on the u^{th} sub-window that superimposes from the other sub-windows has the expression

$$\begin{aligned} IBI_u &\sim \mathcal{N}\left(0, \int_{f_u} \sum_{v,v\neq u}^{U(d)} P_v |G_r^v(f_u) \sum_{m=1}^{N_u} \boldsymbol{\alpha}^{(v)}(m)\boldsymbol{\beta}^{(v)}(m)|^2 df_u\right), \\ &\approx \mathcal{N}\left(0, P_u \int_{f_u} \sum_{v,v\neq u}^{U(d)} |G_r^v(f_u) \sum_{m=1}^{N_u} \boldsymbol{\alpha}^{(v)}(m)\boldsymbol{\beta}^{(v)}(m)|^2 df_u\right), \end{aligned} \tag{31}$$

where $G_r^v(f_u)$ describes the interference on the u^{th} sub-window that is contributed from the v^{th} sub-window, with $v \neq u$.

The IBI mainly contributes from the neighboring sub-windows, i.e., $(u+1)^{\text{th}}$ and $(u-1)^{\text{th}}$ in this case. Hence, we rearrange the IBI_u by using P_u in the above approximation, by considering the channel quality and the resulting transmit power for the neighboring sub-windows are similar. This approximation is useful to obtain P_u in (37). Moreover, G_r^v is the frequency response from the v^{th} sub-window, based on the received pulse g_r in (22). The interaction with the THz band channel and the receiver coefficients are also captured in the above expression, which influences the IBI.

The IBI captures the power leakage from the surrounding sub-windows, and increases

if the separation between the consecutive sub-windows (i.e., the bandwidth of the sub-window that is denoted by B_g) decreases. As the distance increases, the frequency selectivity becomes more severe. Consequently, the temporal broadening makes the transmitted pulse in the time domain wider, which thereby leads to a reduction of the IBI in the frequency domain. With the use of high-gain antennas, the delay spread reduces significantly and the channel frequency response varies less frequency-selective. However, the path loss of the channel is reduced and hence, the IBI becomes more significant in this case. These effects are captured in (86).

3.2.3 Signal-to-Interference-plus-Noise-Ratio-per-Bit (SINR-per-bit)

The noise based on the Rake receiver in (24) is the weighted sum of the Gaussian noise from the different paths. The power power spectral density of the noise is distributed as

$$w_u \sim \mathcal{N}\left(0, N_f^u S_w \sum_{l=1}^{N_u} \left[\boldsymbol{\beta}^{(u)}(l)\right]^2\right). \tag{32}$$

Hence, by combining (24), (30), (86) and (32), the SINR-per-bit in the u^{th} sub-window at the receiver is calculated as

$$\gamma_u^{\text{mp}}(d) = \frac{P_u\left[N_f^u\left(\alpha_{\text{LoS}}^{(u)}(d)\beta_{\text{LoS}}^{(u)}\right) + N_f^u \sum_{q=1}^{N_{\text{Ref}}^{(u)}}\left(\alpha_{\text{Ref}}^{(u,q)}(d)\beta_q^{(u)}\right)\right]^2}{\frac{P_u}{N_p^2}\sigma_{\text{ISI}}^2 + P_u\sigma_{\text{IBI}}^2 + B_g N_f^u S_w \sigma_{\text{noise}}^2}, \tag{33}$$

where the interference and noise terms in the above equation are stemmed from (30), (86), and (32), respectively

$$\sigma_{\text{ISI}}^2 = \sum_{m=1}^{N_u-1} m[R_{g_r}(mT_p) \sum_{l=1}^{N_u-m}(\boldsymbol{\beta}^{(u)}(l)\boldsymbol{\alpha}^{(u)}(l+m) + \boldsymbol{\alpha}^{(u)}(l)\boldsymbol{\beta}^{(u)}(l+m))]^2, \tag{34}$$

$$\sigma_{\text{IBI}}^2 = \int_{f_u} \sum_{v,v\neq u}^{U(d)} |G_r^v(f_u) \sum_{m=1}^{N_u} \boldsymbol{\alpha}^{(u)}(m)\boldsymbol{\beta}^{(u)}(m)|^2 df_u, \tag{35}$$

$$\sigma_{\text{noise}}^2 = \sum_{l=1}^{N_u}\left[\boldsymbol{\beta}^{(u)}(l)\right]^2. \tag{36}$$

Correspondingly, for a given SINR-per-bit and the number of frame, the required transmit power on the sub-window is given by

$$P_u = \frac{\gamma_u^{\text{mp}}(d) B_g N_f^u S_w \sigma^2_{\text{noise}}}{\left[N_f^u \left(\alpha^{(u)}_{\text{LoS}}(d) \beta^{(u)}_{\text{LoS}} \right) \mathbb{1} + N_f^u \sum_{q=1}^{N^{(u)}_{\text{Ref}}} \left(\alpha^{(u,q)}_{\text{Ref}}(d) \beta^{(u)}_{q} \right) \right]^2 - A_1} \tag{37}$$

where $A_1 = \gamma_u^{\text{mp}}(d) \left[\frac{\sigma^2_{\text{ISI}}}{N_p^2} + \sigma^2_{\text{IBI}} \right]$.

The above analysis for the ISI is for the multi-path propagation with $G_t = G_r = 0$ dB. With the use of high-gain antennas, the transmission becomes directional and consequently, $N_u = 1$ and $\alpha^{(u)}_{\text{LoS}} \neq 0$. Moreover, the ISI term becomes negligible while the IBI term becomes more important. The SINR-per-bit for the directional transmission, γ_u^{di}, is given by

$$\gamma_u^{\text{di}}(d) = \frac{\left(N_f^u \alpha^{(u)}_{\text{LoS}}(d) \beta^{(u)}_{\text{LoS}} \right)^2}{\int_{f_u} \sum_{v, v \neq u}^{U(d)} |G_r^v(f_u) \alpha^{(u)}_{\text{LoS}}(d) \beta^{(u)}_{\text{LoS}}|^2 df_u + \frac{B_g N_f^u S_w}{G_t G_r P_u} \left[\beta^{(u)}_{\text{LoS}} \right]^2} \tag{38}$$

As a function of the desired SINR, the required transmit power on the sub-window for the directional transmission is

$$P_u^{\text{di}} = \frac{\gamma_u^{\text{di}}(d) B_g N_f^u S_w \left[\beta^{(u)}_{\text{LoS}} \right]^2}{G_t G_r \left(N_f^u \alpha^{(u)}_{\text{LoS}}(d) \beta^{(u)}_{\text{LoS}} \right)^2 - A_2} \tag{39}$$

where $A_2 = \gamma_u^{\text{di}}(d) \int_{f_u} G_t G_r \sum_{v, v \neq u}^{U(d)} |G_r^v(f_u) \alpha^{(u)}_{\text{LoS}}(d) \beta^{(u)}_{\text{LoS}}|^2 df_u$.

3.2.4 Bit-error-rate (BER)

In light of the SINR for the designed multi-wideband waveform, the error performance of the system can be computed. Particularly for the pulse-based systems by incorporating the interference and the noise effects jointly, the Q-function of the SINR was shown to capture the error behavior [67]. Hence, starting with the SINR expression in (33), the BER over the u^{th} sub-window for the multi-path propagation can be approximated as

$$\begin{aligned} \epsilon_u^{\text{mp}} &\approx Q\left(\sqrt{\gamma_u^{\text{mp}}} \right) \\ &\approx Q\left(\frac{N_f^u \alpha^{(u)}_{\text{LoS}}(d) \beta^{(u)}_{\text{LoS}} + N_f^u \sum_{q=1}^{N^{(u)}_{\text{Ref}}} \alpha^{(u,q)}_{\text{Ref}}(d) \beta^{(u)}_{q}}{\sqrt{\frac{A_1}{\gamma_u^{\text{mp}}(d)} + B_g N_f^u S_w \sigma^2_{\text{noise}} / P_u}} \right), \end{aligned} \tag{40}$$

where $Q(\cdot)$ denotes the Q-function.

For the directional transmission, the ISI can be omitted while the IBI increases with the use of high-gain antennas. According to the SINR expression in (38), the BER over one sub-window is given in the similar fashion, as

$$\epsilon_u^{\mathrm{di}} \approx Q\left(\frac{\sqrt{G_t G_r P_u} N_f^u \alpha_{\mathrm{LoS}}^{(u)}(d) \beta_{\mathrm{LoS}}^{(u)}}{\sqrt{\frac{A_2 P_u}{\gamma_u^{\mathrm{di}}(d)} + B_g N_f^u S_w \left[\beta_{\mathrm{LoS}}^{(u)}\right]^2}}\right). \tag{41}$$

From the above equations, the BER decreases with the increase of the SINR. Consequently, the BER decreases with the increase of the transmit power and the number of frames. Moreover, the BER in the directional transmission is greatly reduced thanks to the additional antenna gains as well as the elimination of the ISI.

3.3 Multi-Wideband Waveform Design

To cope with the unique characteristics and improve the distance, we dynamically adapt the rate (i.e., the number of frames) and the transmit power on each sub-window in the pulse waveform model of the distance-adaptive multi-wideband system in (21). To solve for these parameters, we formulate and solve the optimization framework with the aim to maximize the distance while satisfying the rate and transmit power constraints. Noticeably, this problem can be solved by solving the rate maximization problem for a given distance iteratively, by which the maximum distance is obtained when the maximum rate in the first problem reaches the threshold, R_{th}. In this section, we present the problem formulation and the solution to these two problems.

3.3.1 Rate Maximization for the Fixed Distance

For a distance d, we consider the total number of sub-windows is $U(d)$, which is the ratio between the total usable bandwidth and the sub-window bandwidth, B_g. The total rate is

equal to the sum of the rate over each sub-window, as

$$R_{\text{tot}} = \sum_{u=1}^{U(d)} k_u, \tag{42}$$

where by using the wideband signal model in (21), the rate over the u^{th} sub-window is equal to the inverse of the number of the symbols in one second, which is given by

$$\begin{aligned} k_u &= \frac{1}{N_f^u N_p T_p} \\ &= \frac{1}{N_f^u T_f}. \end{aligned} \tag{43}$$

The computation of k_u is a function of the number of frames. The number of frames is included in the SINR-per-bit in (33) and (38), for the multi-path and directional propagations, respectively. Moreover, the BER, in (40) and (41), are functions of the SINR-per-bit and the computed k_u. Therefore, k_u takes the SINR-per-bit as well as the BER into account implicitly. In fact, a tradeoff as an outcome of the waveform design is that the increase of the number of frames leads the decrease of the rate, the increase of the SINR-per-bit, and the decrease of the BER.

According to the waveform design in Sec. 3.2.1, when $N_f^u = 1, \forall u = 1, \ldots, U(d)$ is the theoretical upper bound to the data rate. However, this solution is infeasible due to the constraints on the transmit power and the SINR. To maximize the rate, the transmit power, P_u, and the number of frames, N_f^u, need to be determined over each sub-window. As the power needed to achieve a certain rate on one sub-window is independent of the rates on other sub-windows, we decouple the allocation of the transmit power with the distribution of the number of frames to obtain a sub-optimal solution. Furthermore, the spectral windows that are used for transmission are distance-adaptive and in particular, the sub-windows whose path loss exceeds the path loss threshold are not used. After the transmit power allocation is accomplished, the number of frames on each sub-window , N_f^u, can be determined as the smallest number that fulfills the SINR requirement. In particular, four power allocation schemes are considered in our analysis, as follows.

1. *Min power/bit*: The first scheme allocates the transmit power by minimizing the power-per-bit, which is also suggested in [72]. Relating to our waveform design, this scheme targets to minimize power/bit for each sub-window, i.e., minimize $P_u \cdot N_f^u$ as the rate is inversely proportional to N_f^u. This scheme allows an effective and fair utilization of the transmit power. The resulting power allocation increases steadily as the frequency increases and the SINR decreases. The resulting allocation is equivalent to the power inversion scheme, where more power is allocated to the higher frequency bands.

2. *Min N_f^u*: The second scheme allocates the power starting from the lower frequencies, i.e., $f_1 = 0.06$ THz to $f_U = 1$ THz, due to the monotonic increase of the path loss values. At each sub-window, the transmit power satisfies the SINR requirement with the lowest possible N_f^u, i.e., $N_f^u \geq 1$. This allocation continues until the transmit power requirement in (47) is satisfied. This may result in an unfair utilization of the transmit power by allocating no power to the high THz frequencies. This scheme is equivalent to the truncated power inversion scheme in [73].

3. *Water-filling*: The third scheme follows the water-filling principle [73], which results in the fact that the sub-windows with better quality are distributed with more power. To implement the water-filling allocation scheme, the SINR on each sub-window in (33) is computed by assuming the same number of frames, for example, $N_f^u = 1$. After the power distribution is determined, the smallest N_f^u is computed for each sub-window to achieve the possible largest rate.

4. *Equal-power*: The fourth scheme follows the equal-power principle [73], by letting $P_u = P_{\text{Tx}}$. Then, the smallest N_f^u is computed for each sub-window. This scheme allows the transmit power and the number of frames to be obtained offline and greatly reduces the computational complexity.

The complexities of sub-optimal algorithms are significantly reduced since the allocation of the transmit power is decoupled with the distribution of the number of frames, i.e., the rates over each sub-window. The four schemes yield different system performance as well as the computational complexity. The rate performance and the operation regions of the four schemes are investigated in the numerical section in Sec. 3.4, for both the multi-path propagation and the directional transmission.

3.3.2 Distance Maximization

In the previous section, the maximal rate is obtained for a given distance and the constraints on the transmit power and the SINR-per-bit. In light of these results, we formulate an optimization to find the largest distance by solving the previous problem iteratively, by which the maximum distance is obtained when the maximum rate in the first problem reaches the threshold, R_{th}.

3.3.2.1 Optimization Framework Formulation

For the multi-wideband system in the THz band, we formulate an optimization problem to maximize the communication distance, d, as follows:

$$\begin{aligned}
&\textit{Given:} && P_{\text{Tx}}, \gamma_{\text{th}}, R_{\text{th}}, S_w \\
&\textit{Find offline:} && T_f, T_p, N_p, B_g, \boldsymbol{\beta}^u \geq 0 && (44)\\
&\textit{Find:} && N_f^u, P_u \geq 0, && (45)\\
&\textit{Maximize:} && d && (46)\\
&\textit{Subject to:} && \\
&\text{Transmit power:} && E\left[P_u\right] \leq P_{\text{Tx}} && (47)\\
&\text{SINR-per-bit:} && \gamma_u^{\text{mp}}(d) \geq \gamma_{\text{th}}, \forall u = 1, \ldots, U(d) && (48)\\
&\text{Data rate:} && \sum_{u=1}^{U(d)} \frac{1}{N_f^u N_p T_p} \geq R_{\text{th}} && (49)
\end{aligned}$$

In the above framework, $E[\cdot]$ stands for the expectation operator. Moreover, U denotes the total number of sub-windows at the distance d with the sub-window bandwidth B_g, which

is at the order of 10^2. In (48), γ_u^{mp} is given in (33). In (49), the data rate is obtained from (43).

3.3.2.2 Solution to the Optimization Problem

This optimization requires prohibitive computational complexity for an optimal solution, for the following reasons. First, this is a non-convex optimization problem with a non-convex constraint (49), since the Hessian of this constraint is not positive semi-definite.

Furthermore, the complexity grows exponentially with the number of constraints and variables. There are $U + 2$ constraints and the number of variables is $2U$, where U is at the order of 10^2. Instead of searching for an optimal solution, we use algorithms developed in Sec. 3.3.1 to obtain the sub-optimal solutions for the design parameters. Initially, we select the Rake receiver coefficients by pursuing the maximum ratio combining principle. The amplitude and the phase satisfy [74]

$$\beta_l^{(u)} = |\alpha_l| \mathrm{e}^{j2\pi f_u t_l}, \text{ for } l = 1, \ldots, N_u. \tag{50}$$

Moreover, we compute the pulse width, $T_p = 0.5$ns, the number of pulse positions in one frame, $N_p = 5$, and the bandwidth of the sub-window, $B_g = 10$ GHz, to satisfy the THz channel peculiarities, which are common for all the sub-windows. Particularly, the separation between the consecutive pulses N_p needs to sufficiently large to avoid the temporal broadening effects, and the selection of the spectral windows at any distance to satisfy the minimum SINR.

So far the offline parameters of the optimization problem in (46) have been obtained. Next, the distance maximization problem is addressed by solving the rate maximization problem for a given distance iteratively, by which the maximum distance is obtained when the maximum rate reaches the threshold. The detailed solution to the rate maximization problem is detailed in Sec. 3.3.1, in which the power allocation and the rate assignment are decoupled. In particular, four power allocation schemes are considered in our analysis, namely, min power/bit, min N_f^u, water-filling and equal-power. Based on these power

allocation schemes, the number of frames on each sub-window can be obtained, which completes the solution of the distance maximization problem.

3.3.3 Design Tradeoffs

The channel peculiarities and the multi-wideband waveform design are fully captured in the optimization problem. In particular, the SINR-per-bit in (48) and the data rate in the constraint (49) are obtained based on the functions of the channel in (2), the waveform signal in (21), and the interferences in (30) and (86).

The optimization problem has two variables that appear in the waveform signal in (21) and are closely interacted with each other, which are: the transmit power, P_u, and the number of frames, N_f^u, over each sub-window, which The number of frames can also be understood as the rate computation over each sub-window. The increase of the transmit power allows a smaller number of frames in one sub-window to satisfy the SINR-per-bit constraint. This consequently increases the rate on that particular sub-window. However, the relationship between the transmit power and the data rate on one sub-window is not linear. Moreover, increasing the transmit power in one sub-window suggests a reduction of the available power to other sub-windows. From another perspective, large numbers of frames on the sub-windows require less power to fulfill the SINR-per-bit constraint. Although the rate over each sub-window is reduced, more sub-windows can be utilized in this case.

To increase the communication distance and the rate over the THz band, the tradeoff between the transmit power and the number of frames on the sub-windows, that are realized in the four allocation schemes in Sec. 3.3.1, need to be investigated throughly. Furthermore, the impact of the propagation peculiarities in the THz band such as the antenna gains, path gains, the delay spread and the temporal broadening influence the wideband waveform design and ultimately the THz system performance. Lastly, the complexity of this algorithm is significantly reduced since the allocation of the transmit power is decoupled with the distribution of the number of frames, i.e., the rates over each sub-window.

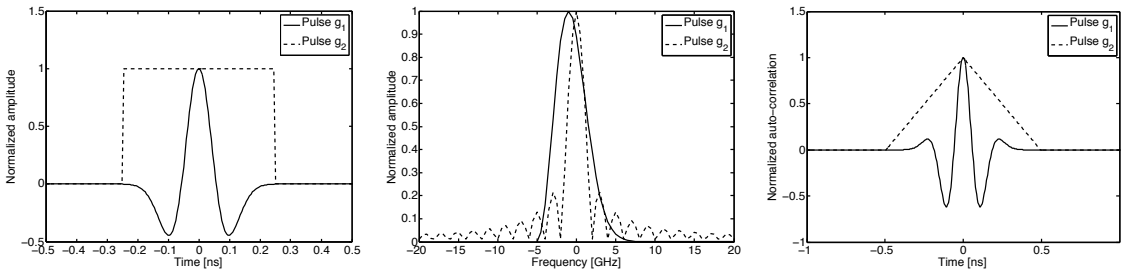

(a) Time response. (b) Frequency response. (c) Auto-correlation function.

Figure 11. The wideband THz pulse waveform properties.

3.4 Numerical Analysis

In this section, we perform numerical analysis on the multi-wideband waveform design for the multi-path propagation and directional transmission, respectively. In particular, the SINR and the BER for the different transmit power, the different number of frames, and the different waveforms are studied. By using the THz band channel and the waveform design, the rate is analyzed, which is dependent on the transmit power, the communication distance, and the power allocation scheme. Finally, the improvement of the distance to achieve the data rate requirement, R_{th}, is investigated.

The simulation parameters are $P_{\text{Tx}} = 10$ dBm, $\gamma_{\text{th}} = 10$ dB, and $R_{\text{th}} = 10$ Gbps for the multi-path and 30 Gbps for the directional propagations. These parameter values are consistent with the state-of-art system and hardware design in the Terahertz band, in [28, 75]. The feasible solutions are obtained by using these parameters.

Two types of pulses are used in the simulation for comparison. The pulse shapes are given by [76]

$$g_1(t) = \left(1 - \frac{25\pi t^2}{T_p^2}\right) \mathrm{e}^{-12.5\pi t^2/T_p^2}, \tag{51}$$

$$g_2(t) = \frac{1}{\sqrt{T_p}}, \quad \text{for } -0.5T_p \le t \le 0.5T_p. \tag{52}$$

The pulses in the time domain and the frequency domain are plotted in Fig. 11(a) and 11(b), respectively. g_1 has a narrow time response and thus a wide frequency response. The bandwidth for g_1 is 10 GHz. In contrast, the rectangular pulse g_2 has the main lobe is

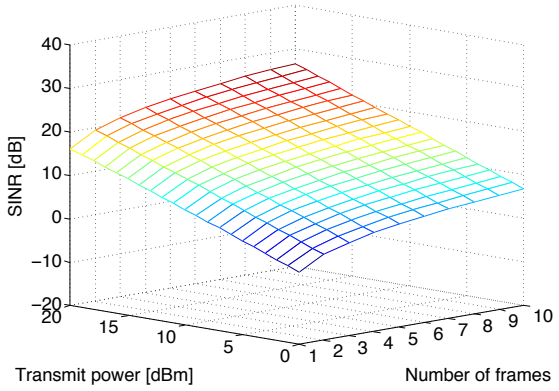

(a) Multi-path propagation with d = 5m, f = 60 GHz.

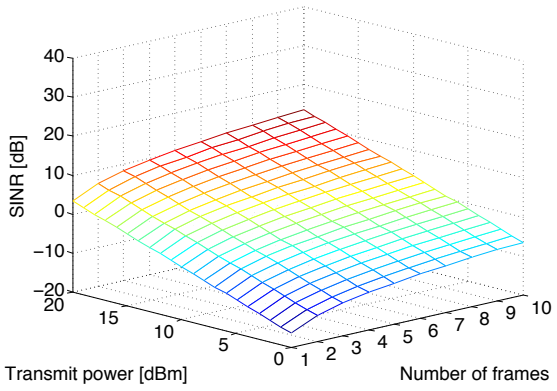

(b) Multi-path propagation with d = 5m, f = 300 GHz.

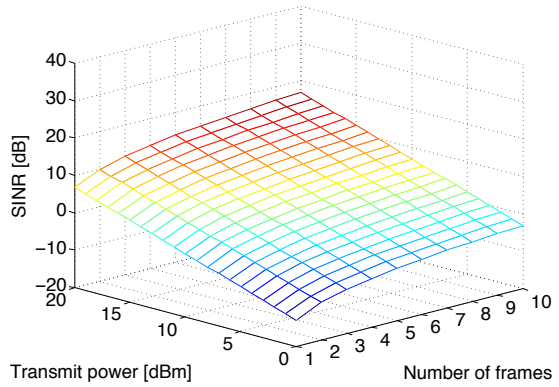

(c) Multi-path propagation with d = 1m, f = 1 THz.

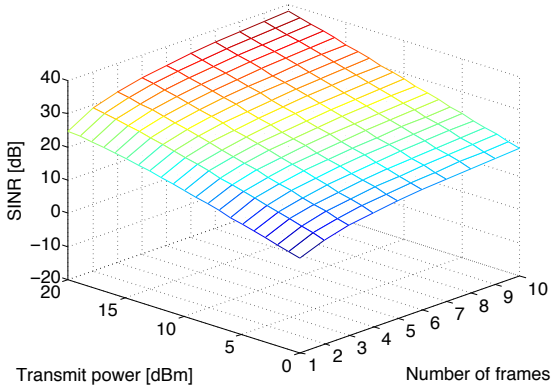

(d) Directional transmission with d = 30m, f = 300 GHz.

Figure 12. SINR for the different distances and frequencies.

4 GHz wide and many sidelobes appear even at 20 GHz around the center frequency. The normalized power leakage values are 0.18% and 17.47% for the two pulses, respectively. This would cause the IBI in (86). Moreover, the auto-correlation functions of the two pulses are demonstrated in Fig. 11(c), whose values at mT_p are used in the computation of the ISI in (30).

3.4.1 SINR

By using (33) and (38), the SINR values for the different transmit power and the different number of frames are investigated. The observations are summarized as follows. First, the SINR increases with the transmit power and the number of frames, although the ISI and IBI rise at the same time. In Fig. 12(a), the SINR for the multi-path propagation at the

distance of 5m and at the sub-window of 60 GHz is shown. To reach the targeted signal strength requirement, for example $\gamma_{\text{th}} = 10$ dB, the possible solutions to the constraint (48) are $\{N_f^u = 1, P_u = 14 \text{ dBm}\}$, $\{N_f^u = 10, P_u = 4 \text{ dBm}\}$ and $\{N_f^u = 3, P_u = 9 \text{ dBm}\}$.

Second, as the frequency increases, the THz band channel has higher path loss over the same distance. The resulting SINR reduces since the path gains decrease in the SINR express in (33), as shown in Fig. 12(b). To achieve the same signal strength, the minimum number of frame becomes 5 instead of 1 for the 60 GHz case, with the transmit power of 20 dBm. On the other hand, the minimum transmit power is 17 dBm instead of 9 dBm for the 60 GHz case, with the number of frames of 10. If the frequency further increases to 1 THz, $\gamma_{\text{th}} = 10$ dB cannot be satisfied for $d = 5$m. Hence, Fig. 12(c) shows the SINR for $d = 1$m, and the possible solutions to (48) are $\{N_f^u = 3, P_u = 19 \text{ dBm}\}$, $\{N_f^u = 9, P_u = 14 \text{ dBm}\}$ and $\{N_f^u = 7, P_u = 15 \text{ dBm}\}$.

Third, with the use of the high-gain antennas, the SINR is greatly improved. In particular, when $G_t = G_r = 20$ dB, the communication distance can be enhanced to $d = 30$m for $f = 0.3$ THz, as shown in Fig. 12(d). In the SINR expression in (38), the ISI is omitted since only the LoS path is considered for the directional transmission. Based on these parameter values, the SINR requirement is satisfied for the solutions $\{N_f^u = 1, P_u = 2 \text{ dBm}\}$ and $\{N_f^u = 2, P_u = 0 \text{ dBm}\}$, among others. Fourth, the influences of the transmit power and the number of frames are comparable. In particular, when the transmit power increases from 0 dBm to 10 dBm, the SINR value increases by 10 dB. This improvement of SINR is approximately the same if we send 10 frames instead of 1 frame for one symbol, as given in (21).

To maintain the required SINR, the tradeoff between the power efficiency and the rate effectiveness needs to be determined, since SINR is affected by the combination of the number of frames and the transmit power.

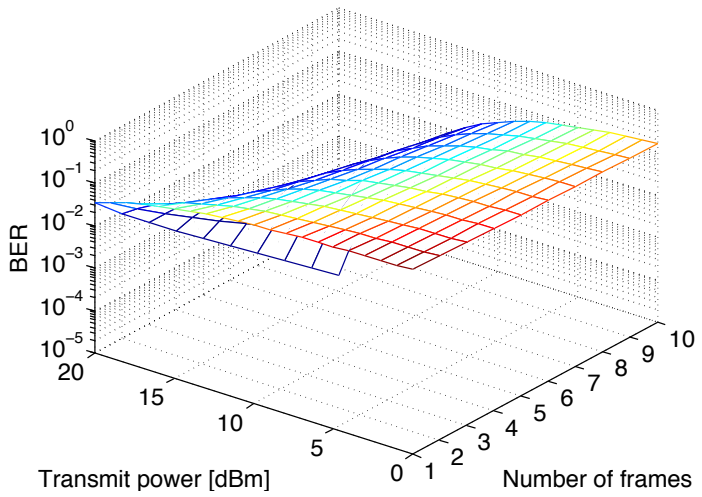

Figure 13. BER for the multi-path propagation with d = 5m, f = 300 GHz

3.4.2 BER

Then, the BER is related to the SINR by using (40) and (41). The BER decreases with the increase of the SINR. Consequently, the BER decreases with the increase of the transmit power and the number of frames. To realize the error rate below 10^{-3}, the SINR needs to be greater or equal to 9 dB, while in particular, $\gamma_{\text{th}} = 10$ dB suggests BER $= 3.9 \times 10^{-4}$. For the multi-path propagation at 0.3 THz over 5m, the BER is given in Fig. 13. A drastic decrease is observed for the BER and when N_f^u is no less than 4 and P_u is no less than 16 dBm, the BER is below 10^{-3}.

3.4.3 Power Allocation Schemes

By using the THz band channel and the waveform design, the rate is analyzed in this section. Four power allocation schemes are considered for $d = 1$m and $P_{\text{Tx}} = 10$ dBm. The first scheme that minimizes power/bit allows an efficient utilization of the transmit power, as shown in Fig. 14(a). With the increase of the operating frequency, the path loss increases and the SINR decreases. To achieve the same power-per-bit, the allocated power increases steadily. More power is allocated to the higher frequency bands. The second scheme in in Fig. 14(b) minimizes the number of frames over each sub-window. The transmit power is allocated only to the sub-windows with the small carrier frequencies, i.e., up to 0.53 THz,

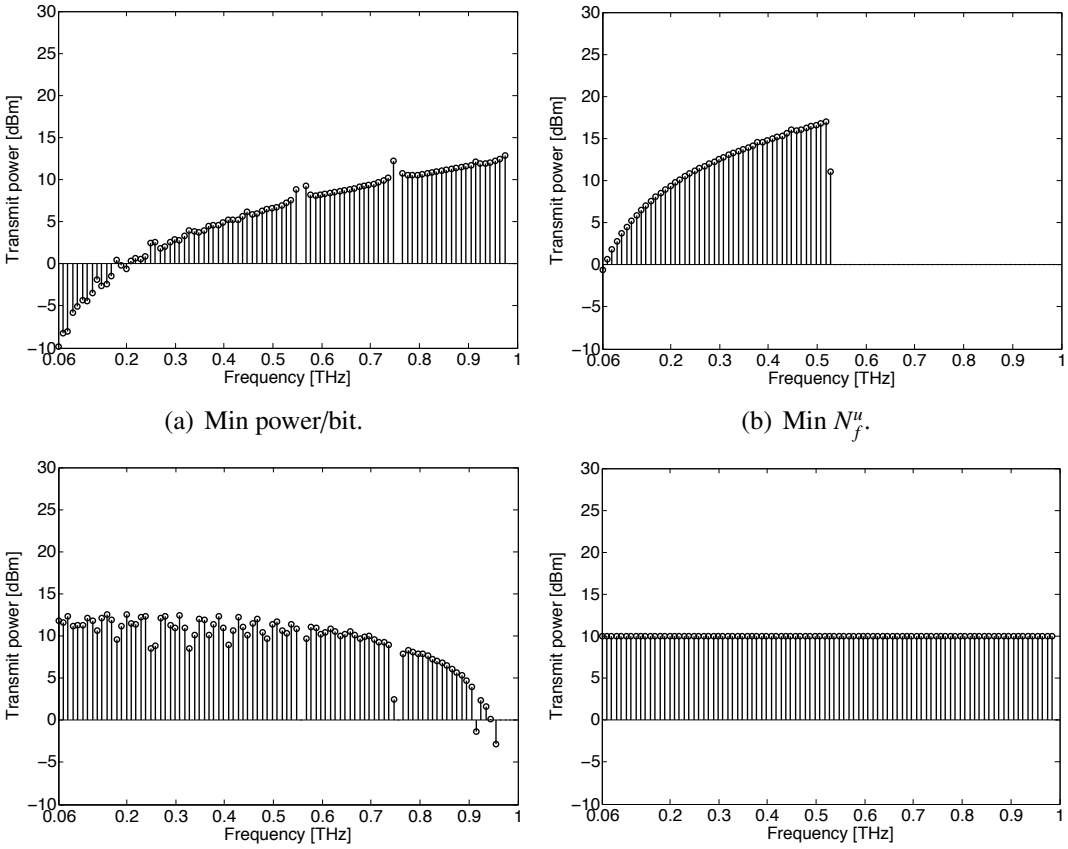

(a) Min power/bit.

(b) Min N_f^u.

(c) Water-filling.

(d) Equal-power.

Figure 14. Transmit power over the 0.06 - 1 THz spectrum for the different allocation schemes, with d = 1m, P_{Tx} = 10 dBm.

while no power is provided for the higher frequency bands, which is equivalent to the truncated channel inversion scheme [73]. The third scheme follows the water-filling principle, which allocates more power to the sub-windows that have better SINR, as illustrated in Fig. 14(c). However, this scheme requires a feedback path to supply the channel information at the transmitter [61], which is very costly since the channel variation can be very fast over time at THz frequencies due to the mobility or the transmission medium changes. The fourth schemes allocates the transmit power equally over the sub-windows from 0.06 THz to 1 THz, as shown in Fig. 14(d). This scheme allows the offline allocation of the transmit power and consequently the number of frames.

3.4.4 Achievable Rates

The total rate over the 0.06 – 1 THz band for the multi-path propagation is analyzed for the aforementioned four power allocation schemes with $P_{\text{Tx}} = 10$ dBm, as shown in Fig. 15(a). When the distance is below 4m, the equal-power scheme outperforms the others and requires no channel information. However, the decreasing rate of this scheme is the largest. The first scheme and the water-filling scheme have very close performance until $d = 5$m. Above this distance, the path loss and the frequency selectivity degrade significantly. As a result, the fist scheme has the largest throughout since it has the most efficient utilization of the transmit power over the 0.06 – 1 THz band. In contrast, the second scheme allocates the transmit power up to 0.25 THz (see Fig. 14(b)), and has the worst rate performance among the four schemes. Quantitatively, at $d = 1$m, the rate values for the four schemes are 18.2 Gbps, 11.6 Gbps, 20.1 Gbps, and 27.3 Gbps, respectively. Furthermore, the decreasing rates for the four schemes are approximated as 1.67 Gbps/m, 1.02 Gbps/m, 2.06 Gbps/m, and 3.00 Gbps/m, separately, from 1m to 10m.

In addition to the multi-path propagation, we analyze the rate for the directional transmission case, by exploiting the spectral windows. Surprisingly, the rate performance of the first scheme that minimizes $P_u \cdot N_f^u$ degrades significantly and is the worst among others. This is due to the fact that the first scheme allocates more power to the sub-windows that have worse attenuations, as shown in Fig. 14(a). This power allocation scheme performs well for the multi-path propagation, when the SINR at the receiver is low. However, for the directional transmission at 20m, this scheme uses 16.06 dBm of the total power, which is 4.3% of P_{Tx}. The underexploited use of the transmit power leads to the severe rate degradation of this scheme. On the contrary, the other three schemes take the advantages of the antenna gains, (i.e., $G_t = G_r = 20$ dB). The rate and the communication distance are significantly enhanced. Fig. 15(b) shows the rate over the distance up to 50m. The min N_f, water-filling and equal-power schemes perform approximately the same in this case. However, the equal-power scheme allows the offline computation of the transmit power

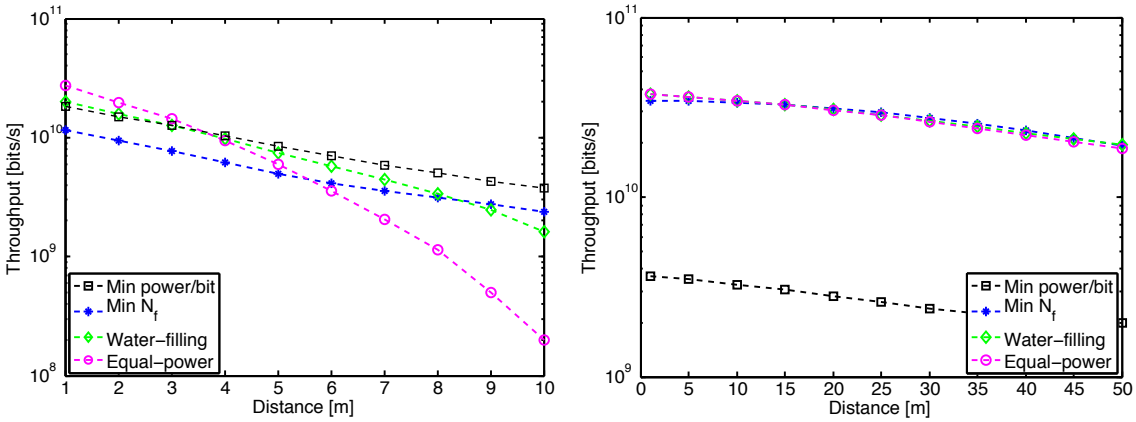

(a) Multi-path propagation. (b) Directional transmission.

Figure 15. Data rates for the different allocation schemes over 0.06 - 1 THz band, and $P_{\mathrm{Tx}} = 10$ dBm.

and hence the number of frames. As a result, the equal-power scheme is desired for the directional transmission.

We note that there exist some numerical discrepancies for these data rate results. For example, the water-filling scheme performs unexpectedly worse than the other schemes. Mainly, the reasons are two-folded. First, the problem is solved as a sub-optimal solution, which suggests that even the water-filling scheme here is not optimal. Second, the discrete values of the data rates as the inverse of the number of frames also leads to the numerical errors. Additional sub-optimal or low-complexity optimal solutions can be developed as future research.

In Fig. 16, the rate values are evaluated for the different mean transmit power, P_{Tx}, in (47), by adopting the first power allocation scheme in the multi-path propagation. The decreasing rates of the rate are comparable for the different transmit power. In particular, the average rate over the distance 1m to 10m is 9.07 Gbps, when the mean transmit power is 10 dBm. The rate values reduce by 29.0% and 50.5%, to 6.44 Gbps, and 4.49 Gbps, when the transmit power changes to 5 dBm and 1 dBm, respectively. If we use g_2, due to the increase of the ISI and IBI, the rate by using the rectangular pulse is slightly worse than g_1. In particular, the average rates are 9.00 Gbps, 6.39 Gbps and 4.41 Gbps for the given transmit power. From this analysis, the pulse type makes insignificant influence on

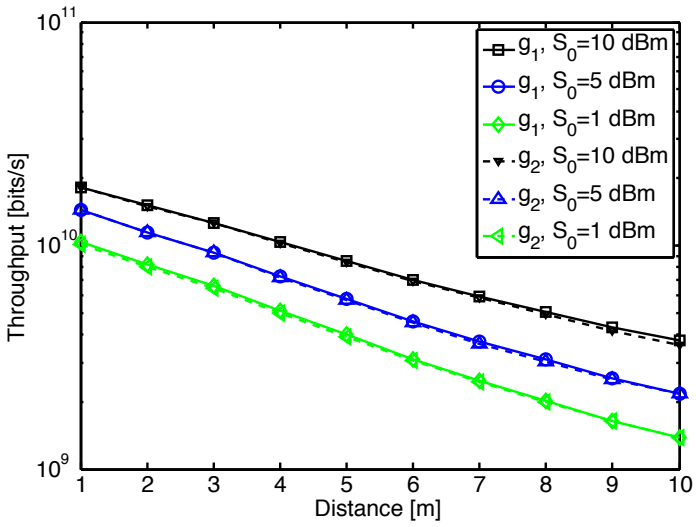

Figure 16. Data rates for the different transmit power and waveforms. The min power/bit scheme is used in the multi-path propagation.

the system performance.

3.4.5 Distance Improvement

Based on the analysis on the wideband signal model, the SINR, and dynamic allocation of the power and the number of frames, we obtain the solutions to the optimization problem in 3.3.2. By using the four allocation schemes, the maximum distances that can be supported are shown in Fig. 17(a) for the multi-path propagation, and in Fig. 17(b) for the directional transmission, respectively. With the transmit power $P_{\text{Tx}} = 10$ dBm, the largest distance to support $R_{\text{th}} = 10$ Gbps for the multi-path propagation is 4m, which is realized via the first allocation scheme. As seen in Fig. 17(a), the scheme to minimize power-per-bit outperforms than the other three allocation schemes, except when $P_{\text{Tx}} = 1$ dBm, the second scheme to minimize the number of frames can reach the largest distance of 1.28m. Compared to the fixed power scheme, the distance is improved by 25% for 1 dBm and 2.6% for 10 dBm.

On the other hand, when the high-gain antennas are used, the first scheme that minimizes power-per-bit under-exploits the transmit power severely. Instead, the other three

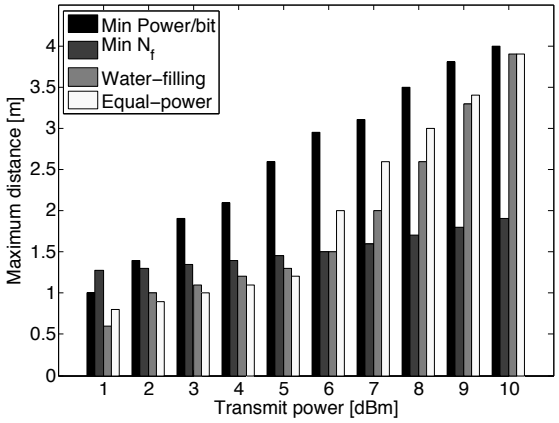

(a) $R_{\text{th}} = 10$ Gbps for the multi-path propagation.

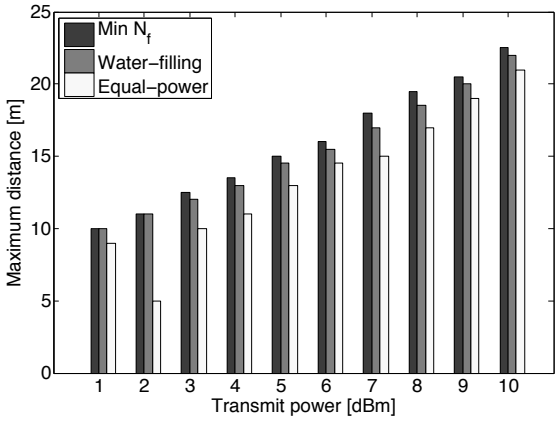

(b) $R_{\text{th}} = 30$ Gbps for the directional transmission. The min power/bit scheme under-exploits the transmit power severely and is excluded for comparison.

Figure 17. Maximum distance for the different transmit power, over 0.06 - 1 THz band.

schemes have comparable performances and the second scheme that minimizes the number of frames slightly outperforms. In terms of the maximum distance that achieves $R_{\text{th}} = 30$ Gbps, the second scheme reaches 22.5m when $P_{\text{Tx}} = 10$ dBm. This coverage reduces with the transit power, and drops to 10m when $P_{\text{Tx}} = 1$ dBm. Although the equal-power scheme achieves $5\% - 10\%$ less distance than the water-filling and the min N_f schemes, it has the lowest complexity by allowing the offline power allocation and rate computation.

3.5 Conclusions

In this chapter, we proposed a multi-wideband waveform design for the THz band, which includes the features of the pseudo-random time-hopping sequence and the polarity randomization, and allows the dynamical variation of the rate and the transmit power on each sub-window. Moreover, we derived the ISI and the IBI and provided the closed-form expressions of the SINR and BER for the developed multi-wideband waveform. Based in the system model and the waveform design, we formulated an optimization framework to solve for the multi-wideband waveform design parameters of the transmit power and the number of frames, with the aim to maximize the communication distance while satisfying the rate and the transmit power constraints. Four sub-optimal solutions are proposed and compared

via extensive numeral analysis.

The results showed that the SINR increase with the transmit power and the number of frames in the multi-wideband waveform design, at the cost of the consumption of the power and the decrease of the rate. With the transmit power of 10 dBm, the largest distance to support 10 Gbps for the multi-path propagation is 4m, which is realized via the power allocation scheme to minimize the power/bit on each sub-window and is 10% improvement over the fixed scheme. However, for the directional transmission, this scheme under-exploits the transmit power severely. Instead, the allocation scheme that minimizes the number of frames outperforms. In terms of the maximum distance that achieves 30 Gbps, this scheme reaches 22.5m. Although the equal-power scheme achieves $5\% - 10\%$ less distance than the water-filling and the min N_f schemes, it has the lowest complexity by allowing the offline power allocation and rate computation.

CHAPTER 4

TIMING ACQUISITION ALGORITHMS AND ERROR ANALYSIS FOR PULSE-BASED WIRELESS SYSTEMS

Tailored for the unique properties of pulse-based communications in the THz band, two timing acquisition algorithms are proposed and analyzed thoroughly in this chapter. First, a LSR synchronization algorithm is proposed, by extending the theory of sampling signals with finite rate of innovation in the communication context and exploiting the properties of the annihilating filter. Second, a ML approach for timing acquisition is developed, which searches for the timing offsets by adopting a two-step acquisition procedure based on the ML criterion. For evaluation, the error performance and the resulting BER sensitivity to the timing errors in the two algorithms are both analytically and numerically studied. The simulation results show that the LSR algorithm has high performance with uniform sampling at $1/20$ of the Nyquist rate when the SNR is high (i.e., greater than 10 dB benefiting from high antenna gains). Moreover, the LSR algorithm can also effectively mitigate the temporal broadening effect due to the frequency-selectivity of the THz channel. Complementary to this, the ML-based algorithm is well suitable in the low SNR case with a half-reduced search space.

4.1 Motivation and Related Work

The THz band communication has been an attractive subject of study these years. The contributions in the literature range from the antenna and transceiver technologies [27], to the channel modeling [56, 28], and beamforming techniques [77]. In particular, ultra-short pulse-based modulation is proposed to capture the expected capabilities of low-complexity THz signal generators [65, 78]. Following this direction, we recently proposed a multi-wideband pulse-based waveform design for distance-adaptive THz band communications [79]. However, to the best of our knowledge, there are only few solutions which are proposed for

synchronization in the THz band. In [80], a non-coherent receiver architecture based on a continuous time moving average symbol detection scheme is proposed for the THz pulse-based communication. However, the timing information and the threshold value used in this detection-based approach are not analytically provided.

4.2 Terahertz Pulse Waveform and Timing Offsets

Based on the pulse-waveform model in Sec. 3.2, the received channel output is passed through a receiver filter $h_R(t)$, and the filter output is

$$\begin{aligned} y(t) &= \sqrt{P_t} \sum_{i=0}^{I-1} a_i \sum_{k=0}^{N_f-1} g(t - iN_fT_f - kT_f - \tau_0 - t_D - \psi_i) + w(t) \\ &= \sqrt{P_t} \sum_{i=0}^{I-1} a_i \sum_{k=0}^{N_f-1} g(t - iN_fT_f - kT_f - \mu_iT_f - \nu_iT_s) + w(t) \end{aligned} \tag{53}$$

where $g(t)$ and the timing offsets are defined as

$$g(t) = p(t) * h(t) * h_R(t), \tag{54}$$

$$\mu_iT_f + \nu_iT_s = \tau_0 + t_D + \psi_i. \tag{55}$$

In the above equations, $w(t)$ is the white Gaussian noise, $t_D = d_T/c$ stands for the transmission delay, and ψ_i denotes the jittering offset or the random misalignment between the transmitter and receiver clocks, which dynamically varies over symbols. The channel impulse response is denoted by $h(t)$. In (55), μ_i identifies the first frame of a symbol, which amounts to the symbol timing (ST) at a frame level, and suggests that a symbol begins at $t = iN_fT_f + \mu_iT_f$. On the other hand, ν_i indicates the frame timing (FT) at a sample level, and indicates a frame begins at $t = (iN_f + k + \mu_i)T_f + \nu_iT_s$, with $T_s = 1/f_s$ being the sampling interval.

Consequently, the timing acquisition for the THz band communication accounts for the offsets that include (see Figure 18): i) the random starting time, τ_0, ii) the propagation delay, t_D, which is a constant if the transmitter and the receiver are fixed, and iii) the jittering offset, ψ_i, which is different for the different symbols. Equivalently, finding these

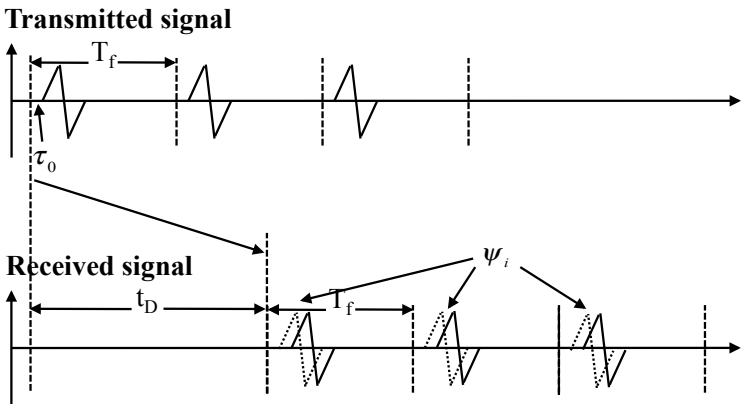

Figure 18. A pulse-based Terahertz transmit and received signal, with $I = 1$ and $N_f = 3$. The timing offsets are shown, which include the random starting time τ_0, the propagation delay t_D, and the jittering offset ψ_i.

parameters is related to solving for μ_i and ν_i.

Based on the received signal in (53) and the channel response, the SNR is calculated as

$$\gamma = \frac{G_t G_r P_t |h|^2 N_f}{P_w}, \tag{56}$$

where P_w refers to the noise power of $w(t)$. As the number of pulses per symbol N_f increases, the SNR increases and consequently, the synchronization performance will improve. However, this is at the cost of the sacrifice of data rates. Therefore, there is a tradeoff among the SNR, the synchronization performance, and the data rate.

4.3 Low-Sampling-Rate (LSR) Algorithm for Timing Acquisition

A signal that is not bandlimited can still be completely reconstructed from uniform samples, provided that the signal has a finite rate of innovation, as proved in [36]. In the communication context, the rate of innovation of a memoryless modulation system is the symbol rate [36]. In many wideband communication systems, the large signal bandwidth prescribes a prohibitively high sampling rate for implementing an optimal matched filter receiver, according to the classical sampling theory. Instead, sampling at or above the rate of innovation can be a solution to such a problem. Indeed, we will show that it is possible to reliably decode a received signal by sampling it at or above the rate of innovation, not at the sampling rate dictated by the bandwidth of the transmit signal. This approach was adopted

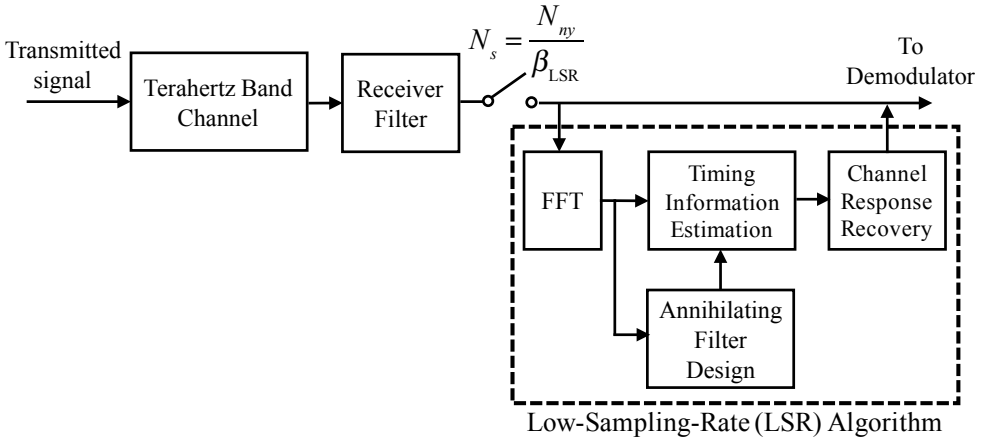

Figure 19. Block diagram of the LSR algorithm.

for ultra-wideband (UWB) systems [81, 82]. In this section, we tailor the algorithm of [81] to the THz band synchronization to cope with the unique channel characteristics at the THz frequencies and the more challenging requirement for the reduction of the sampling rate.

The resulting LSR algorithm is based on the annihilating filter method and the spectral estimation techniques in the frequency domain, and is useful to estimate the timing information at a sub-Nyquist rate. In particular, the annihilating filter method is a well-known tool from spectral estimations [37, 38, 83, 84], while in our context, we derive the analytical sampling formulas in the THz band. The LSR algorithm for timing acquisition is given in Fig. 19, and consists of the three steps, namely, 1) computing the spectral coefficients, 2) designing the annihilating filter, and 3) determining the timing offsets. Moreover, the *LSR factor* is defined as the ratio between the Nyquist sampling rate N_{ny}, and the implemented sampling rate N_s, as $\beta_{\text{LSR}} = N_{ny}/N_s$. We proceed with the description of the three steps of the LSR algorithm as follows.

4.3.1 Computing the Spectral Coefficients

By performing the Fourier transform on the received signal in (53), the equivalent signal model in the frequency domain is expressed as

$$Y(f) = \sqrt{P_t}\sum_{i=0}^{I-1} a_i \sum_{k=0}^{N_f-1} \sqrt{G_t G_r}\frac{c}{4\pi f d_T}\exp\left(-\frac{1}{2}\mathcal{K}(f)d_T\right) \cdot P(f)H_R(f)\exp\left(-j2\pi f\left(iN_fT_f + kT_f\right)\right)\exp\left(-j2\pi f\left(\mu_i T_f + \nu_i T_s\right)\right) + W(f), \quad (57)$$

where $P(f)$, $H_R(f)$ and $W(f)$ represent the frequency responses of $p(t)$ and $h_R(t)$, and $w(t)$, in (53) and (54). Furthermore, we define a sampling interval $T_s = T_f/Q$, where Q is an integer that denotes the number of samples per frame. Hence, ν_i takes integer values in the range of $[0, Q-1]$, while the multiple of T_f is absorbed in μ_i. After sampling at a sampling rate N_s with the time interval T_s, the discrete-time signal of (53) becomes

$$y[n] = \sqrt{P_t}\sum_{i=0}^{I-1} a_i \sum_{k=0}^{N_f-1} g[n - iN_fQ - kQ - \mu_i Q - \nu_i] + w[n]. \quad (58)$$

Next, we transform the signals into the discrete frequency domain, and assume that the bandlimited filter $g(t)$ has a center frequency $f_c = \frac{f_U+f_L}{2}$, where f_U and f_L denote the upper and lower cutoff frequencies. The frequency step is defined as $f_0 = \frac{f_U-f_L}{N}$. In the frequency domain, the N uniformly spaced frequency samples can be expressed as

$$\begin{aligned} Y[n] &= \sum_{i=0}^{I-1} A_i[n] \sum_{k=0}^{N_f-1} \exp\left(-j2\pi f_n\left(iN_fT_f + kT_f\right)\right)\cdot\exp\left(-j2\pi f_n\left(\mu_i T_f + \nu_i T_s\right)\right) + W[n] \\ &= \sum_{i=0}^{I-1} A_i[n] \sum_{k=0}^{N_f-1} \exp\left(-j2\pi f_n T_f\left(iN_f + k + \mu_i\right)\right)\cdot\exp\left(-j2\pi f_n T_s \nu_i\right) + W[n] \\ &= \sum_{i=0}^{I-1}\sum_{k=0}^{N_f-1} A_i[n]\, u_{i,k}^n + W[n], \quad n = 0, 1, \ldots, N-1 \end{aligned} \quad (59)$$

where $f_n = f_L + nf_0$. In the above equations, the expanded expressions for $A_i[n]$ and $u_{i,k}^n$ are given by

$$A_i[n] = a_i\sqrt{G_tG_rP_t}\frac{c}{4\pi f_n d_T}\mathrm{e}^{-\frac{1}{2}\mathcal{K}(f_n)d_T}P(f_n)H_R(f_n), \quad (60)$$

$$u_{i,k}^{n} = \mathrm{e}^{\left(-j2\pi f_n T_f \left(iN_f + k + \mu_i\right)\right) + \left(-j2\pi f_n T_s \nu_i\right)}. \tag{61}$$

Note that $u_{i,k}^{n}$ depends on i and k. By using a polynomial approximation, the coefficients $A_i[n]$ can be expressed as a sum of powers with the exponents of $m \in [0, M-1]$,

$$A_i[n] \approx \sum_{m=0}^{M-1} x_m n^m. \tag{62}$$

Hence, the expression for $Y[n]$ in (59) can be further approximated as

$$Y[n] \approx \sum_{i=0}^{I-1} \sum_{k=0}^{N_f-1} \left(\sum_{m=0}^{M-1} x_m n^m \right) u_{i,k}^{n} + W[n]. \tag{63}$$

4.3.2 Designing the Annihilating Filter

Based on the spectral coefficients, we proceed with designing the annihilating filter, $H_a[m]$. The N spectral coefficients $Y[n]$ are computed according to (63), with $N \geq 2L + 1$. The annihilating filter is designed for guaranteeing

$$\begin{aligned} H_a[n] * Y[n] &= \sum_{l=0}^{L} H_a[l] Y[n-l] \\ &= 0, \text{for } n = 0, 1, \ldots, N-1, \end{aligned} \tag{64}$$

where $L = I \cdot N_f \cdot M$. By exploiting the z-transform properties of $H_a[n]$, the annihilating filter coefficients $H_a(z)$ in the z-domain are

$$\begin{aligned} H_a(z) &= \sum_{l=0}^{L} H_a[l] z^{-l} \\ &= \prod_{i=0}^{I-1} \prod_{k=0}^{N_f-1} \left[1 - p_{i,k}^{0} z^{-1}\right]^{M}, \end{aligned} \tag{65}$$

where $p_{i,k}^{0}$ is a function of the frequency step f_0 and relates to $u_{i,k}^{n}$ as

$$\begin{aligned} p_{i,k}^{0} &= \exp\left(-j2\pi f_0 T_f \left(iN_f + k + \mu_i\right) - j2\pi f_0 T_s \nu_i\right) \\ &= \left(u_{i,k}^{n} \cdot \exp\left(j2\pi f_L \left(T_f \left(iN_f + k + \mu_i\right) + T_s \nu_i\right)\right)\right)^{\frac{1}{n}}. \end{aligned} \tag{66}$$

Our aim is to explore the properties of the annihilating filter in (65) to solve for the timing offsets. The annihilating filter has the degree of L and $L + 1$ unknown filter coefficients,

which consequently require $L+1$ linear equations to solve for the annihilating filter coefficients. This indicates that $N \geq 2L+1$ samples are needed in $Y[n]$, which is shown in the matrix form of the above equation

$$\begin{pmatrix} Y[L] & Y[L-1] & \cdots & Y[0] \\ Y[L+1] & Y[L] & \cdots & Y[1] \\ \vdots & \vdots & \ddots & \vdots \\ Y[2L] & Y[2L-1] & \cdots & Y[L] \end{pmatrix} \begin{pmatrix} H_a[0] \\ H_a[1] \\ \vdots \\ H_a[L] \end{pmatrix} = \mathbf{0}. \tag{67}$$

To efficiently solve for the annihilating filter coefficients, we can set $H_a[0] = 1$, without loss of generality. Then, the matrix equation can be rearranged as $\mathbf{Y}' \cdot \mathbf{H}'_a = -\mathbf{Y}_1$, where the matrices are defined as

$$\mathbf{Y}' = \begin{pmatrix} Y[L-1] & Y[L-2] & \cdots & Y[0] \\ Y[L] & Y[L-1] & \cdots & Y[1] \\ \vdots & \vdots & \ddots & \vdots \\ Y[2L-1] & Y[2L-2] & \cdots & Y[L] \end{pmatrix}, \tag{68}$$

$$\mathbf{H}'_a = \begin{pmatrix} H_a[1] & H_a[2] & \cdots & H_a[L] \end{pmatrix}^T, \tag{69}$$

$$\mathbf{Y}_1 = \begin{pmatrix} Y[L] & Y[L+1] & \cdots & Y[2L] \end{pmatrix}^T, \tag{70}$$

where $(\cdot)^T$ denotes the transpose operator.

4.3.3 Determining the Timing Offsets

Next, we utilize the derivations above to compute the timing offsets. With the filter coefficients $H_a[m]$, the values of μ_i and ν_i can be estimated by exploiting the pole properties of the annihilating filter. After transforming the annihilating filter impulse response into the z-domain in (65), we relate the filter characteristics to the desired timing parameters.

Denoting the poles as $\{\hat{p}^0_{i,k}\}$, the estimated ST and FT offsets are solved as

$$\hat{\mu}_i = \left\lfloor \frac{\angle \hat{p}^0_{i,k}}{-j2\pi f_0 T_f} \right\rfloor - iN_f - k, \tag{71}$$

$$\text{and} \quad \hat{\nu}_i = \left\lfloor \frac{\angle \hat{p}^0_{i,k}}{-j2\pi f_0 T_s} \right\rfloor - Q\left(iN_f + k + \hat{\mu}_i\right), \tag{72}$$

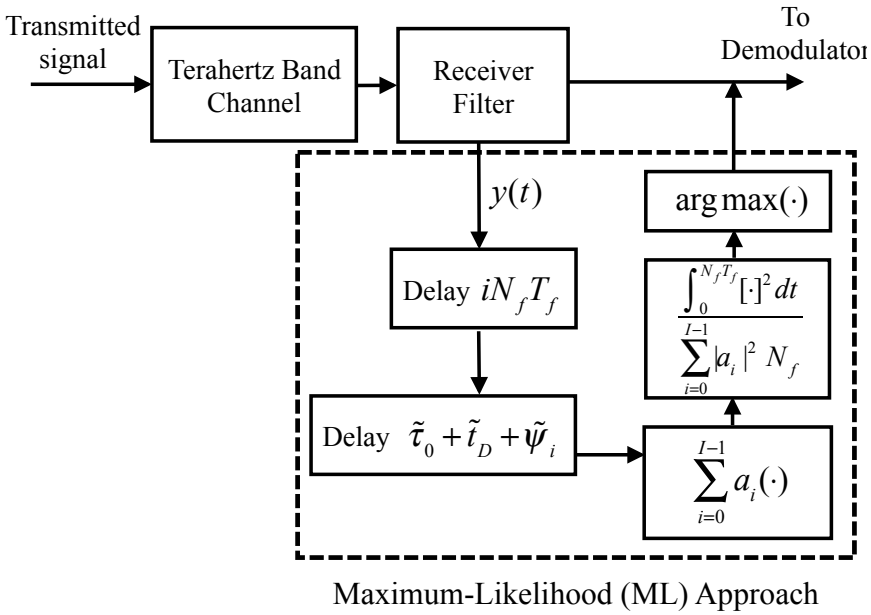

Figure 20. Block diagram of the ML approach.

where $\lfloor\cdot\rfloor$ denotes the flooring operator. For (71) and (72), we search for the poles $\hat{p}_{i,k}^0$ that are closest to the unit circle [34].

This algorithm is reliable when the noise level is low and the antenna gains are high. In THz band communications, beamforming techniques as well as the pulse combining gain can effectively improve the SNR and hence decrease the noise effect. Nevertheless, the problem of numerical ill-conditioning may arise by using this approach, mainly because root-finding is not robust to noise. Alternatively, instead of finding the roots, matrix manipulations can be performed, exploiting the properties of the signal subspace [35, 37, 83]. However, a major computational cost for this method arises in the singular value decomposition procedure in the matrix manipulations, which is an iterative algorithm with very high computational costs and is not favored in this work.

4.4 Maximum-Likelihood-Based Timing Acquisition Approach

The LSR algorithm developed in the previous section allows choosing a sub-Nyquist sampling rate and achieves good timing acquisition performance when the SNR is high. As

a complementary approach, for the low SNR case (i.e., less than 10 dB), the ML criterion [39, 40, 41] is adopted to derive a timing acquisition algorithm tailored to the pulse-based THz band communication in this section. In particular, a two-step acquisition procedure and a weighted construction are used in this process in the absence of timing information. Starting with the THz communication model (53), we introduce a vector with trial values of the unknown timing offsets as $\left(\tilde{\tau}_0, \tilde{t}_D, \tilde{\psi}_i\right)^T$ and the hypothetical channel-dependent received pulse as $\tilde{g}(t)$, which correspond to the parameters in (54) and (55). We assume the absence of inter-symbol interference in the directional transmission, and treat the noise component $w(t)$ in the received signal according to (53) as a zero-mean Gaussian process with constant power spectral density over the receiver-filter bandwidth. Moreover, we describe $\tilde{z}(t)$ as the noise-free component of the trial received signal, as

$$\tilde{z}(t) = \sqrt{P_t} \sum_{i=0}^{I-1} a_i \sum_{k=0}^{N_f-1} \tilde{g}(t - iN_f T_f - kT_f - \tilde{\tau}_0 - \tilde{t}_D - \tilde{\psi}_i). \tag{73}$$

We define $\tilde{g}_1(t) = \sum_{k=0}^{N_f-1} \tilde{g}(t - kT_f)$. The ML rule is equivalent to searching $\left(\tilde{\tau}_0, \tilde{t}_D, \tilde{\psi}_i\right)^T$ and $\tilde{g}_1(t)$ for a minimum of $\|y(t) - \tilde{z}(t)\|^2$, which equivalently maximizes

$$\begin{aligned}
&\Lambda\left[y(t)|\left(\tilde{\tau}_0, \tilde{t}_D, \tilde{\psi}_i\right)^T, \tilde{g}_1(t)\right] = 2\int_0^{IN_fT_f} y(t)\tilde{z}(t)dt - \int_0^{IN_fT_f} [\tilde{z}(t)]^2\, dt \\
&= 2\int_0^{IN_fT_f} y(t)\sqrt{P_t}\sum_{i=0}^{I-1} a_i \sum_{k=0}^{N_f-1} \tilde{g}(t - iN_fT_f - kT_f - \tilde{\tau}_0 - \tilde{t}_D - \tilde{\psi}_i)dt \\
&- \int_0^{IN_fT_f} \left[\sqrt{P_t}\sum_{i=0}^{I-1} a_i \sum_{k=0}^{N_f-1} \tilde{g}(t - iN_fT_f - kT_f - \tilde{\tau}_0 - \tilde{t}_D - \tilde{\psi}_i)\right]^2 dt \\
&= 2\int_0^{IN_fT_f} y(t)\sqrt{P_t}\sum_{i=0}^{I-1} a_i\tilde{g}_1(t - iN_fT_f - \tilde{\tau}_0 - \tilde{t}_D - \tilde{\psi}_i)dt \\
&- \int_0^{IN_fT_f} \left[\sqrt{P_t}\sum_{i=0}^{I-1} a_i\tilde{g}_1(t - iN_fT_f - \tilde{\tau}_0 - \tilde{t}_D - \tilde{\psi}_i)\right]^2 dt
\end{aligned} \tag{74}$$

In this objective function, we assume that the training symbols a_i are uncorrelated with each other. Moreover, we recognize that one symbol waveform is confined with the non-zero support over $[0, N_f T_f]$. Hence, the objective function can be further rearranged

$$\begin{aligned}\Lambda\left[y(t)|\left(\tilde{\tau}_0, \tilde{t}_D, \tilde{\psi}_i\right)^T, \tilde{g}_1(t)\right] &\approx 2\sqrt{P_t}\sum_{i=0}^{I-1} a_i \int_0^{N_f T_f} y(t + iN_f T_f + \tilde{\tau}_0 + \tilde{t}_D + \tilde{\psi}_i) \\ &\cdot \sum_{k=0}^{N_f-1} \tilde{g}(t - kT_f)dt - P_t \sum_{i=0}^{I-1}|a_i|^2 \int_0^{N_f T_f}\left[\sum_{k=0}^{N_f-1}\tilde{g}(t-kT_f)\right]^2 dt \\ &\approx 2\sqrt{P_t}\sum_{i=0}^{I-1} a_i \int_0^{N_f T_f} \tilde{g}_1(t)\cdot y(t + iN_f T_f + \tilde{\tau}_0 + \tilde{t}_D + \tilde{\psi}_i)dt - P_t\sum_{i=0}^{I-1}|a_i|^2\int_0^{N_f T_f}\left[\tilde{g}_1(t)\right]^2 dt.\end{aligned} \tag{75}$$

The ML-based time acquisition problem can be solved by adopting a two-step procedure. In particular, the objective function can be rearranged by taking $\tilde{g}_1(t)$ as a nuisance, as

$$\left(\tilde{\tau}_0, \tilde{t}_D, \tilde{\psi}_i\right)^T = \arg\max\left\{\underset{\tilde{g}_1(t)}{max}\left\{\Lambda\left[y(t)|\left(\tilde{\tau}_0, \tilde{t}_D, \tilde{\psi}_i\right)^T, \tilde{g}_1(t)\right]\right\}\right\}. \tag{76}$$

To solve the inner maximization in (76), we fix $\left(\tilde{\tau}_0, \tilde{t}_D, \tilde{\psi}_i\right)^T$ and set $\frac{\partial\Lambda}{\partial\tilde{g}_1(t)} = 0$ in (75) with t confined over $[0, N_f T_f]$. The resulting optimal estimate of the received pulse waveform $\tilde{g}_1(t)$ is obtained as

$$\tilde{g}_1(t) = \frac{1}{\sum_{i=0}^{I-1}\sqrt{P_t}|a_i|^2 N_f}\cdot\sum_{i=0}^{I-1} a_i y(t + iN_f T_f + \tilde{\tau}_0 + \tilde{t}_D + \tilde{\psi}_i). \tag{77}$$

This estimate can be interpreted as a weighted construction with the normalized known training symbols $a_i/\sum_{i=0}^{I-1}|a_i|^2$ as the weighting coefficients. By substituting (77) into (75) and (76), we reach the solution to the timing acquisition problem. As a result, the timing offset is obtained

$$\left(\tilde{\tau}_0, \tilde{t}_D, \tilde{\psi}_i\right)^T = \arg\max\left\{\frac{1}{\sum_{i=0}^{I-1}\sqrt{P_t}|a_i|^2 N_f}\int_0^{N_f T_f}\left[\sum_{i=0}^{I-1} a_i y(t + iN_f T_f + \tilde{\tau}_0 + \tilde{t}_D + \tilde{\psi}_i)\right]^2 dt\right\}. \tag{78}$$

The desired estimate maximizes the energy in (78). The block diagram to implement the ML approach is illustrated in Fig. 20. The cost of the ML approach is affected by the size

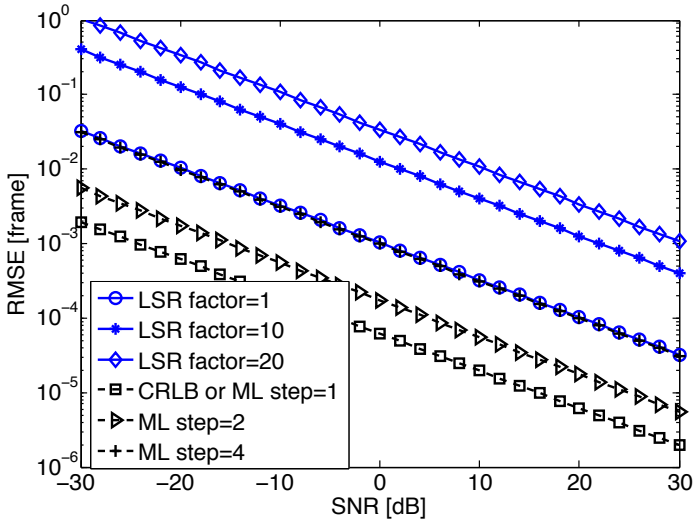

Figure 21. Timing acquisition RMSE in comparison with the CRLB.

of the search space, and can be reduced by enlarging the time step to a multiple of T_s. The tradeoff between the synchronization performance and the complexity is investigated numerically in Sec. 4.6.

4.5 Error Analysis

In this section, we first provide an estimation error analysis in terms of the root-mean-square-error (RMSE) and the CRLB analytically and numerically. Then, we derive an analytical expression of the BER as a function of the timing acquisition errors.

4.5.1 RMSE and Theoretical Bounds

To evaluate the developed algorithms, we analyze the RMSE of timing estimates and compare with the CRLB. First, we define the estimation error in the i^{th} symbol of the signal as

$$\tilde{\epsilon}_i = (\tilde{\tau}_0 + \tilde{t}_D + \tilde{\psi}_i) - (\tau_0 + t_D + \psi_i). \tag{79}$$

Over the I symbols of the transmitted signal, the normalized RMSE of the estimation error $\tilde{\epsilon}_i$ at the frame level is given by

$$\text{RMSE}(\tilde{\epsilon}) = \frac{\sqrt{\frac{1}{I}\sum_{i=0}^{I-1} \tilde{\epsilon}_i^2}}{T_f} \tag{80}$$

To approximate the RMSE of the LSR algorithm by a function of the SNR, we employ an analytical expression developed via a first order perturbation analysis [85],

$$\begin{aligned}\mathrm{RMSE}\{\tilde{\epsilon}\} &\approx \sqrt{\frac{2M+1}{6(\pi f_0)^2 \cdot (N-M)^2(M^2+M)\cdot \mathrm{SNR}}} \\ &\approx \sqrt{\frac{1}{3M(\pi f_0)^2 \cdot N^2 \cdot \mathrm{SNR}}},\end{aligned} \tag{81}$$

where the approximation in (81) is a function of the frequency step, f_0, the polynomial degree, M, and the total number N of frequency samples $Y[n]$ in (59). By contrast, the CRLB suggests a lower bound on achievable RMSE for any unbiased estimation methods [86], as

$$\mathrm{CRLB}\{\tilde{\epsilon}\} = \sqrt{\frac{3}{2(\pi f_0)^2 \cdot N^3 \cdot \mathrm{SNR}}}. \tag{82}$$

Note that the performance of the ML estimator is close to the CRLB and can achieve this bound asymptotically [76, 87]. Hence, we only compare the RMSE performance of the LSR algorithm with the CRLB, as shown in Fig. 21. The LSR algorithm provides a very good estimation performance, and its RMSE approaches the CRLB as the polynomial degree is comparable to the number of frequency samples, i.e., $N \geq 2IN_fM+1$, as described in Sec. 4.3.2. In particular, by increasing the sampling rate X times for the same SNR, the RMSE of the LSR algorithm decreases by a factor of $M^{1/2} \cdot X$, while the CRLB reduces by a greater factor of $X^{3/2}$ as can be deduced from (82). These results are consistent with the observations in [81].

In this analysis, we select the degree of the polynomial estimation as $M = 20$ in (63). As the LSR factor (β_{LSR} in Fig. 19) increases from 1 to 10 and 20, the performance difference between the LSR algorithm and the CRLB increases. At SNR=30 dB, the approximated RMSEs are 3×10^{-5}, 4×10^{-4} and 1×10^{-3} respectively, while the CRLB or equivalently, the performance of the ML algorithm with a time step of 1, is equal to 2×10^{-6}. The RMSE performance becomes worse as the SNR decreases, and is further away from the CRLB as the LSR factor increases. Furthermore, by comparing with the simulation results, the approximations are in good agreements particularly for high SNR. In addition, the error

performance of the ML method is studied, for different time steps ranging from 1, 2 to 4. The ML method generally outperforms the LSR approach. At SNR=−30 dB, the RMSE increases from 2×10^{-3}, 5×10^{-3} to 3×10^{-2}.

4.5.2 BER Sensitivity

In the following, we evaluate the BER performance of the THz receiver equipped with the above timing acquisition methods. The goal is to assess the BER sensitivity caused by the timing acquisition errors while assuming ideal channel estimation. Particularly for the pulse-based systems, by incorporating the interference and the noise effects jointly, the Q-function of the SNR was shown to capture the error behavior [76, 88, 89]. In light of the received signal in (53), the timing errors model in (55), and the SNR expression in (87), the BER is given by

$$\rho_i(\mu_i, \nu_i) = Q\left(\sqrt{\frac{G_t G_r P_t |h|^2 N_f R_p^2(\mu_i T_f + \nu_i T_s)}{P_w}}\right), \tag{83}$$

where we consider a_i takes a value from $\{+1, -1\}$ with equal probabilities. In (83), $R_p(t)$ describes the normalized auto-correlation function of the THz pulse, $p(t)$, as

$$R_p(\tau) = A_R \int_{-\infty}^{+\infty} p(t)p(t-\tau)dt, \tag{84}$$

where A_R is the normalizing factor. If the timing acquisition is perfect, the best-case BER is

$$\rho_i(0,0) = Q\left(\sqrt{\frac{G_t G_r P_t |h|^2 N_f}{P_w}}\right), \tag{85}$$

where the term inside the Q-function is the square root of the SNR. According to the above equation, the BER decreases for higher SNR, smaller timing acquisition errors, and larger number of pulses per symbol.

4.6 Performance Evaluation

In this section, we assess the LSR synchronization algorithm and the ML-based approach in terms of the timing offset estimation performance, based on Monte Carlo simulations. All

Table 2. Physical Parameters Used in the Simulations

Symbol	Parameter	Value	Unit
T_s	Nyquist sampling interval	0.5	ps
T_p	Pulse width	10	ps
T_f	Frame length	1	ns
N_f	Number of frames for one symbol	[1,4]	–
f_0	Frequency step	10	MHz
P_t	Transmit power	1	dBm
G_t	Transmit antenna gain	[0, 30]	dBi
G_r	Receive antenna gain	[0, 30]	dBi
P_w	Noise power	-80	dBm
f_L	Lower filter cutoff frequency	0.06	THz
f_U	Upper filter cutoff frequency	1	THz
d_T	Communication distance	[1, 20]	m

presented results are averages over 1000 realizations. Moreover, we study the influence of synchronization on the resulting received signals. Finally, we analyze the BER sensitivity as a function of the timing acquisition errors for the two algorithms. We consider the following choice of parameters in the simulations. The random initial delay τ_0 and the random misalignment between the transmitter and the receiver ψ_i in (55) follow uniform distributions over $[-T_f, T_f]$, and are multiples of $T_s = 0.5$ ps. The physical parameters that are used in the simulations unless otherwise stated are listed in Table I, which is consistent with the THz device specifications in the literature [75].

4.6.1 LSR Algorithm Performance

In the following, timing offset estimation based on the LSR algorithm developed in Sec. 4.3 is considered. After determining the filter coefficients, we can find the roots in the z-domain. Based on the results of roots finding, we obtain the timing offset. We study the RMSE as a function of the LSR factor, for different antenna gains, distances, pulse waveforms and transmission bands. As our main objective is to achieve an accurate synchronization by using a sub-Nyquist sampling rate, we investigate which LSR factors β_{LSR} can support RMSE $\leq 0.01 T_f$. The results and the observations are discussed as follows.

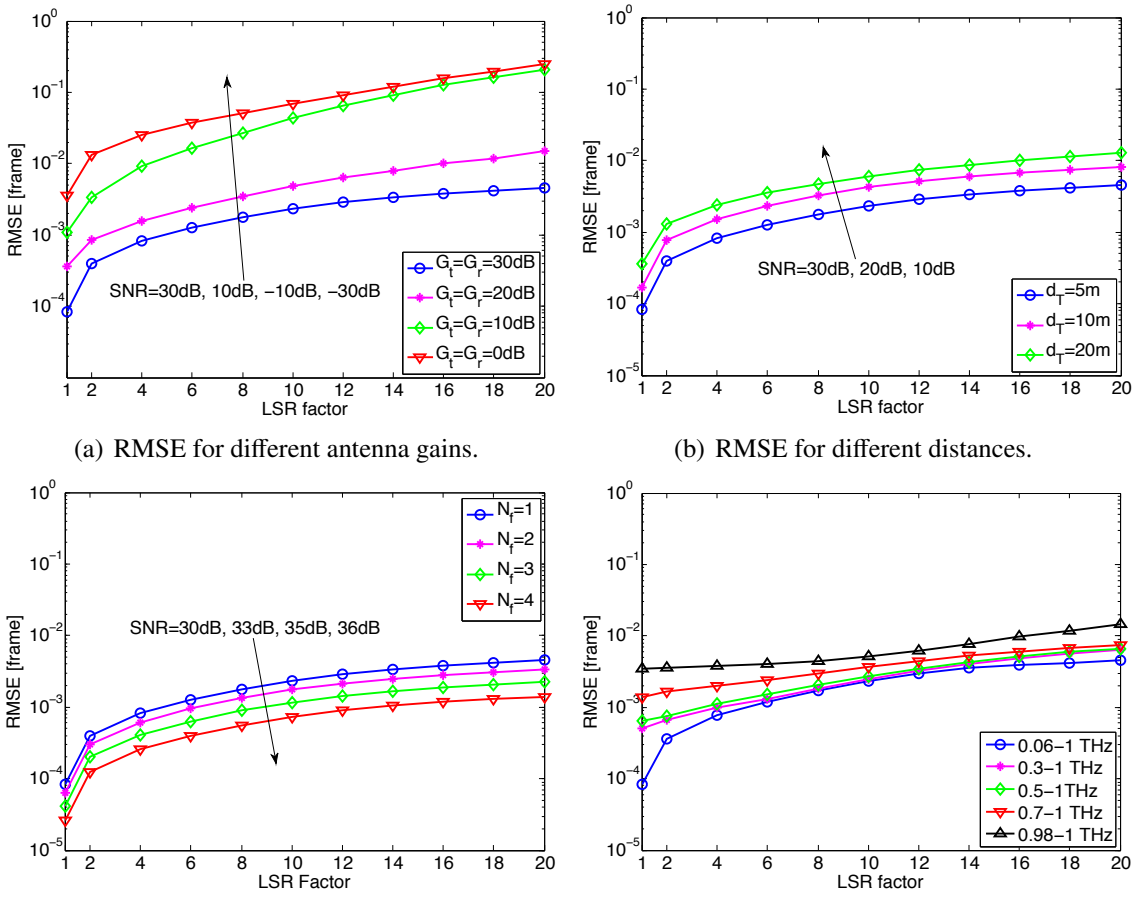

(a) RMSE for different antenna gains.

(b) RMSE for different distances.

(c) RMSE for different number of pulses per symbol, which relates to the symbol rates.

(d) RMSE for different pulse widths in the frequency domain.

Figure 22. RMSE of the LSR algorithm for different THz-band physical parameters.

4.6.1.1 Impact of Antenna Gain

In Fig. 22(a), the RMSE performance is evaluated for different antenna gains. In particular, when the antenna gains equal $G_t = G_r = 30$ dB by benefiting from the very large antenna arrays [2, 77], and the communication distance is $d_T = 5$m, $\beta_{\text{LSR}} = 20$ can be adopted. In this case, the path loss is approximately 110 dB [56] and the resulting SNR is equal to 30 dB. On the one hand, a reduction of antenna gains implies a decrease in SNR, which makes RMSE increasing significantly. As the antenna gains are equal to 20 dB, 10 dB and 0 dB, the maximum LSR factor reduces from 16 to 4 and 2. With these antenna gains, the SNR values reduce to 10 dB, -10 dB, and -30 dB. At the Nyquist sampling rate, the RMSE increases to 3×10^{-4}, 1×10^{-3} and 3×10^{-3}, respectively. These results are consistent with the analytical studies in Sec. 4.5.1 for the high SNR values, i.e, larger than 10 dB. For lower SNR values, the analytical expression in (81) over-estimates the RMSE, i.e., the analytical expressions yield larger RMSE values than the simulations. Hence, when the antenna gains or the equivalent SNR are very small, the RMSE becomes significant and the LSR algorithm is not suitable to be used.

4.6.1.2 Impact of Communication Distance

Moreover, we study the influence of communication distances on the synchronization performance in Fig. 22(b). In general, as the distance increases, a higher path loss results and more severe frequency-selectivity appears in the THz band spectrum. This consequently degrades the RMSE of the LSR algorithm. Although the LSR factor $\beta_{\text{LSR}} = 20$ can be supported to achieve RMSE = 0.01 frame, the average RMSE values increase from 0.003, 0.005, 0.007 to 0.011, as the distance increases from 5m, 10m, to 20m. At these distances, the SNR values are equal to 30 dB, 20 dB and 10 dB.

4.6.1.3 Impact of Pulse Repetitions

In addition, the influence of the number of the pulses to represent one symbol (N_f) in the transmitted signal is studied in Fig. 22(c). The increase of the number of pulses per symbol N_f leads to the improvement of the SNR of $10 \log_{10}(N_f)$ dB, which results in a reduced

RMSE. For all N_f, the LSR factor of 20 can be supported for d = 5m and $G_t = G_r$ = 30 dB. The possibility of an increase of the number of frames is important when a targeted SNR is mandatory while the antenna gains and the transmit power are fixed, as shown in (87). Moreover, the BER decreases for a larger number of pulses per symbol as suggested in Sec. 4.5.2. However, this is at the cost of the reduction of the data rate by a factor of N_f.

4.6.1.4 Impact of Pulse Width

Furthermore, the effect of five pulses with different supporting bandwidths is investigated in Fig. 22(d). With a very small pulse duration, T_p, the supporting bandwidth is large. When using the LSR algorithm in the frequency domain, a wider frequency response yields better performance. This can be explained by the fact that for the larger frequency support, the number of frequency samples is higher under the same sampling rate. However, the resulting number of samples is still high for the frequency-wide pulse, although the LSR factor can be large. In particular, a 10 ps pulse has the frequency response occupying the spectrum between 0.06 and 1 THz. This pulse waveform is able to support an RMSE of 0.01 frame with the LSR factor of 20. In contrast, the tolerable LSR factor decreases as the pulse width in the frequency domain decreases. When a 20 GHz-bandwidth pulse is used, the largest LSR factor to satisfy the RMSE constraint reduces to 16.

4.6.1.5 Discussions

In general, the performance of the LSR algorithm improves for a better SNR. The resulting RMSE decreases for a higher antenna gain, a smaller communication distance, a higher number of pulses to represent one symbol, and a larger pulse width in the frequency domain. Specifically, an LSR factor of 20 can be used to fulfill RMSE$\leq$0.01 T_f, when the antenna gains are selected as $G_t = G_r$ = 30 dB, the communication distance is d_T = 5m, the number of pulses is N_f = 1, and the pulse occupies the frequencies 0.06 - 1 THz. The resulting SNR= 30 dB. In comparison with the analytical study of the error performance in Sec. 4.5.1, a good approximation is provided in (81) for high SNR, while the approximation over-estimates the RMSE for low SNR regions.

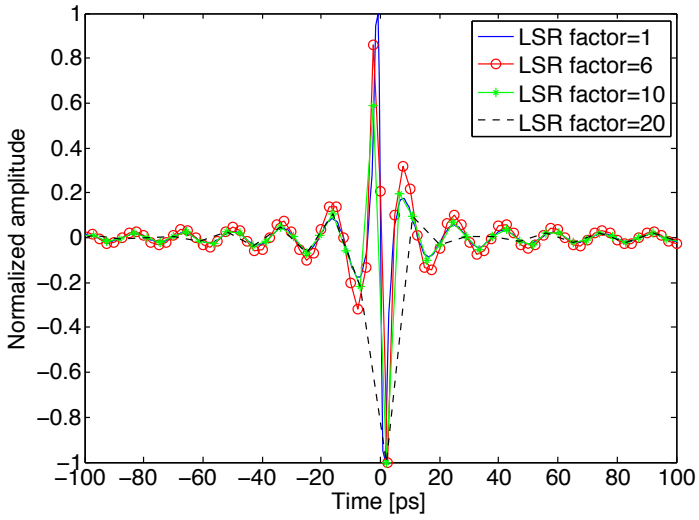

Figure 23. Sampled signals for different LSR factors.

4.6.2 Influence on Received Signal

We analyze the effect of the LSR algorithm on the received signal for different LSR factors in Fig. 23, with $N_f = 1$. With smaller sampling rates, the recovery of the received signal becomes more challenging. The RMSE values between the received pulse with $\beta_{\text{LSR}} = 1$ and the received pulses at sub-Nyquist sampling rates are evaluated in the time domain, which increases from 1.26×10^{-3}, 2.33×10^{-3} to 4.50×10^{-3}, when $\beta_{\text{LSR}} = 6, 10$ and 20. Although the recovery of received signals becomes challenging, the transmitted symbols can still be detected based on the signal power available for pulse-based communication in the THz band. The received pulses experience severe distortion in the THz band channel.

In addition to the amplitude and phase distortion, temporal broadening effects appear, due to the very high frequency-selectivity in the wideband THz spectrum [28]. The width of the received pulse independent of β_{LSR} is over 200 ps, which is 20 times larger than the transmitted pulse. However, by using a low sampling rate, the rapid fluctuation in the received pulses dwindles, and hence, the broadening effects attenuate. For example, when the LSR factors are 10 and 20, the width of the received pulse reduces to 180 ps and 150 ps, respectively. These are equivalent to suggest the maximal pulse rates of 5.56 and 6.67 Giga-pulses-per-second to avoid the inter-symbol-interference. The details on

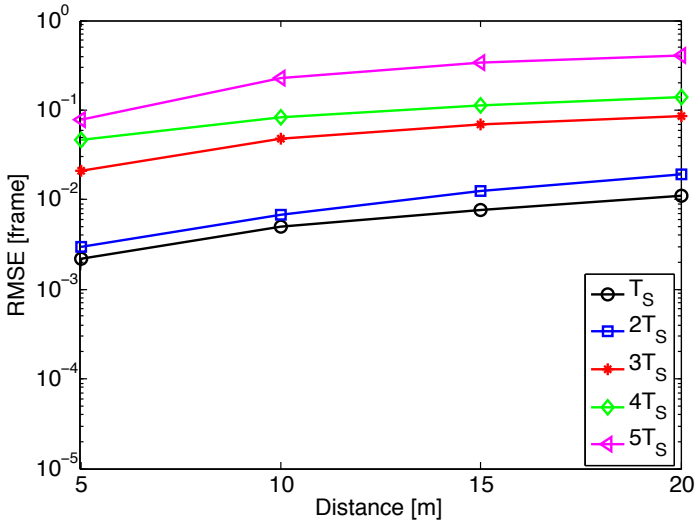

Figure 24. RMSE of the ML algorithm for different time steps, with $G_t = G_r = 0$ dB.

the temporal broadening effect and its influences on received pulses can be found in [28]. Hence, the LSR algorithm can effectively relax the restriction of the minimum spacing between consecutive pulse transmissions.

4.6.3 ML Approach Performance

The LSR algorithm is not favored when the SNR at the receiver is low, for example in the multi-path propagation [28], or with $G_t = G_r = 0$ dB. As an alternative, the ML approach yields better performance than the LSR algorithm, at the cost of significant search space and data storage. The RMSE performance of the ML-based approach is shown in Fig. 24. These results match with the observations in Sec. 4.5.1. As a major computational constraint, different time step values (multiples of the Nyquist sampling interval T_s) of the trial values in (78) are studied. The RMSE increases when the distance increases and the search space decreases. To achieve RMSE = 0.01 frame, a time step of 2 can be used to reduce the search space by half. However, the distance needs to remain below 15m. Specifically at d_T = 5m, the RMSE increases from 0.002, 0.003, 0.021, 0.046 to 0.077 when the time step increases from 1 to 5, respectively. For d_T = 5m, the SNR is equal to -30 dB, and CRLB=1.9×10^{-3} (see Fig. 21), which lower-bounds the RMSE of the ML method. Hence, the ML-based algorithm can be used when the SNR is low, with a time step of 2 to reduce

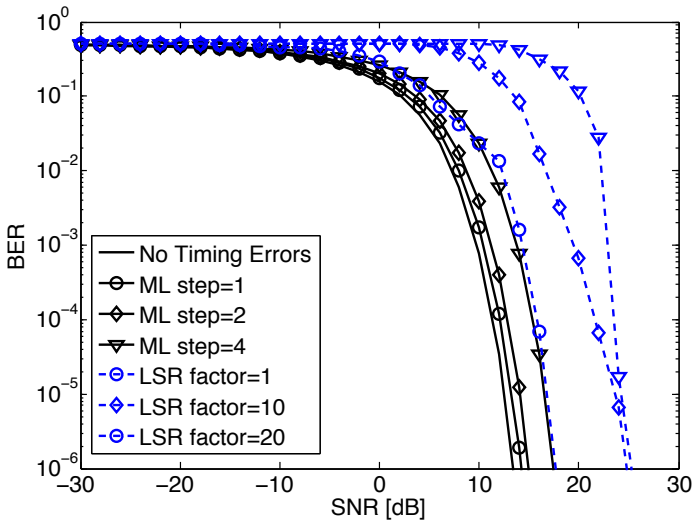

Figure 25. BER sensitivity for the LSR and ML algorithms.

the search space by half.

4.6.4 BER Sensitivity

The BER sensitivity is given in (83), where μ_i is of the order of the frame length, T_f, while ν_i is of the order of the sampling interval, T_s, as defined in (55). The BER sensitivity is presented in Fig. 25 for the different timing acquisition methods and settings. The curve corresponding to the ideal timing acquisition in (85) provides a benchmark to quantify the performance loss due to timing acquisition errors. A Gaussian pulse is considered in the simulation, which is commonly studied for THz band communications [65], with the pulse duration $T_p = 10$ ps. The results appear to be consistent with the aforementioned RMSE performance of the algorithms. Indeed, like the RMSE, the BER performance degrades as the ML step size increases and as the LSR factor increases. Moreover, the LSR algorithm shows a larger performance loss compared to the ML method, particularly at low SNR. Hence, the LSR algorithm is recommended for directional transmission while the ML method is suitable at low SNR.

4.7 Conclusions

In this chapter, we proposed and analyzed the LSR and the ML-based algorithms for timing acquisition in the THz band to address the challenges such as the THz band channel peculiarities and the ultra-high sampling rate demand. The error performance of the algorithms has been analytically approximated, where the results have shown good agreements with the simulation results when the SNR is high. Moreover, we analytically and numerically evaluated the two timing acquisition algorithms, in comparison with the CRLB. Furthermore, we studied the BER sensitivity to the acquisition errors in the two algorithms. With the metric of the RMSE, the simulation results showed that when the SNR is high (i.e., greater than 30 dB benefiting from high gain antennas), the LSR algorithm can be used with the uniform sampling at $1/20$ of the Nyquist rate, while the ML-based algorithm can be used for low SNR with a time step of 2 to reduce the search space by half. The LSR algorithm can also effectively mitigate the temporal broadening effect due to the frequency-selectivity of the THz channel. This work contributes to achieving a reliable timing acquisition with a reduced sampling rate for digital transmissions in the THz band.

CHAPTER 5

DISTANCE-AWARE BANDWIDTH-ADAPTIVE RESOURCE ALLOCATION

In this chapter, a distance-aware bandwidth-adaptive resource allocation scheme is developed in the THz band communication network, with the objectives to improve the communication distance. The proposed resource allocation scheme captures the unique channel peculiarities including the relationship between the distance and the bandwidth, and strategically utilizes the spectrum to enable multiple ultra-high-speed links. Based on the developed scheme, the sub-windows of the THz spectrum, the modulations and the transmit power are adaptively allocated, for both single-user and multi-user communications.

In the formulated optimization frameworks for the single-user and multi-user cases, the objective focuses on the distance maximization, and the constraints cover the transmit power, the bandwidth, the error rate and the data rate, which are all closely related to the physical parameters such as the path loss, the delay and the coherence bandwidth that result from the unique THz band channel as analyzed. Then, an optimal solution based on the KKT method is analytically derived for the single-user case, while a sub-optimal solution based on our proposed strategic spectrum allocation principle is provided for the multi-user case. The developed resource allocation scheme and the strategic spectrum allocation principle are numerically evaluated to effectively improve the spectrum utilization and enable multiple ultra-high-speed links in the THz band networks.

5.1 Motivation and Related Work

For the realization of ultra-high-speed wireless communication networks in the THz band, it is imperative to develop a novel communication scheme that can address the unique challenges and requirements. The development of a resource allocation scheme appears to be attractive, which have been well investigated for the multi-user multi-carrier systems

at lower frequencies [90, 91, 92, 93, 94]. However, none of these existing work fully addresses the THz challenges. Recently, ultra-high-speed communication schemes in the THz band have been studied. For example, a single-band pulse-based scheme has been proposed in [65]. However, this modulation is mainly valid for very short transmission distances, e.g., nanonetworks, in which the distance-varying spectral windows do not appear. Moreover, a multi-wideband waveform design is proposed in [79], in which an optimization framework is formulated to solve for the transmit power and the number of frames, with the aim to maximize the distance. Nevertheless, these two schemes rely on pulse-based communications and do not support more spectrum-efficient modulations, which poses a limitation on the maximum achievable data rates. Furthermore, experimental studies in [95, 96, 97] have shown the feasibility of broadband communications by exploiting the low THz frequencies (i.e., around 0.3 THz), to enable 100 Gbps wireless links below 20 m. However, the resources including the ultra-broad bandwidth, the modulation scheme and the transmit power are not jointly intelligently utilized, by being aware of the distance-bandwidth dependency in the THz band.

Therefore, we develop a distance-aware bandwidth-adaptive resource allocation scheme in THz band communication networks. In particular, this scheme determines the bandwidth as a function of the distance, and has three functionalities: sub-window allocation, modulation adaptation and transmit power controlling. These interrelated functionalities of resource allocation are realized in the control unit. A system model that employs this resource allocation scheme is illustrated in Fig. 26.

Design guidelines: Based on the channel characteristics according to Chapter 2, the very strong relationship between the distance, the spectral windows and the total usable bandwidth motivates the development of *distance-aware bandwidth-adaptive* transmission schemes. Moreover, the ultra-broad bandwidth of the spectral window ranges from multi-GHz to THz, which allows the multi-band transmission by dividing each spectral window

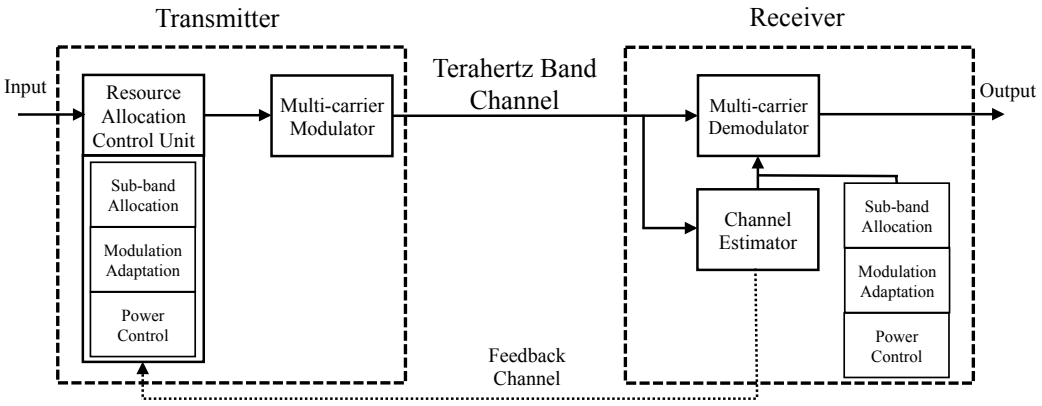

Figure 26. The system model of the the distance-aware bandwidth-adaptive resource allocation scheme, by using the control unit.

into many sub-windows. The utilization of the sub-windows needs to be intelligently selected to avoid spectrum with the path loss peaks. For example, in the multi-path propagation with d = 5m, the spectrum above 0.1 THz has significantly large path loss and cannot be used. In the directional propagation, the communication around 0.56 THz, 0.75 THz, and 0.98 THz need to be prevented.

As a result, the created sub-window has smaller bandwidth and supports slower data rates, which effectively relaxes the design requirements of individual sub-windows, and is helpful for THz band communication to process very high data rates. Over each band, adaptive modulation can be used for transmission for the features of spectral-efficiency and in conjunction with the design of transmit power and error rate. These resource allocation techniques have been well explored for lower frequencies in [90, 91, 92, 93]. In the realm of THz band communications, the distance improvement becomes the focus and moreover, the available bandwidth varies over the different distances. Furthermore, the peculiarities of the channel lead us to rethink the physical parameters in the resource allocation scheme, as follows.

From the investigation on the temporal broadening effects, the width of the sub-width can be set as B_g = 1 GHz, which is smaller than the coherence bandwidth. The separation between the consecutive transmissions is larger than the minimum separation that is defined

by the temporal broadening effects in the THz band channel. This eliminates the ISI effects and thereby, allows the narrowband communication over each sub-window. However, in this multi-band system, the IBI occurs which causes from the power leakage from the neighboring sub-windows. Hence, the sub-window width (B_g), the utilization and the allocation of the spectrum, the IBI, the transmit power, and the modulation schemes, and the distance enhancement, need to be throughout investigated in the THz band communication network.

For each sub-band or sub-window, we consider that a single carrier is implemented in an individual modulator/demodulator circuit at the transmitter/receiver. The overall multi-band modulators/demodulators are included in the system design in Fig. 26. Then, the signal over each sub-band is radiated by using an individual THz antenna with a directivity gain. Thanks to the very small wavelengths at THz frequencies, the multi-band architecture can be implemented by using the graphene-based nano-antenna [27, 45] and nano-transceiver [20, 98] technologies, among others. Although orthogonal frequency-division multiplexing (OFDM) is suggested for 60 GHz systems to enhance the spectral efficiency [66], the bandwidth is not scarce in the THz band. Furthermore, the very complex transceivers, high peak-to-average power ratio (PAPR), and strict requirements for frequency synchronization make OFDM very challenging in the THz band, where digital processors that can handle such very high data rates (e.g., over 1 Tbps) do not exist to date. On the contrary, the multi-band system allows non-overlapping utilization of the spectrum to improve the spectrum efficiency compared to the pulse-based systems [65, 79], while has less complex transceivers and more relaxed synchronization requirements than OFDM systems.

5.2 Distance-aware Bandwidth-adaptive Resource Allocation: Single-user

In this section, we develop the distance-aware bandwidth-adaptive resource allocation scheme in the single-user communication. The objective is to increase the communication range and explore the relationship between the distance and the bandwidth. This can be realized by maximizing the data rate, since it decreases monotonically as the distance rises. In this case, the available spectrum is determined as a function of the link distance and the entire bandwidth is allocated to one user. Then, once the data rate requirement is determined, the largest attainable distance is obtained accordingly.

5.2.1 Signal-to-Interference-plus-Noise Ratio (SINR)

For a communication distance d, we consider that there are $U(d)$ sub-windows or sub-bands for transmission. We first determine the expression for the SINR, which is affected by the transmit power, the channel gain, the interference and the noise. In particular, the interference associated with the multi-band system includes the ISI and the IBI. ISI is negligible as discussed in the design guidelines, which is enabled by the narrowband communication over each sub-window. Hence, the IBI is analyzed first.

The IBI occurs in the multi-wideband systems which causes from the power leakage from the neighboring sub-windows. In the THz band, the number of sub-windows is at the order of multiple-tens. To model this interference, we invoke the central limit theorem to approximate the IBI with a Gaussian process. The IBI accounts for the power leakage from the surrounding sub-windows. The distribution of the interference power on the u^{th} sub-window that superimposes from the other sub-windows has the expression

$$I_B^u \sim \mathcal{N}\left(0, \int_{f_u} \sum_{v, v\neq u}^{U(d)} P_v |G^v(f_u)| \sum_{m=1}^{N_u} \boldsymbol{\alpha}^{(v)}(m)|^2 df_u\right), \tag{86}$$

where G^v describes the waveform. The interference on the u^{th} sub-window is contributed as the power leakage from the v^{th} sub-window, with $v \neq u$. Moreover, from the channel model in (2), the path attenuation $\boldsymbol{\alpha}^{(v)} = [\alpha_{\text{LOS}}^{(v)}, \alpha_{\text{Ref}}^{(v,1)}, \ldots, \alpha_{\text{Ref}}^{(v,N_{\text{Ref}}^{(v)})}]$.

The IBI captures the power leakage from the surrounding sub-windows, and increases if the separation between the consecutive sub-windows (i.e., the bandwidth of the sub-window that is denoted by B_g) decreases. As the distance increases, the frequency selectivity becomes more severe. Consequently, the temporal broadening makes the transmitted pulse in the time domain wider, which thereby leads to a reduction of the IBI in the frequency domain. With the use of high-gain antennas, the delay spread reduces significantly and the channel frequency response varies less frequency-selective. However, the path loss of the channel is reduced and hence, the IBI becomes more significant in this case. These effects are captured in (86).

Next, the instantaneous SINR in the u^{th} sub-window, $\gamma_u(d)$, is analyzed, which is affected by the channel response, the transmit power, the interference and the noise, as

$$\gamma_u(d) = \frac{G_t G_r |h_u(d)|^2 P_{\text{Tx}}}{G_t G_r I_B^u + B_g S_w}, \tag{87}$$

where h_u is the channel response in the u^{th} sub-window given in (2), P_{Tx} represents transmit power, S_w denotes the noise power spectral density, and I_B^u is the interference from (86). As a function of the instantaneous SINR in (87), the received SNR in this sub-window equals to $\gamma_u \left(P_u(\gamma)/P_{\text{Tx}}\right)$, with P_u standing for the transmit power that is allocated on the u^{th} sub-window.

5.2.2 Resource Allocation Model

In the single-user communication, the very broad bandwidth in the THz band enables very high data rate transmission. Hence, different from the traditional resource allocation problem which either minimizes the energy consumption or maximizes the data rate, distance maximization becomes the objective, while the data rate needs to exceed some threshold.

In order to address this distance maximization problem efficiently, we transform it into a set of data rate maximization problems for different distances. Then, the solution to the original distance maximization problem is found at d^*, when the transformed optimal data rate drops to the threshold, $R_{\text{su}}^{\text{th}}$, at the distance d^*. Since the resource allocation problem for

data rate maximization is well investigated and the optimal solution requires low complexity, the distance maximization in the realm of the THz band communication can be solved efficiently.

To start with, the original distance maximization problem is written as

$$\textit{Objective:} \quad \max \quad d \tag{88}$$

$$\textit{Subject to:} \quad R_{\mathrm{su}}(d) > R_{\mathrm{su}}^{\mathrm{th}} \tag{89}$$

To transform this into the data rate maximization, we first express the single-user data rate at one particular distance as the sum of the data rates on individual sub-windows, as

$$\textit{Transformed objective:} \quad \max_{P_u, k_u} \quad R_{\mathrm{su}}(d) = B_g \sum_{u=1}^{U(d)} k_u(\gamma_u(d)), \tag{90}$$

The solution to the distance maximization problem is found by iteratively solving (90) with the increasing d to satisfy (89).

Note that the SINR is a function of the distance and the transmit power P_u depends on the SINR. For conciseness, these dependencies are declared when the parameters are defined, whereas the dependences are omitted in the later equations. Moreover, ϵ_u refers to the bit error rate (BER) on the u^{th} sub-window, which is a function of the SINR as well. In particular, the BER expression of square MQAM as a function of SINR is approximated as [94]

$$\begin{aligned}\epsilon_u(\gamma_u(d)) &\approx \frac{2}{k_u}\left(1 - \frac{1}{\sqrt{2^{k_u}}}\right) \times \mathrm{erfc}\left(\frac{1.5\gamma_u\,(P_u/P_{\mathrm{Tx}})}{2^{k_u}-1}\right) \\ &\approx 0.2\exp\left(\frac{-1.5\gamma_u\,(P_u/P_{\mathrm{Tx}})}{2^{k_u}-1}\right).\end{aligned} \tag{91}$$

In (90), the rate on the sub-window, k_u, is obtained as a log function of the maximum constellation

$$k_u(\gamma_u(d)) = \log_2\left(1 - \frac{1.5\gamma_u\,(P_u/P_{\mathrm{Tx}})}{\ln(5\epsilon_u)}\right). \tag{92}$$

There are two constraints associated with the single-user optimization problem. First, the total transmit power for each user is bounded by:

$$\textit{Constraint 1:} \quad \sum_{u=1}^{U(d)} P_u(\gamma_u(d)) \leq P_{\mathrm{Tx}}, \tag{93}$$

where P_{Tx} is the threshold of the transmit power budget. The second constraint is for the error rate, which is equivalent to the constraint on the SINR per bit in the communication system. Specifically, the average BER, $\overline{\epsilon}$, as

$$\textit{Constraint 2:} \quad \overline{\epsilon} = \frac{B_g \sum_{u=1}^{U(d)} \epsilon_u \cdot k_u}{B_g \sum_{u=1}^{U(d)} k_u} \leq \epsilon_{\mathrm{th}}, \tag{94}$$

where ϵ_{th} refers to the average BER threshold value, and the BER is derived in (91), which is related to the SINR, the distance, the modulation scheme and the transmit power.

5.2.3 Solution

This constrained optimization problem can be solved by using the KKT method, with the convex objective of maximizing the data rate [72]. By defining the KKT multipliers, $\mu_1, \mu_2 \geq 0$, we obtain the Lagrangian as

$$L(P_u, k_u, \mu_1, \mu_2) = \sum_{u=1}^{U(d)} k_u + \mu_1 \left[P_{\mathrm{Tx}} - \sum_{u=1}^{U(d)} P_u \right] + \mu_2 \left[\epsilon_{\mathrm{th}} B_g \sum_{u=1}^{U(d)} k_u - B_g \sum_{u=1}^{U(d)} \epsilon_u \cdot k_u \right]. \tag{95}$$

By differentiating the Lagrangian with respect to the power adaptation and transmutation rate, we can obtain the KKT necessary conditions for the optimal solutions [99], as

$$\frac{\partial L}{\partial P_u} = 0, \quad \text{and} \tag{96}$$

$$\frac{\partial L}{\partial k_u} = 0. \tag{97}$$

The above condition in (96) can be rearranged since k_u is not a function of P_u, as

$$-\mu_1 - \mu_2 \cdot B_g k_u \frac{\partial \epsilon_u}{\partial P_u} = 0 \tag{98}$$

By recalling (91), the derivative of the error probability can be rearranged as

$$\begin{aligned} \frac{\partial \epsilon_u}{\partial P_u} &= \frac{\partial \left[0.2 \exp\left(\frac{-1.5\gamma_u(P_u/P_{\mathrm{Tx}})}{2^{k_u}-1} \right) \right]}{\partial P_u} \\ &= -\frac{1.5\gamma_u / P_{\mathrm{Tx}}}{2^{k_u}-1} \cdot \epsilon_u \end{aligned} \tag{99}$$

By combining (98) and (99), the BER adaptation is obtained as

$$\epsilon_u = \frac{P_{\mathrm{Tx}}\mu_1}{\mu_2 B_g k_u} \cdot \frac{2^{k_u}-1}{1.5\gamma_u} \tag{100}$$

This can be interpreted that the error probability decreases as the channel quality (i.e., the SINR in (100)) increases, which is matching with the water-filling principle. From (97), we obtain

$$1 + \mu_2 \epsilon_{\mathrm{th}} B_g - \mu_2 \frac{\partial \epsilon_u}{\partial k_u} \cdot B_g k_u - \mu_2 \epsilon_u B_g = 0 \tag{101}$$

By recalling (91), the derivative of the error probability can be rearranged as

$$\begin{aligned}\frac{\partial \epsilon_u}{\partial k_u} &= 0.2 \exp\left(\frac{-1.5\gamma_u (P_u/P_{\mathrm{Tx}})}{2^{k_u}-1}\right) \cdot \frac{1.5\gamma_u (P_u/P_{\mathrm{Tx}})}{(2^{k_u}-1)^2} \cdot 2^{k_u} \ln(2) \\ &= \epsilon_u \cdot \frac{1.5\gamma_u (P_u/P_{\mathrm{Tx}})}{(2^{k_u}-1)^2} \cdot 2^{k_u} \ln(2). \end{aligned} \tag{102}$$

Then, to combine (100), (101) and (102), the power adaptation that maximizes the data rate is

$$\begin{aligned}\frac{P_u}{P_{\mathrm{Tx}}} &= \max\left\{\left[\frac{1+\mu_2\epsilon_{\mathrm{th}}B_g}{\mu_2\epsilon_u B_g} - 1\right] \cdot \frac{\left(2^{k_u}-1\right)^2}{1.04 \cdot \gamma_u 2^{k_u} k_u}, 0\right\} \\ &= \max\left\{\frac{\left(2^{k_u}-1\right)\left(1+\mu_2\epsilon_{\mathrm{th}}B_g\right)U(d)}{P_{\mathrm{Tx}}\mu_1 2^{k_u}\ln(2)} - \frac{\left(2^{k_u}-1\right)^2}{1.04 \cdot \gamma_u 2^{k_u} k_u}, 0\right\}. \end{aligned} \tag{103}$$

By including (87), the solution to the power adaptation is

$$\frac{P_u}{P_{\mathrm{Tx}}} = \max\left\{\frac{\left(2^{k_u}-1\right)\left(1+\mu_2\epsilon_{\mathrm{th}}B_g\right)}{P_{\mathrm{Tx}}\mu_1 2^{k_u}\ln(2)} - \frac{\left(2^{k_u}-1\right)^2 (G_t G_r I_B^u + B_g S_w)}{1.04 \cdot G_t G_r |h_u(d)|^2 P_{\mathrm{Tx}} 2^{k_u} k_u}, 0\right\}. \tag{104}$$

The constellation adaptation k_u that is defined in (92) is either zero or the non-negative solution of the following equation, by recalling (92), (100) and (104):

$$\frac{1+\mu_2\epsilon_{\mathrm{th}}B_g}{P_{\mathrm{Tx}}\mu_1 2^{k_u}\ln(2)} - \frac{(2^{k_u}-1)(G_t G_r I_B^u + B_g S_w)}{1.04 G_t G_r |h_u(d)|^2 P_{\mathrm{Tx}} 2^{k_u} k_u} = -\frac{1}{1.5\gamma_u}\ln\left(\frac{P_{\mathrm{Tx}}\mu_1}{\mu_2 B_g k_u} \cdot \frac{(2^{k_u}-1)(I_B^u + B_g S_w)}{0.3 G_t G_r |h_u(d)|^2 P_{\mathrm{Tx}}}\right). \tag{105}$$

The values of the modulation rate k_u and the Lagrange multipliers μ_1 and μ_2 can be found through a numerical search, which guarantees that the transmit power and the BER constraints are satisfied.

In practice, the transmission rate is discrete and varied within a fixed set [94]. For example, if we select no transmission, BPSK, 4-QAM, 16-QAM, 64-QAM, 256-QAM and 1024-QAM as the MQAM candidates, the rate $k_{u,v}$ takes the value in the set $\{0, 1, 2, 4, 6, 8, 10\}$ bits/symbol. Correspondingly, there are six boundary SINR values, namely $\{\hat{\gamma}_m, m = 1, 2, 3, 4, 5, 6\}$, which are used to assign the transmission rate, $\{\hat{k}_m\}$. In particular, the rate on each sub-window is determined by using the following piecewise function

$$k_u = \begin{cases} 0 & \text{if } \gamma_u < \hat{\gamma}_1 \\ 1 & \text{if } \hat{\gamma}_1 \leq \gamma_u < \hat{\gamma}_2 \\ 2 & \text{if } \hat{\gamma}_2 \leq \gamma_u < \hat{\gamma}_3 \\ 4 & \text{if } \hat{\gamma}_3 \leq \gamma_u < \hat{\gamma}_4 \\ 6 & \text{if } \hat{\gamma}_4 \leq \gamma_u < \hat{\gamma}_5 \\ 8 & \text{if } \hat{\gamma}_5 \leq \gamma_u < \hat{\gamma}_6 \\ 10 & \text{if } \hat{\gamma}_6 \leq \gamma_u \end{cases} \tag{106}$$

As a result, the rate adaptation corresponds to finding the rate region boundaries. If we further assume that the power adaption P_u is continuous at each boundary [94], we obtain the solutions to the optimization framework. To start with, we define two constants μ_1 and μ_2, which will be updated at each iteration. At the first step, the SINR boundaries are defined, which are used to determine the transmission rate on each sub-window, as obtained at the second step. Then, the BER and transmit power allocation are computed at the third and fourth steps. To end this iteration, we decrease μ_1 and increase μ_2. In the next iteration, we check the current transmit power and the average BER. If both of these two constraints are satisfied, we proceed to the first step and repeat the process. Otherwise, we acquire the desired values for P_u, k_u and the iteration is completed.

By using the aforementioned solution, the analytical solution to maximizing the rate for a distance in (90) can be acquired efficiently. Then, the solution to the original distance maximization problem in (88) is found at d^*, when the optimal data rate $R_{\text{su}}(d^*)$ drops to $R_{\text{su}}^{\text{th}}$ as in (89). Since the resource allocation problem for the data rate maximization has

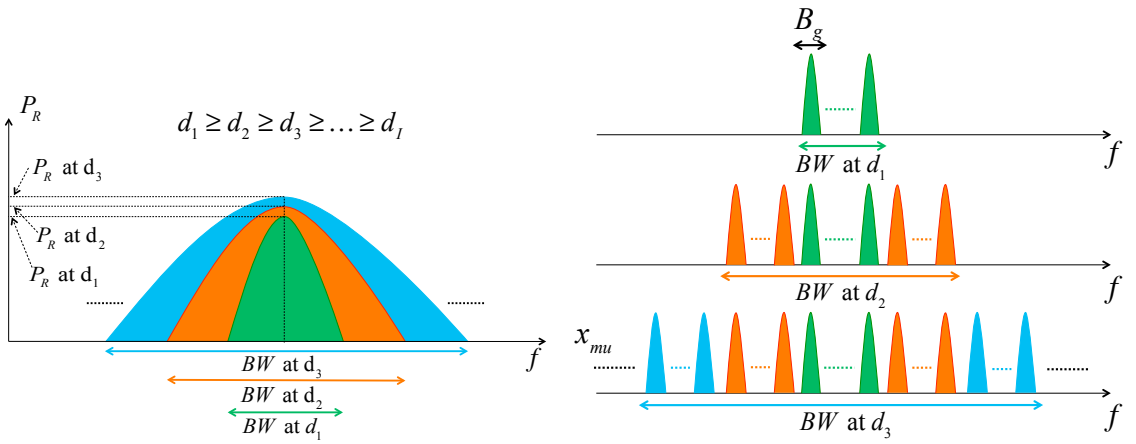

(a) Receive power and bandwidth (BW).

(b) An illustration of the proposed spectrum allocation principle.

Figure 27. Multi-user communication network.

analytical solution with a low complexity, the original resource allocation problem for the distance maximization in the THz band can be solved efficiently.

5.3 Distance-aware Bandwidth-adaptive Resource Allocation: Multi-user

In the single-user case, the communication range and the data rate are maximized by intelligently adapting the transmit power and the modulation technique on each sub-window. For example, the data rate over 100 Gbps (as studied in [61] and in Sec. 5.4.1) is attainable for distance up to 21m, by applying the distance-aware bandwidth-adaptive resource allocation scheme in the directional transmission. However, the actual utilized bandwidth to enable this ultra-high-speed link is 0.06-0.12 THz or equivalently, 60 sub-windows. Being motivated by this spectrum under-exploitation, our aim is to seek for the bound on how many ultra-high-speed links can be simultaneously supported in the THz band. To achieve this goal, in this section we propose a novel strategic spectrum allocation principle adjunct with the distance-aware bandwidth-adaptive resource allocation scheme in the multi-user case.

5.3.1 Strategic Spectrum Allocation

In a multi-user network, there are I transmission links to be allocated. We sort the links in a descending order according to the distance, such as $d_1 > \ldots > d_i > \ldots > d_I$. Without loss of generality, we analyze one spectral window in the THz band, as shown in Fig. 27(a). As the distance decreases, the path loss drops and as a result, the received power (P_R) and the usable bandwidth (BW) of this window increase, for example, from d_1 to d_2 and d_3. Based on this relationship, the strategic spectrum utilization principle is presented in Fig. 27(b), and summarized as follows. First, the center sub-windows, i.e. the center spectrum in the window, are allocated to the long-distance links. Then, the side sub-windows, i.e., the side spectrum in the window, are allocated to the short-distance transmissions.

Based on this principle, on the one hand, the information on the side sub-windows cannot reach the long-distance users due to the very high path loss. On the other hand, the information on the central sub-windows can reach not only the intended long-distance users, but also the unintended short-distance users, which causes interference. However, this interference to the short-distance users can be effectively mitigated in the multi-carrier communication scheme [70]. As a consequence, this strategic principle efficiently utilizes the spectrum and benefits from the unique relationship between the bandwidth and the distance in the THz band. Note that the distance difference between the consecutive links, for example $d_i - d_{i+1}$, needs to be sufficiently large, so that there is enough bandwidth to be further exploited to support $R_{\text{mu}}^{i+1}(d_{i+1}) \geq R_{\text{mu}}^{\text{th}}$, where $R_{\text{th}}^{\text{mu}}$ represents the data rate threshold in the multi-user network.

5.3.2 Resource Allocation Model

By incorporating this spectrum allocation principle, we formulate the resource allocation model. In a THz band communication network, there is an existing link over the distance d_1. The data rate of this link satisfies the requirement of the ultra-high-speed transmission, $R_{\text{mu}}^{\text{th}}$, i.e., $R_{\text{mu}}^{1}(d_1) \geq R_{\text{mu}}^{\text{th}}$. On the one hand, we focus on addressing the distance challenge in the THz band communication. On the other hand, the resource allocation model in

the multi-user network needs to support multiple ultra-high-speed links at the same time. Therefore, the objective of our strategic spectrum allocation principle is to maximize the total distance, $\sum_{i=1}^{I} d_i$, where I represents the number of transmission links reaching the ultra-high-speed threshold. Then, the data rate becomes a constraint that needs to exceed a threshold (i.e., 10 Gbps or 100 Gbps), thanks to the very broad bandwidth in the THz band. This is different from the multi-user resource allocation schemes for the lower microwave frequencies, in which the data rate or the power consumption is the challenge. For the microwave frequencies, the objective in the resource allocation schemes is either maximizing the total data rate or minimizing the total power consumption [100].

The variables associated in this scheme nclude the transmit power, the modulation scheme and the sub-window allocation. We describe the resource allocation model as

$$\max_{P_u^i, k_u^i, \rho_u^i} \quad \sum_{i=1}^{I} d_i \tag{107}$$

$$\text{subject to} \quad \sum_{u=1}^{U(d)} P_u^i \cdot \rho_u^i \le P_{\text{Tx}}, \text{ for all } i \in \{1, \ldots, I\}, \tag{108}$$

$$\frac{B_g \sum_{u=1}^{U(d)} \epsilon_u^i k_u^i \rho_u^i}{B_g \sum_{u=1}^{U(d)} k_u^i \rho_u^i} \le \epsilon_{\text{th}}, \text{ for all } i \in \{1, \ldots, I\}, \tag{109}$$

$$\sum_{i=1}^{I} \rho_u^i = 1, \text{ for all } u \in \{1, \ldots, U\}, \tag{110}$$

$$R_{\text{mu}}^i(d_i) \ge R_{\text{mu}}^{\text{th}}, \text{ for all } i \in \{1, \ldots, I\}. \tag{111}$$

In (108), the transmit power on each individual sub-window, P_u^i, needs to satisfy that the total transmit power for each user is bounded by P_{Tx}. The average BER for each user's transmission needs to satisfy the constraint in (109), in which $\epsilon_u^i(\gamma)$ refers to the BER of the i^{th} user in the u^{th} sub-window. Moreover, we define the *sharing factor*, ρ, which is dependent on the transmission rate, as

$$\rho_u^i = \begin{cases} 1 & \text{if } k_u^i > 0, \\ 0 & \text{if } k_u^i = 0. \end{cases} \tag{112}$$

The constraint in (110) implies that one sub-window is occupied by at most one user. Finally, the data rate on each link needs to exceed the threshold value for ultra-high-speed communication, as expressed in (111). The calculation of this data rate is described as

$$R^i_{\text{mu}}(d_i) = B_g \sum_{u=1}^{U(d)} k^i_u \cdot \rho^i_u. \tag{113}$$

where d_i denotes the distance of the i^{th} link. These link distances in the multi-user case are restricted as

$$d_{\min} \leq d_i \leq d_{\max}, \tag{114}$$

where $d_{\min}$ is the lower-bound distance, and $d_{\max}$ refers to the upper-bound distance.

In the multi-user case, the SINR for the i^{th} user on the u^{th} sub-window, $\gamma^i_u(d_i)$, is defined as

$$\gamma^i_u(d_i) = \frac{G_t G_r |h_u(d_i)|^2 P_{\text{Tx}}}{G_t G_r I^u_B + B_g S_w}, \tag{115}$$

where the inter-band interference is taken into account as given in (86) which includes the effect of the multi-user interference. The SINR determines the allocation of the transmit power, the rate and the sub-window utilization. In particular, if the SINR is below than the threshold $\hat{\gamma}_1$ in (106), no transmit power is allocated since no transmission occurs, which equivalently to suggest that S^i_u, k^i_u, ρ^i_u are all zeros in this sub-window.

5.3.3 Solution

In the multi-user resource allocation problem, there are totally 3I+U constraints and 3UI variables. To avoid the high complexity of solving this problem, we propose a sub-optimal solution, which efficiently allocates the transmit power, the modulation scheme and the sub-window. Numerical results in Sec. 5.4 will show that the proposed solution with the strategic spectrum allocation (in Sec. 5.3.1) can achieve better results than the existing solutions.

The flow chart to search for the solutions to (107) is demonstrated in Fig. 28, and is explained as follows. First, we sort the links in the network by distances. We initialize the

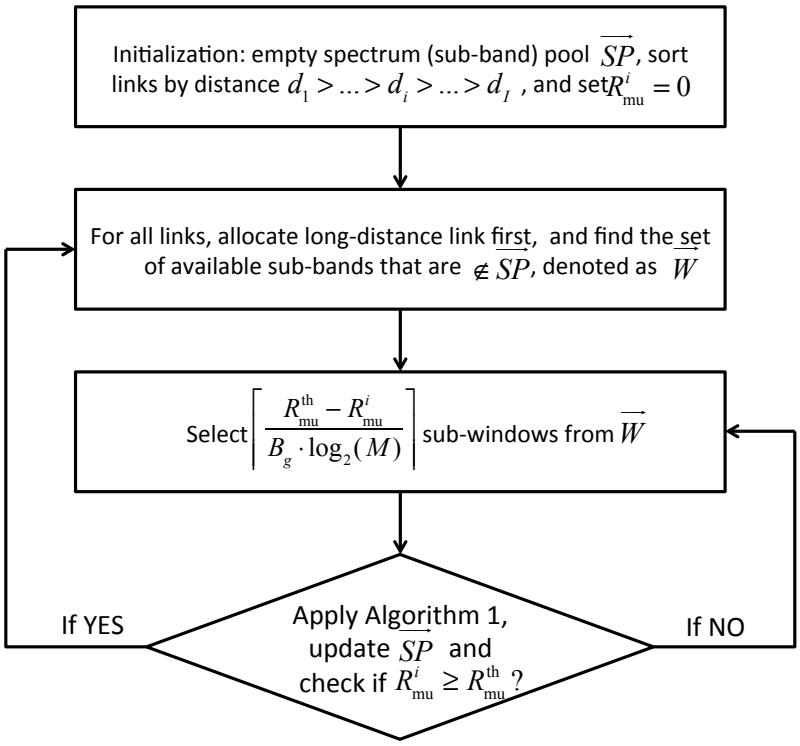

Figure 28. A flow chart for the distance-aware bandwidth-adaptive resource allocation in multi-user networks.

flow by defining a spectrum/sub-window pool $\overrightarrow{SP}$, which contains the set of sub-windows that have already been occupied. Second, starting with long-range communication, we identify the set of available sub-windows, $\overrightarrow{W}(d_i)$, which are determined based on the transmission distance and are not contained in the spectrum pool, i.e., $w \notin \overrightarrow{SP}$ for all $w \in \overrightarrow{W}(d_i)$. Third, we estimate the number of additional sub-windows that is needed for the current user to satisfy $R_i \geq R_{\text{th}}$, which is calculated as

$$\text{Number of sub-windows} \geq \left\lceil \frac{R_{\text{mu}}^{\text{th}} - R_{\text{mu}}^i}{B_g \log_2(M)} \right\rceil, \tag{116}$$

where $\lceil \cdot \rceil$ stands for the ceiling function. This can be explained that the number of sub-windows is at least equal to the ratio of the total demanding data rate and the largest rate per sub-window. Here M represents the M-QAM modulation and we obtain the number of sub-windows by choosing $\log_2(M) = 10$ for 1024-QAM, which is the lower-bound of the sub-windows that are needed, as considered in Sec. 5.2. Fourth, after completing the sub-window allocation, we perform Algorithm 1 to compute the data rate, and update

the spectrum pool based on the sharing factor information as defined in (110). Finally, we check whether the current data rate satisfies the threshold as defined in (111). If the rate constraint is satisfied, we proceed to repeat the procedures for the next-farthest link. Otherwise, we allocate more sub-windows to the current link by using the updated data rate and spectrum pool information.

After iterating these steps until all the links are completed, the solutions to the allocated transmit power, the modulation over each sub-window and the distribution of the sub-windows are obtained. However on the other hand, if spectrum resources are fully assigned, i.e., there is no w such that $w \notin \overrightarrow{SP}$ and $w \in \overrightarrow{W}(d_i)$, I links cannot be accommodated simultaneously for ultra-high-speed transmissions in the THz band.

Hence, the network data rate, $R_{\text{mu}}^{\text{Tot}}$, is equal to the sum of data rates for individual links, R_{mu}^{i}, as

$$\begin{aligned} R_{\text{mu}}^{\text{Tot}} &= \sum_{i=1}^{I} R_{\text{mu}}^{i}(d_i) \\ &= \sum_{i=1}^{I} B_g \sum_{u=1}^{U(d)} k_u^i \cdot \rho_u^i. \end{aligned} \tag{117}$$

5.3.4 Theoretical Bounds

We analyze two theoretical bounds on the data rates based on the developed resource allocation mechanisms for the single-user and multi-user cases. The multi-user data rate R_{mu}^{i} is generally different from the single-user data rate R_{su} as given in (90). For the same distance, the relation is

$$R_{\text{mu}}^{i}(d_i) \leq R_{\text{su}}(d_i), \text{ for } i = 1, 2, \ldots, I, \tag{118}$$

Proof: For the same distance, the multi-user rate is no greater than the single-user one, since the center of the spectral windows has been partially occupied by long-distance links as illustrated in Fig. 27(b). The equality holds for the first link, i.e., $R_{\text{mu}}^{1}(d_1) = R_{\text{su}}(d_1)$.

Furthermore, we have another observation on the overall data rate of the multi-user network, which suggests that R_{mu} is bounded by $R_{\text{su}}(d_1)$ and $R_{\text{su}}(d_I, I \cdot P_{\text{Tx}})$. These inequalities

are expressed as

$$R_{\text{su}}(d_1) \leq R_{\text{mu}}^{\text{Tot}} \leq R_{\text{su}}(d_I, I \cdot P_{\text{Tx}}). \tag{119}$$

Proof: Comparing to the single-user link with the distance d_1, the data rate is improved since additional bandwidth is used in the multi-user network support other links, without compromising the link 1. Simultaneous transmissions by following the proposed strategic spectrum allocation approach enhances the spectrum utilization and the network data rate effectively.

On the other hand, the total usable bandwidth is dependent on the shortest link in the network. In the single-user ($d = d_I$) and the multi-user cases, the total usable bandwidth are equal. However in the multi-user network, the centers of the spectral windows are occupied by long-distance links, which have higher path loss and consequently, worse rate performance. This results in the total multi-user data rate is less than the single-user rate, while the transmit power is calibrated as $I \cdot P_{\text{Tx}}$ for the fair comparison.

5.4 Performance Evaluation

In this section, we evaluate the performance of the distance-aware bandwidth-adaptive resource allocation scheme in both single-user and multiple-user regimes. The discrete MQAM signal constellation chooses from no transmission, BPSK, 4-QAM, 16-QAM, 64-QAM, 256-QAM, and 1024-QAM, which corresponds to the modulation rate $k_u^i \in \{0, 1, 2, 4, 6, 8, 10\}$ bits/Hz as in Sec. 5.2.3. We consider the BER requirement in (94) as $\epsilon_{\text{th}} = 10^{-3}$.

5.4.1 Single-user THz Band Communication

Solution to the Resource Allocation: We obtain the numerical solutions to the developed optimization in (90), by using Algorithm 1. The initial value for the constant μ_1 is chosen as the maximum of the SINR values over the sub-windows which guarantees the feasibility of the solution. At each iteration, it is decreased by 5 percent (i.e., multiply with 0.95). A

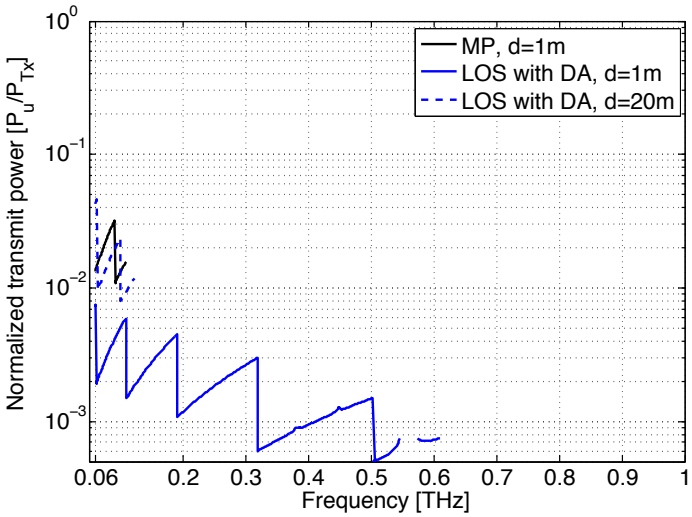

(a) Transmit power.

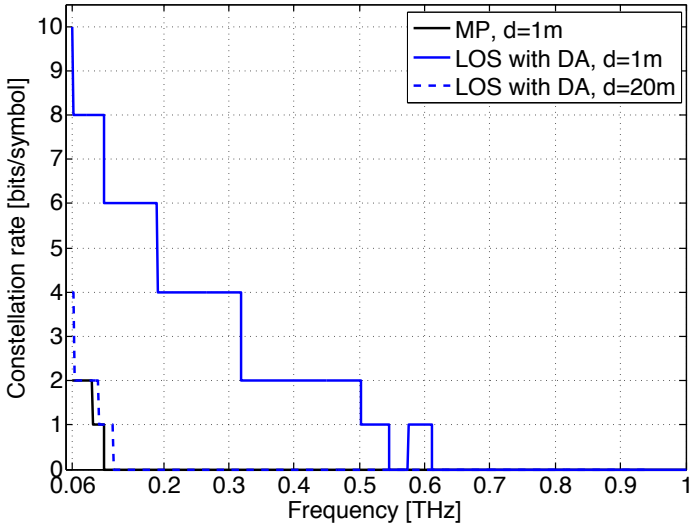

(b) Modulation rate.

Figure 29. Solution to the single-user resource allocation.

good value for the constant μ_2 is found via numerical search, and a general rule is that a smaller value is desired for a larger distance. In the resource allocation problem in (90), the transmit power and the modulation constellation are solved for the different transmission schemes over the different distances, in Fig 29(a) and 29(b) respectively.

Transmit Power: In the multi-path (MP) transmission, the normalized transmit power is shown for d = 1m. The actual utilized bandwidth is 0.06-0.11 THz. while no transmission is allowed for the higher frequencies. In the LOS with directional antenna (DA) case, the transmit power allocation has the shape of a sawtooth, which is also observed in [94]. The utilized frequency bands are less than 0.61 THz. Being consistent with the spectral window analysis, the path loss peak around 0.56 THz is avoided for transmission as shown in Fig 29(a). When the distance increases to 20m, the utilized frequency band shrinks to 0.12 THz. This can be explained that the SINR decreases as the distance or equivalently the path loss in the channel increases. In this case, the resource needs to be focused on the high SINR region, which lies in the lower THz band.

Modulation Rate: At d=1m in the MP case, 2 bits/symbol or 4-QAM is allocated for the 0.06-0.091 THz, while 1 bit/symbol or BPSK is allocated for 0.091-0.11 THz, in our resource allocation model. On the contrary, for the same distance in the LOS with directional antenna (DA) case, 10 bits/symbol is supported from 0.06 to 0.061 THz, which implies the very high-order 1024-QAM. Then, smaller signal constellations are selected for higher carrier frequencies, due to their larger path loss values. When the distance is 20m, the single-user data rate is approximated as $4 \text{ bits/Hz} \cdot 3 \text{ GHz} + 2 \text{ bits/Hz} \cdot 35 \text{ GHz} + 1 \text{ bits/Hz} \cdot 20 \text{ GHz} = 102$ Gbps.

SINR: The resulting SINR in (87) is evaluated in Fig. 30, with the obtained transmit power. We consider the IBI leakage of 17.47% to the neighboring sub-windows, for the rectangular waveform G in (87). The non-zero SINR values appear when the sub-windows are utilized. When $G_t = G_r = 20$ dBi and $d = 1$m,10 bits/symbol is supported and the SINR reaches 28 dB. Although at some utilized sub-windows such as 0.5-0.55 THz and

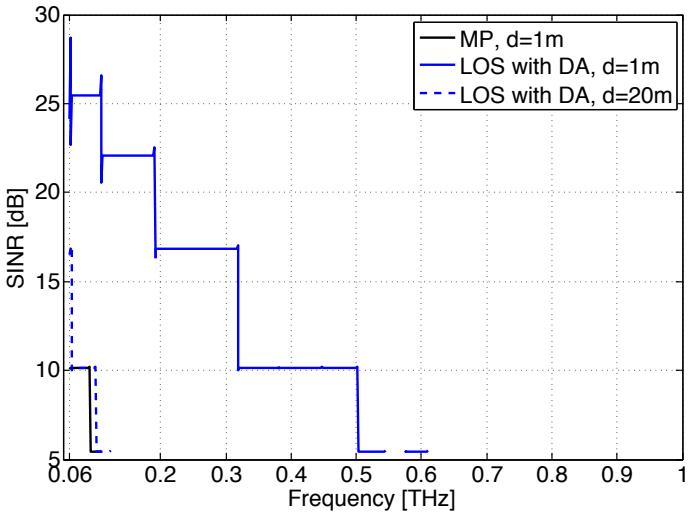

Figure 30. SINR.

0.57-0.61 THz, the SINR drops below 10 dB for γ_{th}, the average BER requirement in (94) is satisfied. Interestingly, the fluctuations in the SINR occur when the constellation rate changes or equivalently, the transmit power changes sharply in the sawtooth shape, for example, at 0.061 THz, 0.1 THz, and 0.19 THz, among others. This is due to the sharp change of the transmit power at these frequencies, which make noticeable effects on the IBI in (86), and consequently, the fluctuations of SINR.

Distance Improvement: The resource allocation model is used to maximize the data rate in (90). while as the main objective, the distance maximization is then analyzed as shown in (88), for a given rate threshold, R_{su}. The data rate performance for the multi-path with $G_t = G_r = 0$ dBi and the LOS with $G_t = G_r = 20$ dBi are illustrated in Fig. 31(a) and 31(b). For comparison, the water-filling capacity is an upper-bound of the achievable data rates, while the equal-power capacity suggests the achievable data rates of the non-adaptive transmission. Moreover, we apply our resource allocation scheme on the state-of-the-art millimeter wave systems, at 0.3 THz [52] and 0.06 THz [10]. In particular, the transmission at 0.3 THz occupies the fixed 50 GHz bandwidth, while the transmission at 60 GHz uses the fixed 10 GHz bandwidth.

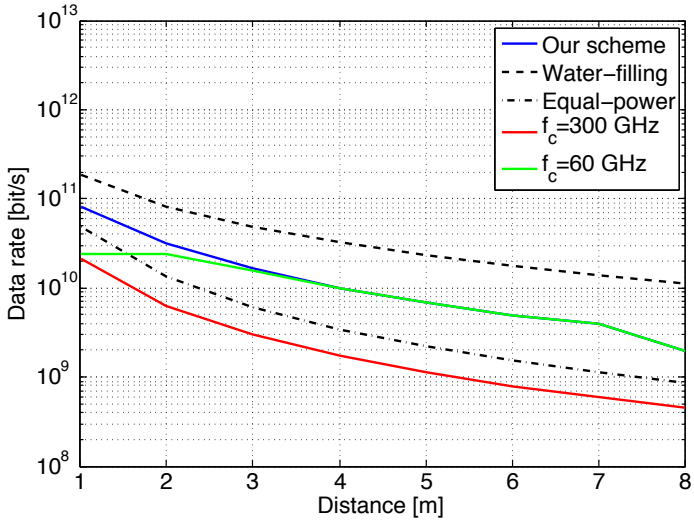

(a) Multi-path with $G_t = G_r = 0$ dBi.

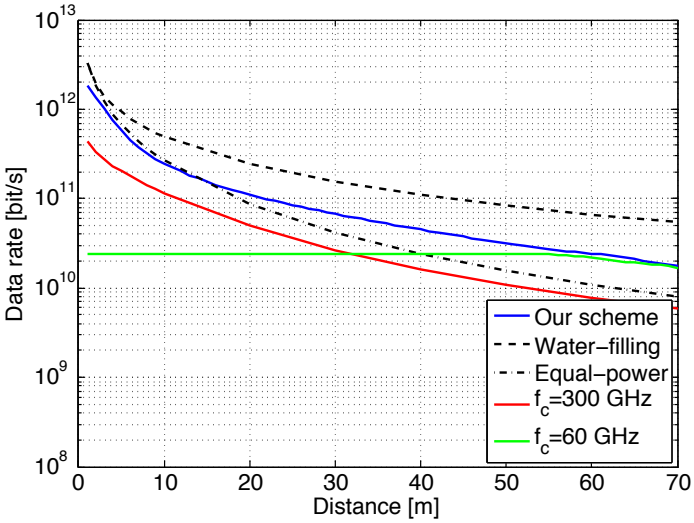

(b) LOS with $G_t = G_r = 20$ dBi.

Figure 31. Data rates in the single-user THz band communication.

Multi-path with $G_t = G_r = 0$ dBi: In Fig. 31(a)), the results based on the resource allocations scheme is significantly higher than the non-adaptive equal-power scheme. This advantage is more notable in the multi-path case since the intelligent allocation of the transmit power and the symbol constellation is more important when the channel quality is compromised. The path loss threshold sets the distance limit as 8m. At 1m, the data rate reaches 81.5 Gbps. If $R_{\text{su}} = 10$ Gbps, the solution to the maximal distance in (88) is equal to 4m. This is greater than the results from the other schemes, such as 2.3m of the equal-power scheme and 1.7m of the 300 GHz system. Interestingly, the performance of the 60 GHz system is very close to our resource allocation scheme (operating over 0.06-1 THz), particularly when $d > 3$m and the channel path loss is high. This can be explained since the resource is allocated to the lower frequency bands with better SINR.

LOS with $G_t = G_r = 20$ dBi: Fig. 31(b) shows that 1 Tbps is achievable with our resource allocation scheme over the 0.06-1 THz band, up to $d = 3$m, since the total usable bandwidth is significantly enhanced with the use of the antenna gains. When the distance is below 10m, the SINR is very high over the sub-windows. Consequently, the resource allocation plays less important role and its data rate is similar to the equal-power scheme. However, the advantage appears as the distance increases. If $R_{\text{su}} = 100$ Gbps, the solution to the maximal distance in (88) is 21m. The significant distance improvement is obtained over the equal-power scheme, and the fixed bandwidth system over 300 GHz, where the results of these two schemes are 17m and 10m. With the high-gain antennas, the data rate of the 60 GHz system is flat over the distance. Comparing to the 60 GHz system, when the distance is small, the advantage of our resource allocation over the 0.06-1 THz band is large, since much bandwidth has high SINR and can be utilized. However, as the distance grows, the path loss drastically increases particularly for the high frequencies. Therefore, the transmission resource is concentrated to the lower frequencies. In particular, when $d \geq 60$m, the performances of the 60 GHz and the entire THz band have negligible difference.

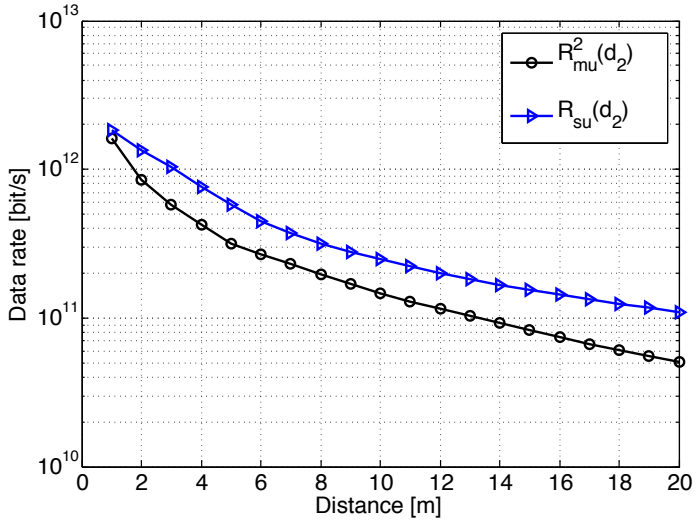

(a) Data rate comparison of the inequality in (118).

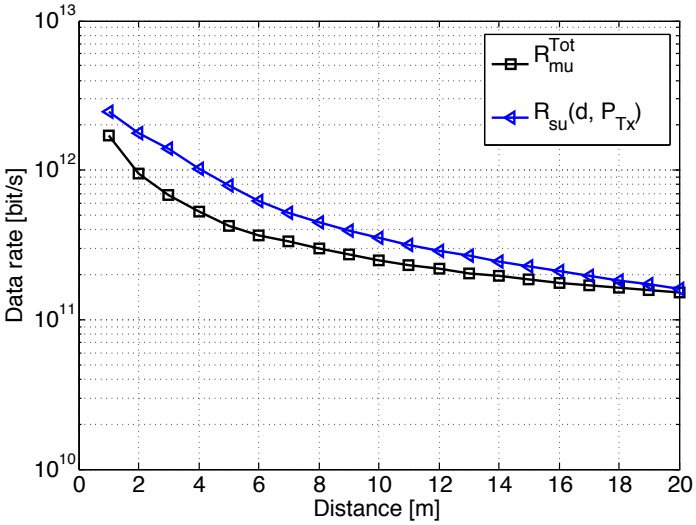

(b) Data rate comparison of the inequality in (119).

Figure 32. Theoretical bounds in the multi-user THz band networks, for LOS with $G_t = G_r = 20$ dBi.

Discussions: In our resource allocation scheme, the resource that includes the transmit power and the signal constellation are preferably distributed to the sub-windows with lower frequencies or equivalently higher SINR. The advantage of our resource allocation becomes more important when the distance is larger, in comparison with the fixed allocation scheme. By using the same resource allocation scheme, to exploit the 0.06-1 THz band has the better performance over the millimeter-wave technologies at 60 GHz and 300 GHz, particular when the distance is small. Furthermore, the distance improvement is significant with our resource allocation model. In particular, 10 Gbps can be supported at 4m in the multi-path channel. On the other hand, 100 Gbps is achieved up to 21m in the LOS transmission with the use of 20-dBi-gain antennas. In light of the spectrum utilization, the actual utilized bandwidth is less than the total usable bandwidth. Hence, the spectrum in the THz band is still under-exploited in the single-user case. This further motivates the design of a strategic spectrum allocation for the multi-user network, as studied in Sec. 5.3.1.

5.4.2 Multi-user THz Band Communication Networks

We next evaluate the distance-aware bandwidth-adaptive resource allocation scheme in a multi-user network in the THz band. Our optimization goal is to maximize the total distance of the ultra-high-speed links, since we intend to support multiple links at the same time and address the distance challenge. Each link needs to reach the data rate greater than $R_{\text{mu}}^{\text{th}}$ in (111). First, we study the theoretical bounds and analyze the performance of the resource allocation scheme in the multi-user network, in terms of the data rate and the distance.

Theoretical Bounds Analysis: We start with link 1 with $d_1 = 21$m, which is the largest distance that can support 100 Gbps for LOS with $G_t = G_r = 20$ dBi. We show that additional links can be concurrently supported by using the unused THz spectrum, without compromising the transmission of link 1. To allocate the second link using the unoccupied spectrum, we check the spectrum pool $\overrightarrow{SP}$ and and apply the flow chart in Fig. 28. To analyze the theoretical bounds, we consider the two-user case and study the attainable data rate, R_2. This can be extended to higher number of multi-user networks, by applying the

same principle.

As illustrated in Fig. 32(a) and Fig.. 32(b), the results are consistent with the inequalities that we developed in Sec. 5.3.4. First, the link data rate in the multi-user network is no greater than that of the single-user link with the same distance, i.e., $R^2_{\text{mu}}(d_2) \leq R_{\text{su}}(d_2)$, as stated in (118). The central part of the spectrum is occupied by link 1 and cannot be used by link 2, which causes this data rate gap. Second, in Fig. 32(b), we observe that $R^{\text{Tot}}_{\text{mu}} \geq R_{\text{su}}(d_1 = 21\text{m}) = 102.4$ Gbps, since the strategic allocation scheme provided in Sec. 5.3.1 utilizes the spectrum resource more efficiently than the single-user case. Third, the results in Fig. 32(b) show that the multi-user data rate is bounded by $R_{\text{su}}(d_2, 2P_{\text{Tx}})$. The second and third observations are supported in (119).

Furthermore, the advantage of $R_{\text{su}}(d_2, 2P_{\text{Tx}})$ decreases as the distance increases, maintaining greater than R_{mu}. This can be explained that the distance-aware bandwidth-adaptive resource allocation scheme in the single-user communication optimizes the modulation and transmit power solutions. As for the data rate, we observe that $R_2 \geq 100$ Gbps is reachable as long as $d_2 \leq 12$m.

Multi-user Ultra-high-speed Network: We find the solution in (107) to maximize the total distance of ultra-high-speed links in the multi-user network. By following the proposed strategic spectrum utilization principle in the flow chart (see Fig. 28), we iteratively allocate the spectrum to multiple users to satisfy the data rate requirement.

Multi-path with $G_t = G_r = 0$ dBi: To start with, we accommodate link 1 at $d_1 = 4$m, which is the largest distance that supports $R^{\text{th}}_{\text{mu}} = 10$ Gbps in this case. Then, by exploiting the rest of the THz spectrum, link 2 is found at $d_2 = 3$m as the largest distance to satisfy the rate requirement. By iterating this process, we obtain 14 links as provided in Table 3. In each iteration, the maximal reachable distance that satisfies $R^{\text{th}}_{\text{mu}}$ is obtained, i.e., $\max d_{i+1}$ while $d_{i+1} \leq d_i$. This process iterates until we reach $d_{14} = 1$m, when the remaining spectrum cannot support a link to exceed $R^{\text{th}}_{\text{mu}} = 10$ Gbps. The number of utilized sub-windows as well as the percentage of the total utilizable bandwidth are also listed for each link.

The overall network data rate in this analysis is 140 Gbps, which is 13 times higher than the single-user rate with $d = 4$m. The sum of the link distances in (107) is equal to 24m. Therefore, in the multi-path channel, fourteen links can be simultaneously supported with $R_{\text{mu}}^{\text{th}} = 10$ Gbps. However, in this case, the utilized spectrum is between 0.06 and 0.2 THz, while much THz frequency bands up to 1 THz are still unused.

LOS with $G_t = G_r = 20$ dBi: Similar process is applied in the LOS case with the high-gain antennas. To start with, we accommodate link 1 at $d_1 = 21$m. Then, by inspecting the spectrum pool, we choose link 2 at $d_2 = 12$m, which is the largest distance to support $R_{\text{mu}}^{\text{th}} = 100$ Gbps transmission with the current spectrum resource. The link information is summarized in Table 3. Importantly, by applying the developed resource allocation scheme in the THz band, thirteen 100 Gbps links can be simultaneously supported in the network. The overall network data rate in this analysis is 1.31 Tbps, which is 12 times higher than the single-user rate with $d = 21$m. The sum of the link distances in (107) is equal to 71m. As the resolution of the link distance becomes finer, more links can be supported simultaneously in the network and consequently, the efficiency of the spectrum utilization can be further enhanced.

Moreover, the ultimate spectrum utilization is demonstrated in Fig. 33, where the constellation rate is shown as the function of the frequency for different links. The entire 0.06-1 THz spectrum is utilized, by using the developed strategic principle, which shows a significant improvement over the single-user case. Specifically, the spectrum between 0.06 THz and 1 THz is fully exploited, while only 60 sub-windows as given in Table 3 (between 0.06 THz and 0.12 THz) are utilized for $d_1 = 21$m. Moreover, the strategic spectrum allocation scheme developed in Sec. 5.3.1 is applied and illustrated in Fig. 33, for example for the links d_7, d_8 and d_9, over the spectrum around 0.6 THz. In particular, the central spectrum is allocated to d_7, while the outer sub-windows are allocated to d_8 and then d_9, which have the lower path losses.

The percentage of the total utilizable bandwidth, which is the ratio between the utilized

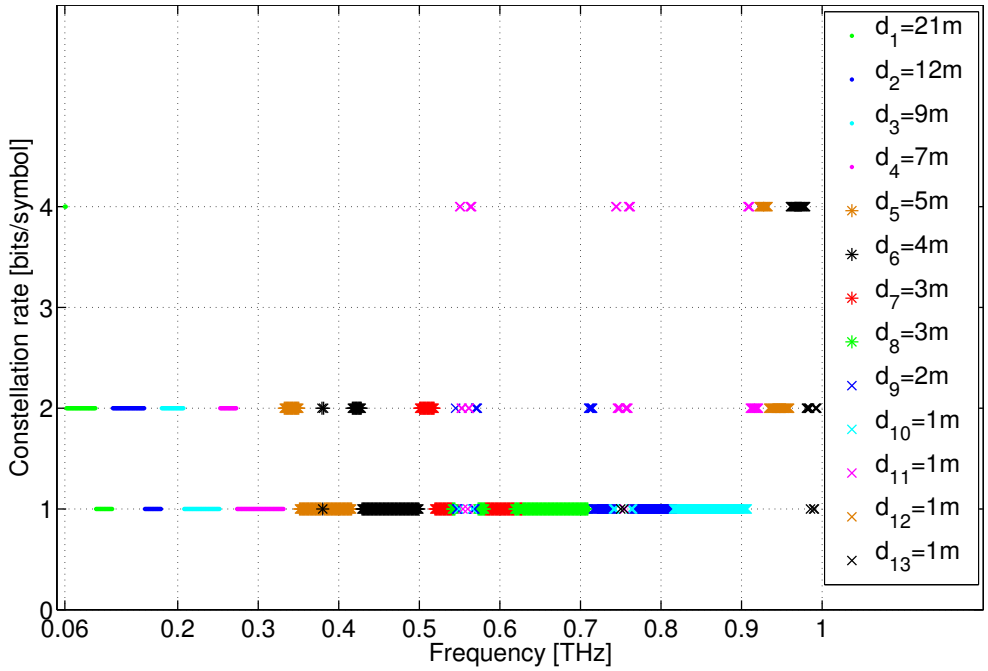

Figure 33. Resource allocation solution in the multi-user network, for LOS with $G_t = G_r = 20$ dBi.

bandwidth and the total utilizable bandwidth at the particular distance, is shown in Table 3. With the smaller distance, the total utilizable bandwidth grows, which results a reduction of the percentage. However, for the same distance and for link i and $i + 1$, the percentage of the link $i + 1$ is greater or equal to that of the link i, since the better sub-windows have already been selected for the link i. To achieve the same data rate $R_{\text{mu}}^{\text{th}}$, more sub-windows are needed for the link $i + 1$. For example, this observation is supported in the results of link 7 and 8, in the LOS communication over 3m.

Comparison: We compare our resource allocation scheme with the non-adaptive scheme, in which the fixed frequency-division, the equal transmit power and the fixed modulation are adopted. In particular, 50 sub-windows are assigned for each user, as suggested in [52]. The equal transmit power (i.e., $P_u = P_{\text{Tx}}/50$), and the fixed 16-QAM modulation (i.e., $k_{\text{fixed}} = 4$) that was designed for the THz system [101] are used on each sub-window. From (92), the resulting threshold SINR to support this transmission over each sub-window is given by

$$\gamma_{\text{th}} = -\frac{(2^{k_{\text{fixed}}} - 1)\ln(5\epsilon_{\text{th}})}{1.5}. \tag{120}$$

However, this non-adaptive scheme fails to support the 100 Gbps link. The largest data rate is equal to 92 Gbps at $d = 1$m, with only 23 sub-windows satisfying the SINR requirement in (120).

Discussions: By using the developed strategic spectrum utilization principle and the resource allocation scheme in the multi-user case, the theoretical bounds of the multi-user data rate are evaluated. Moreover, the spectrum utilization s greatly improved with our scheme. In the multi-path channel, 14 links can be supported simultaneously with $R_{\text{mu}}^{\text{th}} =$ 10 Gbps, and the total distance over these links is 24m. When the high-gain antennas are used for the LOS propagation, thirteen 100 Gbps links can be supported simultaneously. The sum of the distances of these links reaches 71m. The performance of the developed resource allocation scheme is significantly better than the non-adaptive system, due to the successful exploitation of the THz spectrum and the adaption of the transmit power and the modulation.

Table 3. Resource allocation scheme in multi-user networks

MP with $G_t = G_r = 0$ dBi: $R_{\text{mu}}^{\text{th}} = 10$ Gbps														
Link Number	1	2	3	4	5	6	7	8	9	10	11	12	13	14
Distance [m]	4	3	3	2	2	2	1	1	1	1	1	1	1	1
# of Utilized Sub-windows	10	10	10	10	10	10	10	10	10	10	10	10	10	10
% of Utilizable Bandwidth	15%	10%	10%	6%	6%	6%	3.4%	3.4%	3.4%	3.4%	3.4%	3.4%	3.4%	3.4%
LOS with $G_t = G_r = 20$ dBi: $R_{\text{mu}}^{\text{th}} = 100$ Gbps														
Link Number	1	2	3	4	5	6	7	8	9	10	11	12	13	
Distance [m]	21	12	9	7	5	4	3	3	2	2	1	1	1	
# of Utilized Sub-windows	60	61	73	80	82	87	82	101	91	101	33	39	39	
% of Utilizable Bandwidth	8.1%	7.1%	8.3%	8.9%	9%	9.5%	8.9%	10.9%	9.7%	10.7%	3.5%	4.1%	4.1%	

5.5 Conclusions

In this chapter, we developed a novel distance-aware bandwidth-adaptive resource allocation scheme is developed in the THz band communication network, with the objectives to: 1) improve the communication distance, 2) capture the unique channel peculiarities, and 3) strategically utilize the spectrum to enable multiple ultra-high-speed links. Based on the developed scheme, we solve the solutions to the sub-windows allocation, the modulation adaptation and the transmit power control in the resource allocation model, for both single-user and multi-user communications.

The numerical results show that the developed resource allocation scheme improves the distances and the exploitation of the THz spectrum significantly. Specifically, for the single-user communication, 10 Gbps can be supported at 4m in the multi-path channel, while 100 Gbps is achieved up to 21m in the LOS transmission with the use of 20 dB gain antennas. In the multi-user network, fourteen 10 Gbps links can be supported simultaneously in the multi-path channel. With the use of 20 dB gain antennas, thirteen 100 Gbps links can be supported at the same time. Moreover, the developed resource allocation scheme outperforms the existing millimeter-wave systems at 60 GHz and 300 GHz, as well as the non-adaptive scheme. This work achieves the design objectives and contributes to enabling multiple ultra-high-speed links in the THz band communication network.

CHAPTER 6

THREE-DIMENSIONAL END-TO-END MODELING AND ANALYSIS

In this chapter, we develop an analytical 3-D end-to-end model in the THz band, which includes the responses of the graphene-based reflectarray antenna and the 3-D multi-path propagation channel. In particular, the architecture of a graphene-based reflectarray antenna is investigated and the 3-D radiation pattern is modeled. Moreover, a 3-D THz channel model is developed based on ray tracing techniques, as a superposition of the LoS, reflected and scattered paths. Using the developed model, we present an in-depth analysis on the 3-D channel characteristics and the influence of directivity from graphene-based reflectarray antennas in the THz band. In particular, we thoroughly characterize the antenna gain and the beamwidth, the delay spread and the coherence bandwidth, the 3-D angular spread, the wideband channel capacity, and the beam misalignment influence. The provided analysis and the channel physical parameters lay out the foundation and are particular useful for the physical and upper layers design for reliable and efficient ultra-high-speed wireless communications in the THz band.

6.1 Motivation and Related Work

For the realization of efficient wireless communication networks in the THz band, it is imperative to develop an accurate 3-D channel model which accurately characterizes the Terahertz spectrum peculiarities in both the elevation and azimuth planes. In realistic application scenarios, the multi-path rays arrive at the receiver from both the azimuth and elevation planes, which is the result of the 3-D radiation diagram of the antennas and the 3-D propagation of the electromagnetic waves in the channel. These facts introduce an angular spread in the elevation plane, and influence the channel physical peculiarities. The first model that recognizes the elevation coordinate in a 3-D model was proposed in [102],

in which the author assumed the arriving signals were uniformly distributed in the azimuth plane and non-uniformly distributed in the elevation plane. Further development provides analytical solutions of the power spectral density of the received signal in the three dimensions and produces the desired spatio-temporal characteristics of 3-D wireless channels as studied in [103, 104]. However, these models for lower frequency bands do not capture the behavior of the THz band, such as the very high molecular absorption loss or the very high reflection loss. Existing THz band channel models in [56, 28, 52, 105] are developed for 2-D cases, which fail to describe signal variations in the elevation plane. Furthermore, THz antenna responses are not included in these models. Consequently, there is a need for a end-to-end model, which captures the antenna response and the 3-D multi-path propagation, and investigate the resulting channel characteristics.

Graphene-based antennas to operate in the THz band are suggested in [42, 43, 44, 45, 27], due to the fact that graphene supports the propagation of surface plasmon polariton (SPP) waves. The main merit of using graphene-based antennas is that the equivalent electrical size is much larger than its physical dimensions, owing to the much lower speed of SPP waves in a graphene-based antenna compared to that of free-space electromagnetic waves in a metallic antenna [27]. To overcome the very high path loss at THz frequencies, reflectarray antenna technologies [46] are very attractive among others, by taking advantages of parabolic reflectors and phased arrays. This approach is especially fruitful to provide high directivity gain with low losses at high frequencies such as the THz band. In the literature, reflectarray antennas have been studied in microwave and millimeter-wave bands [47], and more recently experimentally demonstrated [48] and theoretically analyzed at THz frequencies [49, 50], from the antenna design perspective. However, the integration of the graphene-based reflectarray antenna response into the THz band channel model, and the influences on the channel peculiarities have not been characterized from the communication perspective.

6.2 A 3-D End-To-End Model in the Terahertz Band

In this section, we develop an end-to-end model, which includes frequency response in a 3-D environment from the transmitting to the receiving antenna in the (0.1-10) THz band. Since the wave propagation in the THz band is frequency-dependent, the model is developed as a combination of a number of sub-bands, which are narrow enough to be considered as flat fading channels. The operating frequency, f, takes values from $\{f_1, f_2 \ldots, f_n, \ldots\}$, where f_n is the center frequency of the n^{th} sub-band. The bandwidth of each sub-band is identical and equal to $\Delta f = f_{n+1} - f_n$.

In the end-to-end channel model, the transfer function $H_{\text{e2e}}(f)$ of the end-to-end response can be expressed as a sum of the transfer function of all arrival rays,

$$H_{\text{e2e}}(f) = \sum_{i=1}^{I} A_T^{(i)}(f) H^{(i)}(f) A_R^{(i)}(f), \tag{121}$$

where $A_T^{(i)}$ and $A_R^{(i)}$ denote the frequency responses of the transmitting and the receiving antennas for the i^{th} ray. Moreover, $H^{(i)}$ describes the frequency response of i^{th} ray propagating in the THz channel. I is the total number of multi-path components in a 3-D environment. Even with antenna directivity, the antenna radiation pattern has 3-D beamwidth, which results in the fact that the multi-path effect still exists but is confined in the radiation sector [106, 107]. Indeed, the number of multi-path components decreases with the reducing antenna beamwidth. In the following, we describe the mathematical models to capture the graphene-based reflectarray antenna response and characterize the 3-D multi-path channel in the THz band.

6.3 Graphene-based Reflectarray Antenna Response

The main constraint of THz band communications is imposed by the very high and frequency-selective path loss, which can easily above 100 dB for distances over 1m [56]. One promising approach to enhance the received power is to provide directivity gain by using reflectarray antenna technologies, which has been experimentally demonstrated [48] and theoretically analyzed at THz frequencies [49, 50]. By reflecting the incident waves from a THz

source, the far-field radiation pattern can be collimated and created as a pencil-sharp beam in a desired direction, as illustrated in Fig. 34.

In this architecture, the reflectarray consists of an array of graphene reflective cells, which introduce appropriate phase-shift from reflection of the incident THz waves. The resulting radiation from the far-field becomes a pencil-sharp beam. This design combines the features of parabolic reflectors and conventional phased arrays with low losses, compact profile and high efficiency. In the following of this section, the complex conductivity of graphene, the complex wave vector and ultimately, the radiation pattern of reflectarray antenna are investigated.

6.3.1 Complex Conductivity of Graphene

Graphene can be modeled as an infinitely thin surface with complex conductivity due to its mono-atomic thickness. Then, the conductivity σ_g is given as a sum of the intraband σ_{intra} and interband σ_{inter} contributions according to Kubo's formula [108, 109],

$$\sigma_g(f) = \sigma_{\text{intra}}(f) + \sigma_{\text{inter}}(f), \tag{122}$$

where

$$\sigma_{\text{intra}}(f) = \frac{jq_e^2}{\pi\hbar^2(2\pi f + j/\tau)} \cdot \int_0^\infty n_F(\epsilon - E_F) - n_F(\epsilon + E_F)d\epsilon, \tag{123}$$

$$\sigma_{\text{inter}}(f) = j2q_e^2 f \int_0^\infty \frac{n_F(\epsilon - E_F) - n_F(-\epsilon - E_F)}{(2\epsilon)^2 - (2\pi f\hbar + j/2\tau)}d\epsilon. \tag{124}$$

In the above equations, q_e is the electron charge,$\hbar$ refers to the reduced Planck constant, E_F is the Fermi level, n_F denotes the Fermi-Dirac distribution function, and τ is the momentum relaxation time due to the carrier intraband scattering. By considering only the intraband contribution and completing the intergral in (123), an approximation to (122) is given by

$$\sigma_g(f) \approx -\frac{jq_e^2 k_B T}{\pi\hbar^2(2\pi f - j/\tau)}\left(\frac{\mu_c}{k_B T} + 2\ln\left(\mathrm{e}^{-\mu_c/k_B T} + 1\right)\right), \tag{125}$$

where k_B represents the Boltzmann constant, T is the temperature, and μ_c denotes the chemical potential.

6.3.2 Complex Wave Vector of Graphene

The complex wave vector of SPP waves in graphene determines the propagation properties of SPP waves, and is dependent on the conductivity in (125). The dispersion equation that relates the complex wave vector k_{spp}, the complex conductivity σ_g, and the permittivity ϵ_r of the surrounding materials of graphene patches, is described as

$$\frac{\epsilon_{r1}}{\sqrt{k_{\text{spp}} - \epsilon_{r1} k_0^2}} + \frac{\epsilon_{r2}}{\sqrt{k_{\text{spp}} - \epsilon_{r2} k_0^2}} = -\frac{j\sigma_g}{2\pi f \epsilon_0}, \tag{126}$$

where ϵ_{r1} and ϵ_{r2} denote the permittivity values of the materials above and below graphene patches, respectively. Moreover, ϵ_0 refers to the vacuum permittivity, and $k_0 = 2\pi f/c$ is the free space wavenumber where c is the speed of light in vacuum.

As shown in Fig. 34, the graphene patch is a rectangular nano-strip and has a finite length l and width w. Since the SPP mode can propagate on finite width nano-strips, a condition on the nano-strip length that results from the complex wave vector in (126) to support standing wave resonances is

$$\begin{aligned} l &= \alpha \frac{\lambda_{\text{spp}}}{2} \\ &= \alpha \frac{\pi}{\text{Re}\{k_{\text{spp}}\}}, \end{aligned} \tag{127}$$

where $\lambda_{\text{spp}} = 2\pi/\text{Re}\{k_{\text{spp}}\}$ stands for the SPP wavelength, and α is an integer SPP mode number.

6.3.3 Radiation Pattern of Reflectarray Antenna

In Fig. 34, the THz source is assumed to have a phase center located at the origin of the 3-D axes. The $(m, n)^{\text{th}}$ cell of the reflectarray scatters the incoming ray from the source to a desired direction, by applying a phase correction. By denoting $\vec{p}_{mn}$ as the position vector of the incoming ray from the source, and $\hat{p}_o$ as the desired direction of the pencil-sharp beam, the phase of the reflectarray needs to satisfy

$$k_0(\vec{p}_{mn} - \vec{P}_{mn} \cdot \hat{p}_o) - \psi_{mn} = 2\pi\beta, \tag{128}$$

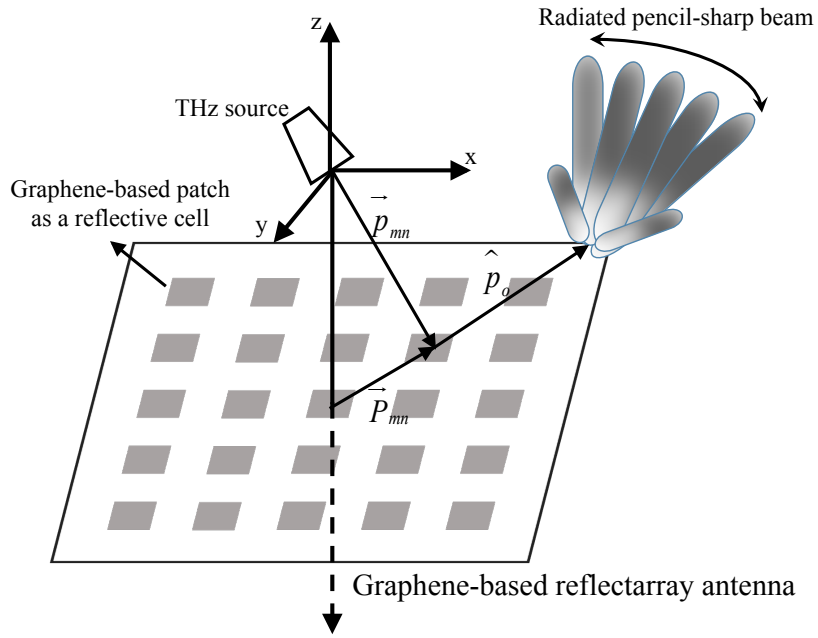

Figure 34. An architecture of graphene-based reflectarray antenna.

where $\vec{P}_{mn}$ is a position vector of the $(m,n)^{\text{th}}$ cell, and $\beta \geq 0$ is an integer. A phase shift ψ_{mn} is introduced between the incident and scattered field from the $(m,n)^{\text{th}}$ reflectarray cell, to allow that the phase of the scattered field from the entire reflectarray is uniform in a plane normal to the direction of the desired beam $\hat{p}_o$. This results in that the reflectarray collimates the waves from the THz source into a pencil-sharp beam in the far-field.

Based on the proposed architecture in Fig. 34, the far-field radiation gain of the reflectarray in the direction (θ,ϕ) at the frequency f can be obtained as

$$A_T(f) = \eta_s G_g(f,\theta,\phi)\cos(\theta)\cdot\sum_{n=0}^{N-1}\sum_{m=0}^{M-1} R_{mn}\left(f,\theta_{mn},\phi_{mn},\psi_{mn}\right)$$
$$\cdot\exp\left(jk_0\left[x'_{mn}\sin(\theta)\cos(\phi)+y'_{mn}\sin(\theta)\sin(\phi)\right]+j\psi_{mn}\right), \qquad (129)$$

where M,N are the number of cells in the x-axis and y-axis of the reflectarray, η_s is the radiation efficiency of the THz source, and G_g describes the gain of the individual nano-strip graphene-based patch.

Importantly, R_{mn} denotes the magnitude of the reflection coefficient of the $(m,n)^{\text{th}}$ cell of the graphene reflectarray, which depends on the graphene conductivity as obtained in (125),

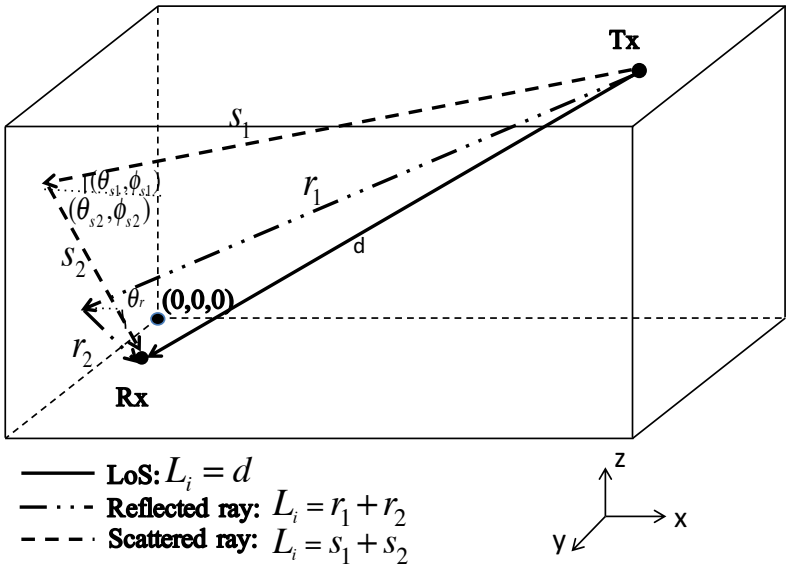

Figure 35. A 3-D geometry of THz propagation model between the transmitter (Tx) and the receiver (Rx).

the wave vector of SPP waves in graphene as computed in (126), the nano-strip length as provided in (127), and the phase correction as analyzed in (128).

On the other hand, the frequency response of the graphene antenna at the receiver is computed as:

$$A_R(f) = \sqrt{e_R(f) D_R(f,\theta,\phi)\frac{\lambda^2}{4\pi}}, \tag{130}$$

where e_R is the receiver antenna radiation efficiency. D_R is the directivity of the receiving antenna, which is a function of frequency, the elevation and the azimuth angles of arrival. Here we assume an omni-directional receiving antenna, in which the radiation efficiency is unitary and the directivity is uniform in the elevation and azimuth planes. Hence, the impact of the graphene-based reflectarray antenna at the transmitter on the 3-D channel response is investigated as a focus.

6.4 3-D Channel Model in the Terahertz Band

In this section, we develop a 3-D THz channel model based on ray tracing techniques, as a superposition of the LoS, reflected and scattered paths. The ray tracing techniques have been proved to enable very good prediction capabilities at Terahertz frequencies [8, 28].

The diffraction path can be ignored in general since it contributes negligibly to the received signal power. The only exception is when the receiver is in the very closed region near the incident shadow boundary [59], which is not considered in this work. The geometry configuration is demonstrated in Fig. 35, where the traveling distance of the i^{th} ray is given by

$$L_i = \begin{cases} d & \text{LoS} \\ r_1 + r_2 & \text{Reflected Rays} \\ s_1 + s_2 & \text{Scattered Rays} \end{cases} \tag{131}$$

where d is the direct distance between the transmitter and the receiver. For reflection, r_1 is the distance from the transmitter to the reflecting point, and r_2 is the distance from the reflecting point to the receiver. For scattering, s_1 is the distance from the transmitter to the scattering point, and s_2 is the distance between the scattering point to the receiver.

The channel transfer function for the i^{th} ray $H^{(i)}$ in (121) is given as

$$H^{(i)}(f) = \begin{cases} \left| \frac{c}{4\pi \cdot f \cdot d} \mathrm{e}^{-\frac{1}{2}k_{\text{ma}}(f)d} \right| \cdot \exp\left(-j2\pi f \tau_i\right) & \text{LoS} \\ \left| \left(\frac{c}{4\pi \cdot f \cdot (r_1+r_2)} \right) \mathrm{e}^{-\frac{1}{2}k_{\text{ma}}(f)(r_1+r_2)} \cdot \gamma_{\text{TM}}(f) \cdot \rho(f) \right| \cdot \mathrm{e}^{-j2\pi f \tau_i} & \text{Reflected Rays} \\ \left| \left(\frac{c}{4\pi \cdot f \cdot (s_1+s_2)} \right) \mathrm{e}^{-\frac{1}{2}k_{\text{ma}}(f)(s_1+s_2)} \cdot S(f) \right| \cdot \mathrm{e}^{-j2\pi f \tau_i} & \text{Scattered Rays} \end{cases} \tag{132}$$

where $\tau_i = L_i/c$ is the time-of-arrival of the ray and c denotes the speed of light.

In the LoS model, k_{ma} is the frequency-dependent medium absorption coefficient, which depends on the composition of the transmission medium and is detailed in [56]. In the reflected ray model, the Fresnel reflection coefficient for the transverse magnetic (TM) polarized waves γ_{TM} on a smooth surface, which is consistent with the SPP mode on the

graphene-based reflectarray according to (126), is computed as

$$\begin{aligned}\gamma_{\mathrm{TM}}(f) &= \frac{\sqrt{1-\left(\frac{1}{n_t}\sin(\theta_{\mathrm{r}})\right)^2} - n_t\cos(\theta_{\mathrm{r}})}{\sqrt{1-\left(\frac{1}{n_t}\sin(\theta_{\mathrm{r}})\right)^2} + n_t\cos(\theta_{\mathrm{r}})} \\ &= 1 - \frac{2n_t\cos(\theta_{\mathrm{r}})}{\sqrt{1-\left(\frac{1}{n_t}\sin(\theta_{\mathrm{r}})\right)^2} + n_t\cos(\theta_{\mathrm{r}})} \\ &\approx 1 + \frac{-2n_t\cos(\theta_{\mathrm{r}})}{\sqrt{1-\frac{1}{n_t^2}}} \\ &\approx \exp\left(\frac{-2n_t\cos(\theta_{\mathrm{r}})}{\sqrt{1-\frac{1}{n_t^2}}}\right), \end{aligned} \tag{133}$$

where θ_{r} is the angle of incident wave and can be computed using the law of cosine, i.e., $\theta_r = \frac{1}{2}\cos^{-1}\left(\frac{r_1^2+r_2^2-d^2}{2r_1r_2}\right)$. In addition, n_t refers to the refractive index, varying with the frequencies and reflecting material. As we consider the reflected rays with large incident angles, the Taylor's approximation for the smooth surface reflection coefficient in (133) shows good accuracy at Terahertz frequencies. In the scattered ray model, the scattering coefficient is obtained in Chapter 2.3.

The theoretical 3-D end-to-end model in (121) consists of the graphene reflectarray antenna response and the 3-D multi-path propagation phenomena. In particular, the multi-path propagation model in the THz band in (132) was partially validated in Chapter 2.4 and [28]. Therefore, we next focus on the characterization analysis on the 3-D channel and the influence of directivity from the graphene-based reflectarray antenna in the THz band.

6.5 3-D Channel Characterization

Using the developed propagation model, we present a detailed analysis of the 3-D end-to-end channel characteristics in the THz Band. In particular, we thoroughly characterize the reflectarray antenna gain and the beamwidth, the delay spread and the coherence bandwidth, the 3-D angular spread, the channel capacity, and the beam misalignment effect.

Simulation Setup: The simulation is conducted by considering a indoor environment of dimensions 5m× 4m× 3m, such as a passenger car as shown in Fig. 35. The transmitter

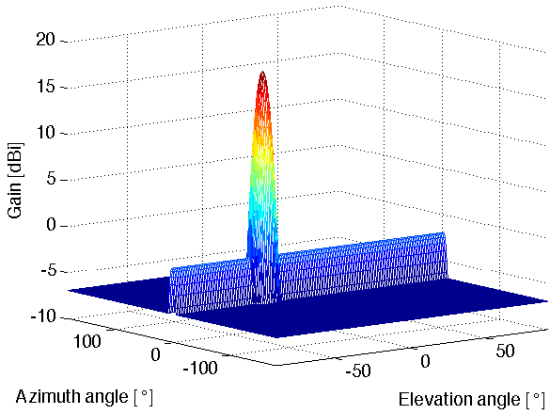

(a) Gain in 3-D spherical view.

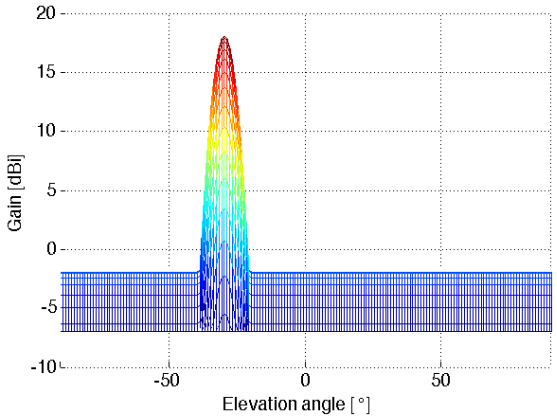

(b) Gain in the elevation plane.

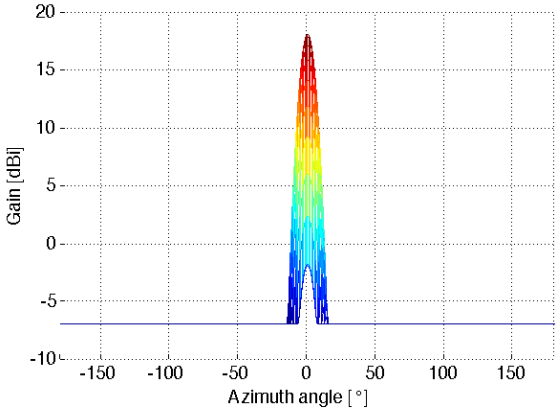

(c) Gain in the azimuth plane.

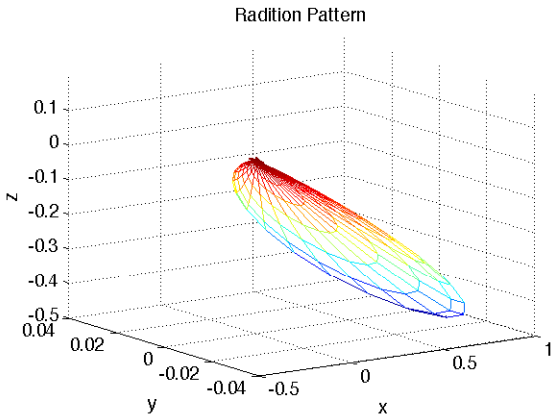

(d) Radiation Pattern in 3-D cartesian view.

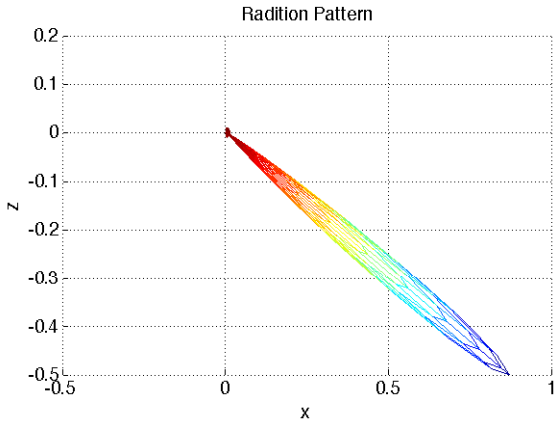

(e) Radiation Pattern in the x-z plane.

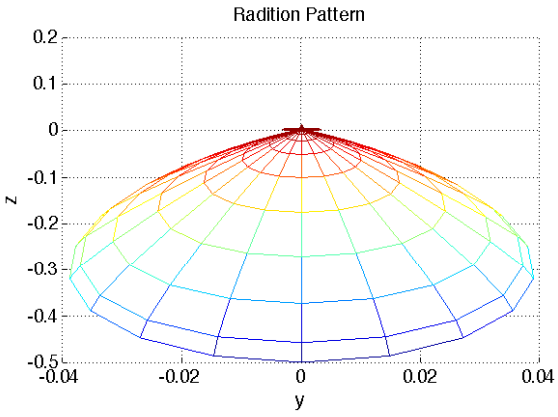

(f) Radiation Pattern in the y-z plane.

Figure 36. Gain of a graphene-based reflectarray antenna in 3-D.

(Tx) is located at (4.8m, 2m, 2.9m), and the receiver (Rx) is located at (0.1m, 2m, 1m). At the transmitter, a graphene-based reflectarray antenna is deployed to provide the directivity gain. On the contrary, an omni-directional antenna is considered at the receiver. Multi-path components in the 3-D environment are captured at the receiver, in which the LoS, the once-reflected, the twice-reflected and the scattered rays are included. The walls are covered by plaster, where its refractive index can be found in [57], while the interactions with the ceiling and the ground are neglected. In the simulations, the main beam of the reflectarray antenna points at the LoS direction.

6.5.1 Reflectarray Antenna Gain and Beamwidth

Based on the expression in (129), the far-field gain of the graphene-based reflectarray antenna is numerically evaluated in the spherical coordinates, as illustrated in Fig. 36(a). The maximum gain is 18 dBi in the main lobe, at the frequency of 1 THz. By contrast, the side lobes stay more than 25 dB below the main beam and hence, are neglected in the figures. The 3-dB beamwidths in the elevation and azimuth planes are 7° and 10° respectively, as shown in Fig. 36(b) and Fig. 36(c). Converting to the cartesian coordinates, the far-field radiation pattern is plotted in Fig. 36(d). In particular, a downtilt angle of 30° can be observed from the radiation pattern in the x-z plane (see Fig. 36(e)), which is consistent with the results in Fig. 36(b). On the other hand, a uniform radiation pattern can be found in the y-z plane in Fig. 36(f).

Note that the direction of the main beam can be directed adaptively, by varying the incident angle from the THz source as seen in Fig. 34, or tuning the phase shifts of the reflectarray according to (128). On the one hand, the incident angle has very small impact on the reflection coefficient in graphene-based cells, i.e., less than 1 dB difference according to [49]. Hence, the variation of the incident angle influences the radiation direction while has no considerable changes in the shape of the main beam. On the other hand, the graphene-based reflectarray offers the possibility to control the phase of the reflected field at the individual cell level and hence, dynamically reconfigure the far-field

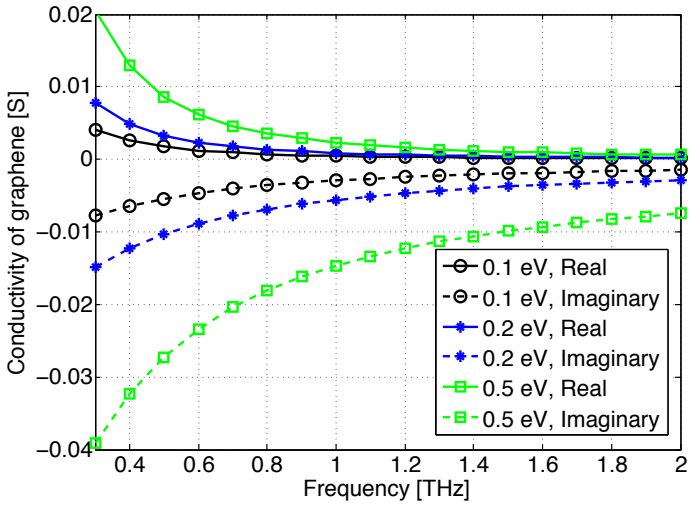

Figure 37. Complexity conductivity of graphene, for a varying chemical potential.

radiation pattern [110]. This is achieved by tuning the complex conductivity of graphene through chemical potential variations. For example, as the chemical potential increases from 0.1 eV, 0.2 eV, to 0.5 eV, the absolute values of the real and imaginary parts of the graphene conductivity rise, as shown in Fig. 37. In addition, the conductivity decreases with an increasing frequency.

6.5.2 Delay Spread and Coherence Bandwidth

Based on the geometry in Fig. 35, the power delay profile with the graphene-based reflectarray antenna is summarized in Table 4. To compare, we also include the results by considering an omni-directional antenna at the transmitter. At the receiver, the LoS, the once-reflected, the twice-reflected and the scattered rays are captured with different delays and gains. Furthermore, the main channel physical parameters such as the total power gain, the average delay, the rms delay spread and the coherence bandwidth are calculated for the two different cases.

The observations from Table 4 are summarized as follows. The total power gain increases from -109.23 dB to -91.62 dB when the reflectarray antenna is used, and the gain enhancement matches with the gain of the reflectarray antenna as analyzed in Sec. 6.5.1.

Table 4. Power Delay Profile in the 3-D channel at $f = 1$ THz

		Reflectarray antenna	Isotropic antenna
	Delay [ns]	Path Gain [dB]	Path Gain [dB]
LoS	16.91	-91.66	-109.66
Reflected Ray 1	17.53	-111.57	-129.57
Reflected Ray 2	18.15	-137.13	-130.13
Reflected Ray 3	21.54	-130.47	-123.47
Reflected Ray 4	21.54	-130.47	-123.47
Twice Reflected Ray 1	18.78	-157.43	-150.43
Scattered Ray 1	17.87	-125.13	-140.13
Scattered Ray 2	18.49	-163.79	-156.79
Scattered Ray 3	21.87	-147.88	-140.88
Scattered Ray 4	21.88	-166.01	-159.01
Total Path Gain [dB]		-91.62	-109.23
Average Delay [ns]		19.46	19.46
RMS Delay Spread [ns]		0.099	1.23
Coherent Bandwidth [GHz]		2.0	0.16

In addition, the rms delay spread can be obtained as

$$\sigma_{delay} = \sqrt{\overline{\tau^2} - (\overline{\tau})^2}, \tag{134}$$

$$\overline{\tau^x} = \frac{\sum_{i=1}^{I} |\alpha_i|^2 |\tau_i|^x}{\sum_{i=1}^{I} |\alpha_i|^2}, \tag{135}$$

where $\overline{\tau^x}$ describes the first (x=1) or second (x=2) moment of the instantaneous power-delay profile. α_i is the path gain amplitude of the i^{th} path, as $\alpha_i = |A_T^{(i)}(f) H^{(i)}(f) A_R^{(i)}(f)|$ according to (121).

The reflectarray antenna confines the radiation pattern, which results that the number of significant multi-path components decreases. Consequently, the rms delay spread reduces from 1.23 ns to 99 ps. The coherence bandwidth, which is computed as $0.2/\sigma_{delay}$, reaches 2 GHz when the reflectarray antenna is used, which is 12.5 times as large as that in the omnidirectional antenna case. This indicates a large range of frequencies over which the channel can be considered as flat. We realize that these values of the coherence bandwidth are smaller than the results in the our prior multi-path channel model in [28]. This is due to the variation of the simulation environment and the inclusion of the 3-D components that introduces a additional delay spread from the elevation plane.

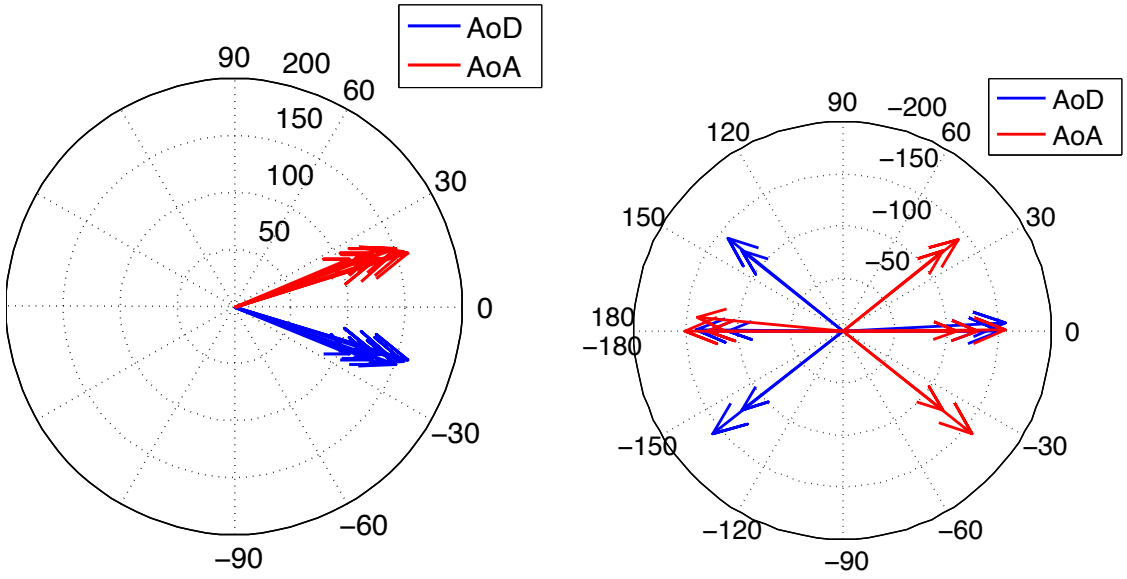

(a) (a) Elevation PAP.

(b) (b) Azimuth PAP.

Figure 38. Power angle profiles (PAP) for AoD and AoA.

6.5.3 3-D Angular Spread

The angular spread is an important factor to evaluate the spatial characteristics of the 3-D channel. To evaluate this, the power angle profiles (PAP) for the elevation angle-of-departure (AoD) and angle-of-arrival (AoA) are demonstrated in Fig. 38(a). In particular, the zero degree lies in the x-y plane, and the degree increases as pointing upwards in the positive z-axis. This suggests the range of the elevation angles is between $-90°$ and $90°$. Since the Tx is located near the ceiling pointing downwards (see Fig. 35), the elevation AoDs are below zero degrees. Correspondingly, the elevation AoAs are reciprocal with EAoD and greater than zero degrees.

To evaluate the spread of the elevation angle profile, the rms angular spread can be obtained in a similar fashion as the rms delay spread, by replacing the delay τ in (134) and (135) with the angle θ [111]. The resulting rms angular spread in the elevation plane is $0.12°$, which is $1/10$ of the rms angular spread in the omni-directional antenna case. The elevation angular spread varies and has some dependency on the heights of the transmitter and the receiver, the communication distance and the propagation environment. In general,

the elevation angular spread increases when the height difference between the transmitter and the receiver reduces, and when the communication distance decreases.

On the other hand, the azimuth AoD and AoA are demonstrated in Fig. 38(b), in which a reciprocity between the AoD and AoA can be observed. Different from the elevation PAP, the range of the azimuth angles extends to -180° and 180°. The zero degree points to the positive x-axis, and the degree increases clockwisely, towards the positive y-axis. The propagation rays travel through the different directions in the azimuth plane, such as the reflections on the left, right, front and back surfaces in Fig. 35. The resulting azimuth rms angular spread is 1.3°. Although the rays propagate in a large range of azimuth angles, the rms angular spread in the azimuth plane is small, due to the beamforming effect by using the reflectarray antenna.

6.5.4 Wideband Channel Capacity

The wideband capacity in the 3-D end-to-end model in the THz band can be calculated as

$$C = \sum_{n=1}^{N} \Delta f \log(1 + \frac{|H_{\text{e2e}}(f_n)|^2 P_n}{\Delta f W_N}), \tag{136}$$

where N refers to the total number of sub-bands for the transmission, $\Delta f = 1$ GHz is the width of each sub-band that is smaller than the coherence bandwidth found in Sec. 6.5.2, to ensure narrowband communications. P_n denotes the transmit power in the n^{th} sub-band and the total transmit power $\sum_{n=1}^{N} P_n$ is fixed. H_{e2e} is the transfer function as given in (121), and $W_N = -85$ dBm/GHz stands for power spectral density of the additive white Gaussian noise. Since the graphene-based antenna can support wideband transmissions, whose bandwidth can reach up to 15% of the carrier frequency [49], a bandwidth of 100 GHz is considered to compute the capacity.

The wideband channel capacities under the water-filling (WF) and equal-power (EP) allocation schemes are numerically evaluated, for the different transmit power levels at the distance $d = 5$m. The WF allocation scheme has one higher order of magnitude of capacity than the EP scheme in general. In Fig. 39(a), the 18-dB-gain graphene-based reflectarray

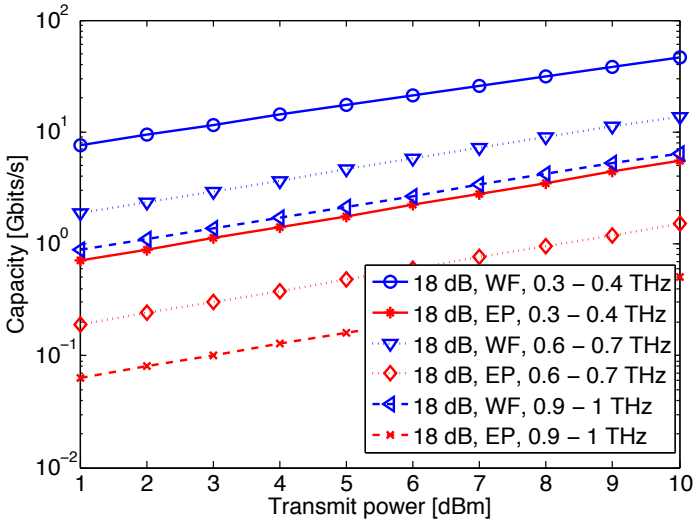

(a) Capacity over the three frequency bands, namely, 0.3-0.4 THz, 0.8-0.9 THz and 1.9-2.0 THz.

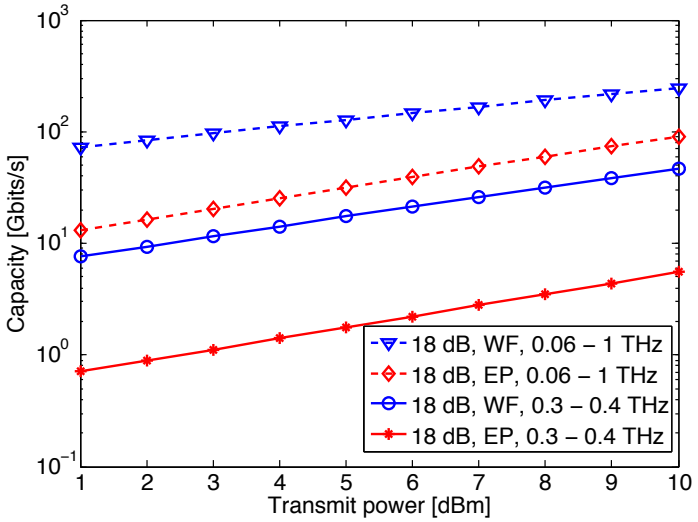

(b) Capacity over the entire 0.06-1 THz band versus 0.3-0.4 THz.

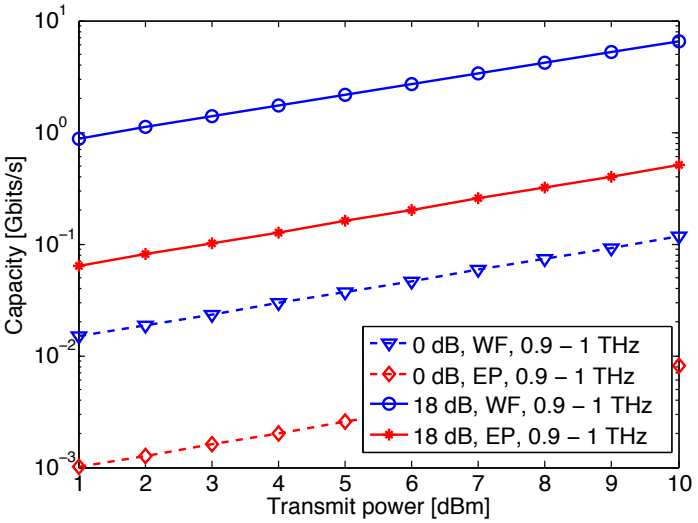

(c) Capacity with the 18 dB reflectarray gain versus the omni-directional antenna.

Figure 39. Wideband capacity for 3-D channels at d = 5m, for the varying transmit power and the water-filling (WF) and equal-power (EP) allocation schemes.

antenna is used at the transmitter. The capacities for the three different bands, namely, (0.3-0.4) THz, (0.6-0.7) THz, and (0.9-1) THz are compared. Due to the degradation of the path gain, the channel capacity decreases as the frequency increases. In particular, the capacity over (0.3-0.4) THz is nearly ten times higher than that over (0.9-1) THz.

In Fig. 39(b), the use of the entire (0.06-1) THz band and the utilization of 100 GHz bandwidth are compared. Even with the use of the reflectarray antenna, 100 Gbps rate is not achievable over (0.3-0.4) THz. On the contrary, 100 Gbps can be obtained when the (0.06-1) THz band is simultaneously explored, for the transmit power above 4 dBm under the WF scheme. Furthermore, the capacity over the (0.3-0.4) THz band with the WF scheme is even worse than that over the (0.06-1) THz band with the EP scheme. This shows the substantial advantage of the large bandwidth even when the transmit power is unchanged.

Fig. 39(c) demonstrates the merit of the reflectarray antenna over the omni-directional antenna at the transmitter. With the same transmit power and the same allocation scheme, the capacity is improved by almost one hundred times thanks to the 18 dB reflectarray antenna gain. In the (0.9-1) THz band, 0.1 Gbits/s is achievable when the transmit power is 10 dBm under the WF scheme when there is no transmit antenna gain. By contrast, 6.47 Gbps can be obtained when the reflectarray gain is applied, given the same transmit power and the same allocation scheme. This comparison suggests the significance of the antenna gain for enabling ultra-high-speed communications in the THz band.

6.5.5 Beam Misalignment

In reality, perfect antenna alignment cannot be achieved, and the beam misalignment would degrade the channel performance. To study the effect of the beam misalignment, we assess the channel capacity using (136) for the (0.9-1) THz band with the different antenna gains and the varying levels of misalignment, as illustrated in Fig. 40. The misalignment level is defined as the angle between the actual main beam direction and the perfect alignment direction in the azimuth plane, while the misalignment in the elevation is negligible owing

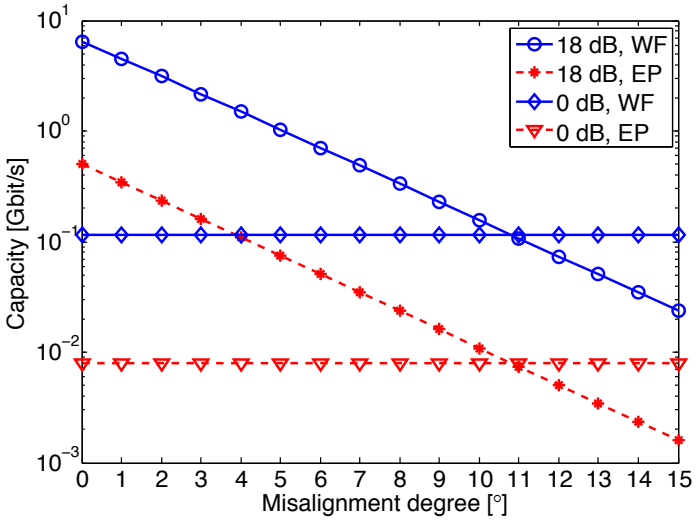

Figure 40. Channel capacity with the beam misalignment. The transmit power is 10 dBm, the frequency band is (0.9-1) THz, and the distance is 5m.

to the very small elevation angular spread, as found in Sec. 6.5.3. The transmit power is 10 dBm under the WF and EP allocation schemes, and the distance is 5m.

When the misalignment angle is 0°, the channel capacity is equivalent to the results discussed in Sec. 6.5.4. As the misalignment angle increases from zero to 15°, the channel capacity decreases considerably, from 6.47 Gbps to 23.5 Mbps, under the WF scheme. This is due to the substantial reduction of the beamforming gain in the reflectarray antenna. The result agrees with the gain and beamwidth analysis in Sec. 6.5.1. In comparison, the channel capacity in the isotropic antenna case keeps at 0.12 Gbps regardless of the increase of the misalignment degree, since the antenna gain is uniform in the 3-D environment. Interestingly, the capacity performance with the reflectarray antenna becomes worse than the omni-directional antenna case when the beam misalignment angle is larger than 11°.

Therefore, the reflectarray brings the beamforming gain, which is significant for enabling ultra-high-speed communications in the THz band. However, the gain is at the cost of a strict beam alignment requirement. Indeed, the requirement for alignment becomes stricter if the beamforming is adopted at both the transmitter and the receiver. The compromise between the directivity gain and the misalignment tolerance is an important factor that needs to be accounted for in the system design.

6.5.6 Discussions

By analyzing the EM wave propagation from the transmit antenna to the receive antenna in the 3-D environment, the channel characteristics are different from the observations in our prior 2-D multi-path channel model [28], and are summarized as follows.

First, additional multi-path rays arrive at the receiver as the elevation plane is incorporated in addition to the azimuth plane. This results in a higher delay spread and a small coherence bandwidth. Second, the angular spread particularly in the elevation plane opens up new opportunities for exploring the diversity gain and also enabling massive MIMO communications with sufficient spatial degrees of freedom. Third, with the use of the graphene-based reflectarray antenna, a 18 dB gain can be achieved in the main beam. This gain improves the channel capacity substantially and equivalently, the communication distance could be enhanced. Fourth, the beamforming gain imposes challenges on the end-to-end link design in terms of the strict 3-D beam alignment requirement.

6.6 Conclusions

In this chapter, we developed a 3-D end-to-end model in the THz band, which includes the responses of the graphene-based reflectarray antenna and the 3-D multi-path channel. In particular, we investigated the architecture of a graphene-based reflectarray antenna and modeled the 3-D radiation pattern. Moreover, we developed the 3-D multi-path channel model based on ray tracing techniques.

By using the developed model, we presented an in-depth analysis on the 3-D channel characteristics. Specifically, first, the gain at the main beam of the graphene-based reflectarray antenna is 18 dB, and the 3-dB beamwidths in the elevation and azimuth planes are 7° and 10° respectively. Second, the use of the reflectarray leads to the decrease of the delay spread from 1.23 ns to 0.099 ns, and the resulting coherence bandwidth reaches 2 GHz. Third, the rms angular spread in the elevation plane is less than 0.12°, which is 1/10 of that without beamforming. Fourth, we analyzed the wideband capacity of the 3-D channel,

which can be enhanced with a larger transmit power, a smaller operating frequency band, a larger bandwidth and a higher beamforming gain. Finally, the beamforming gain enabled by the reflectarray antenna is compromised at the cost of the strict beam alignment, and the deviation needs to be smaller than 11°. The provided analysis and the channel physical parameters lay out the foundation and are particular useful for the physical and upper layers design for reliable and efficient ultra-high-speed wireless communications in the THz band.

CHAPTER 7

CONCLUSIONS

Terahertz band communication offers a very broad bandwidth and is promising to satisfy the need for ultra-high-speed wireless communication in the near future. The use of this spectrum is envisioned to address the spectrum scarcity and capacity limitations of current wireless systems, and enable a plethora of applications in diverse fields.

In this thesis, we aimed to establish the physical layer foundations of the ultra-broadband communication in the THz band. First, we developed a unified multi-path propagation channel is modeled the THz band based on ray-tracing techniques, and analyzed the wide-band characterization including the distance-varying spectral windows, the delay spread and the temporal broadening effects. Second, we proposed a multi-wideband waveform design to improve the distance and support ultra-high-speed transmission. Third, we investigated two algorithms for timing acquisition in the pulse-based wireless systems, namely the LSR algorithm, and the ML-based approach. Fourth, we analyzed the distance-aware bandwidth resource allocation scheme for the single-user and multi-user THz band networks. Fifth, we developed a 3-D end-to-end model is developed and characterized, which includes the responses of the graphene-based reflectarray antenna and the 3-D EM wave propagation channel.

The contributions in each chapter are summarized as follows:

- In Chapter 2, we developed a unified multi-ray channel model in the THz band by using ray tracing techniques. This multi-ray channel incorporates the propagation models for the LoS, reflected, scattered and diffracted paths, is validated by the experimental measurements (0.06 - 1 THz). Using the developed propagation models, we presented an in-depth analysis on the channel characteristics in the THz band. Specifically, we analyzed the distance-varying and frequency-selective nature of the Terahertz channel. Moreover, we studied the coherence bandwidth, and point out the

significance of the delay spread. Furthermore, we characterized the wideband channel capacity using flat and water-filling power allocation strategies. Additionally, we analyzed the temporal broadening effects of the Terahertz channel. Finally, we advocated for distance-adaptive and multi-carrier transmissions to best benefit from the unique relationship between distance and bandwidth.

- In Chapter 3, we proposed a multi-wideband waveform design for the THz band, which includes the features of the pseudo-random time-hopping sequence and the polarity randomization, and allows the dynamical variation of the rate and the transmit power on each sub-window. Moreover, we derived the ISI and the IBI and provided the closed-form expressions of the SINR and BER for the developed multi-wideband waveform. Based in the system model and the waveform design, we formulated an optimization framework to solve for the multi-wideband waveform design parameters of the transmit power and the number of frames, with the aim to maximize the communication distance while satisfying the rate and the transmit power constraints. Four sub-optimal solutions are proposed and compared via extensive numeral analysis.

- In Chapter 4, we proposed and analyzed the LSR and the ML-based algorithms for timing acquisition in the THz band to address the challenges such as the THz band channel peculiarities and the ultra-high sampling rate demand. The error performance of the algorithms has been analytically approximated, where the results have shown good agreements with the simulation results when the SNR is high. Moreover, we analytically and numerically evaluated the two timing acquisition algorithms, in comparison with the CRLB. Furthermore, we studied the BER sensitivity to the acquisition errors in the two algorithms. With the metric of the RMSE, the simulation results showed that when the SNR is high (i.e., greater than 30 dB benefiting from high gain antennas), the LSR algorithm can be used with the uniform sampling at

1/20 of the Nyquist rate, while the ML-based algorithm can be used for low SNR with a time step of 2 to reduce the search space by half. The LSR algorithm can also effectively mitigate the temporal broadening effect due to the frequency-selectivity of the THz channel.

- In Chapter 5, we developed a novel distance-aware bandwidth-adaptive resource allocation scheme is developed in the THz band communication network, with the objective to improve the communication distance. The developed resource allocation scheme captures the unique channel peculiarities, and strategically utilizes the spectrum to enable multiple ultra-high-speed links. In particular, we developed a distance-aware bandwidth-adaptive resource allocation scheme in the THz band communication network, which captures the peculiarities of distance-varying spectral windows and efficiently exploits the Terahertz spectrum. The solutions to the bandwidth utilization, the spectrum allocation, the modulation techniques, and the transmit power are jointly derived. Moreover, we proposed a strategic spectrum allocation principle for the multi-user network, to intelligently allocate the center spectrum of the spectral windows to the long- distance users first, and then the side spectrum to the short-distance users. This principle is evaluated to effectively improve the spectrum utilization and enables multiple ultra-high-speed links in the THz band networks.

- In Chapter 6, we developed a 3-D end-to-end model in the THz band, which includes the responses of the graphene-based reflectarray antenna and the 3-D multi-path channel. In particular, we investigated the architecture of a graphene-based reflectarray antenna and modeled the 3-D radiation pattern. Moreover, we developed the 3-D multi-path channel model based on ray tracing techniques. Using the developed model, we present an in-depth analysis on the 3-D channel characteristics and the influence of directivity from graphene-based reflectarray antennas in the THz

band. In particular, we thoroughly characterize the antenna gain and the beamwidth, the delay spread and the coherence bandwidth, the 3-D angular spread, the wideband channel capacity, and the beam misalignment influence.

The provided physical layer analysis in this thesis lays out the foundation for reliable and efficient ultra-high-speed wireless communications in the THz band.

PUBLICATIONS

Journal Papers

- C. Han, A, O. Bicen, and I. F. Akyildiz, "Multi-Wideband Waveform Design for Distance-adaptive Wireless Communications in the Terahertz Band," IEEE Transactions on Signal Processing, vol. 64, no. 4, pp. 901-922, 2016
- C. Han, and I. F. Akyildiz, "Three-Dimensional End-to-end Modeling and Wideband Analysis for Graphene-enabled Terahertz Band Communications", to appear in IEEE Transactions on Vehicular Technology, 2016
- C. Han, A. O. Bicen, and I. F. Akyildiz, "Multi-Ray Channel Modeling and Wideband Characterization for Wireless Communications in the THz Band," IEEE Transactions on Wireless Communications, vol. 14, no. 5, pp. 2402-2412, May 2015
- I. F. Akyildiz, J. M. Jornet, and C. Han, "Terahertz Band: Next Frontier for Wireless Communications," Physical Communication (Elsevier) Journal, vol 12, pp. 16-32, September 2014
- I. F. Akyildiz, J. M. Jornet, and C. Han, "TeraNets: Ultra-broadband Communication Networks in the Terahertz Band," IEEE Wireless Communications Magazine, vol. 21, no. 4, pp. 130-135, August 2014
- C. Han, and I. F. Akyildiz, "Distance-Aware Bandwidth-Adaptive Resource Allocation in the Terahertz Band", submitted to IEEE Transactions on Terahertz Science and Technology, submitted in September 2015, revised in February 2016
- C. Han, I. F. Akyildiz, and W. H. Gerstacker, "Timing Acquisition Algorithms and Error Analysis for Pulse-based Terahertz Band Communications", submitted to IEEE Transactions on Terahertz Science and Technology, 2016

Conference Papers

- C. Zhang, C. Han, and I. F. Akyildiz, "Three Dimensional End-to-End Modeling and

Directivity Analysis for Graphene-based Antennas in the Terahertz Band," in Proc. of IEEE GLOBECOM, San Diego, USA, December 2015

- C. Han, I. F. Akyildiz, and W. H. Gerstacker, "Timing Acquisition for Pulse-based Wireless Systems in the Terahertz Band," (invited paper) in Proc. of the 2nd ACM NANOCOM, Boston, USA, September 2015
- C. Han, and I. F. Akyildiz, "Distance-Aware Multi-Carrier (DAMC) Modulation in Terahertz Band Communication," in Proc. of IEEE ICC, Sydney, Australia, June 2014

REFERENCES

[1] I. F. Akyildiz, J. M. Jornet, and C. Han, "Terahertz band: Next frontier for wireless communications," *Physical Communication (Elsevier) Journal*, vol. 12, pp. 16 – 32, Sept. 2014.

[2] I. F. Akyildiz, J. M. Jornet, and C. Han, "Teranets: ultra-broadband communication networks in the terahertz band," *IEEE Wireless Communications*, vol. 21, no. 4, pp. 130–135, 2014.

[3] M. Koch, "Terahertz communications: A 2020 vision," in *Terahertz Frequency Detection and Identification of Materials and Objects*, pp. 325–338, Springer, 2007.

[4] R. Piesiewicz, T. Kleine-Ostmann, N. Krumbholz, D. Mittleman, M. Koch, J. Schoebel, and T. Kurner, "Short-range ultra-broadband terahertz communications: Concepts and perspectives," *IEEE Antennas and Propagation Magazine*, vol. 49, no. 6, pp. 24–39, 2007.

[5] J. Federici and L. Moeller, "Review of terahertz and subterahertz wireless communications," *Journal of Applied Physics*, vol. 107, no. 11, p. 111101, 2010.

[6] T. Kleine-Ostmann and T. Nagatsuma, "A review on terahertz communications research," *Journal of Infrared, Millimeter and Terahertz Waves*, vol. 32, pp. 143–171, 2011.

[7] H. Song and T. Nagatsuma, "Present and Future of Terahertz Communications," *IEEE Transactions on Terahertz Science and Technology*, vol. 1, no. 1, pp. 256–263, 2011.

[8] T. Kürner and S. Priebe, "Towards THz Communications-Status in Research, Standardization and Regulation," *Journal of Infrared, Millimeter, and Terahertz Waves*, vol. 35, no. 1, pp. 53–62, 2014.

[9] I. F. Akyildiz, D. M. Gutierrez-Estevez, R. Balakrishnan, and E. Chavarria-Reyes, "LTE-Advanced and the evolution to Beyond 4G (B4G) systems," *Physical Communication (Elsevier) Journal*, vol. 10, pp. 31–60, 2014.

[10] T. Rappaport, J. Murdock, and F. Gutierrez, "State of the art in 60-ghz integrated circuits and systems for wireless communications," *Proceedings of the IEEE*, vol. 99, pp. 1390 –1436, Aug. 2011.

[11] A. H. Azhar, T. A. Tran, and D. O'Brien, "A gigabit/s indoor wireless transmission using mimo-ofdm visible light communications," *IEEE Photonics Technology Letters*, vol. 25, no. 2, pp. 171–174, 2013.

[12] E. Ciaramella, Y. Arimoto, G. Contestabile, M. Presi, A. D'Errico, V. Guarino, and M. Matsumoto, "1.28 terabit/s (32x40 gbit/s) wdm transmission system for free space optical communications," *IEEE Journal on Selected Areas in Communications*, vol. 27, no. 9, pp. 1639–1645, 2009.

[13] A. Prabhakar, "Statement by the Director of the Defense Advanced Research Projects Agency submitted to the US Senate Committee on Appropriations," *Defense Advanced Research Projects Agency, Tech. Rep.*, 2014.

[14] I. F. Akyildiz, E. Chavarria-Reyes, D. M. Gutierrez-Estevez, R. Balakrishnan, and J. R. Krier, "Enabling Next Generation Small Cells Through Femtorelays," *Physical Communication (Elsevier) Journal*, vol. 9, no. 0, pp. 1 – 15, 2013.

[15] K. Wu, J. Xiao, and L. M. Ni, "Rethinking the architecture design of data center networks," *Frontiers of Computer Science*, vol. 6, no. 5, pp. 596–603, 2012.

[16] Y. Katayama, K. Takano, Y. Kohda, N. Ohba, and D. Nakano, "Wireless data center networking with steered-beam mm-wave links," in *Proc. of IEEE Wireless Communications and Networking Conference (WCNC)*, pp. 2179–2184, 2011.

[17] I. F. Akyildiz and J. M. Jornet, "Electromagnetic wireless nanosensor networks," *Nano Communication Networks (Elsevier) Journal*, vol. 1, no. 1, pp. 3–19, 2010.

[18] M. Dragoman, A. A. Muller, D. Dragoman, F. Coccetti, and R. Plana, "Terahertz antenna based on graphene," *Journal of Applied Physics*, vol. 107, pp. 104313–3, 2010.

[19] M. Tamagnone, J. S. Gomez-Diaz, J. R. Mosig, and J. Perruisseau-Carrier, "Reconfigurable Terahertz Plasmonic Antenna Concept Using a Graphene Stack," *Applied Physics Letters*, vol. 101, no. 21, p. 214102, 2012.

[20] L. Vicarelli, M. S. Vitiello, D. Coquillat, A. Lombardo, A. C. Ferrari, W. Knap, M. Polini, V. Pellegrini, and A. Tredicucci, "Graphene Field-effect Transistors as Room-temperature Terahertz Detectors," *Nature Materials*, vol. 11, pp. 865–871, 2012.

[21] J. M. Dubach, D. I. Harjes, and H. A. Clark, "Fluorescent Ion-selective Nanosensors for Intracellular Analysis with Improved Lifetime and Size," *Nano Letters*, vol. 7, no. 6, pp. 1827–1831, 2007.

[22] J. Li, T. Peng, and Y. Peng, "A Cholesterol Biosensor Based on Entrapment of Cholesterol Oxidase in a Silicic Sol-Gel Matrix at a Prussian Blue Modified Electrode," *Electroanalysis*, vol. 15, no. 12, pp. 1031–1037, 2003.

[23] I. E. Tothill, "Biosensors for cancer markers diagnosis," *Seminars in Cell & Developmental Biology*, vol. 20, no. 1, pp. 55–62, 2009.

[24] P. Tallury, A. Malhotra, L. M. Byrne, and S. Santra, "Nanobioimaging and sensing of infectious diseases," *Advanced Drug Delivery Reviews*, vol. 62, pp. 424–437, Mar. 2010.

[25] I. F. Akyildiz and J. M. Jornet, "The Internet of Nano-things," *IEEE Wireless Communications Magazine*, vol. 17, no. 6, pp. 58–63, 2010.

[26] S. Abadal, E. Alarcón, M. C. Lemme, M. Nemirovsky, and A. Cabellos-Aparicio, "Graphene-enabled Wireless Communication for Massive Multicore Architectures," *IEEE Communications Magazine*, vol. 51, no. 11, pp. 137–143, 2012.

[27] J. M. Jornet and I. F. Akyildiz, "Graphene-based Plasmonic Nano-antenna for Terahertz Band Communication in Nanonetworks," *IEEE JSAC, Special Issue on Emerging Technologies for Communications*, vol. 31, no. 12, pp. 685–694, 2013.

[28] C. Han, A. O. Bicen, and I. F. Akyildiz, "Multi-Ray Channel Modeling and Wideband Characterization for Wireless Communications in the Terahertz Band," *IEEE Transactions on Wireless Communications*, vol. 14, no. 5, pp. 2402–2412, 2015.

[29] J. Y. Lee and R. A. Scholtz, "Ranging in a dense multipath environment using an uwb radio link," *IEEE Journal on Selected Areas in Communications (JSAC)*, vol. 20, pp. 1677–1683, Dec. 2002.

[30] S. R. Aedudodla, S. Vijayakumaran, and T. F. Wong, "Timing acquisition in ultra-wideband communication systems," *IEEE Transactions on Vehicular Technology*, vol. 54, no. 5, pp. 1570–1583, 2005.

[31] C. H. Sarantos and N. Dagli, "A photonic analog-to-digital converter based on an unbalanced Mach-Zehnder quantizer," *Optics express*, vol. 18, no. 14, pp. 14598–14603, 2010.

[32] Q. Yang, S. Chen, Y. Ma, and W. Shieh, "Real-time reception of multi-gigabit coherent optical OFDM signals," *Optics express*, vol. 17, no. 10, pp. 7985–7992, 2009.

[33] R. G. Baraniuk, E. Candès, R. Nowak, and M. Vetterli, "Compressive sampling," *IEEE Signal Processing Magazine*, vol. 25, no. 2, pp. 12–13, 2008.

[34] M. Vetterli, P. Marziliano, and T. Blu, "Sampling signals with finite rate of innovation," *IEEE Transactions on Signal Processing*, vol. 50, no. 6, pp. 1417–1428, 2002.

[35] I. Maravic and M. Vetterli, "Sampling and reconstruction of signals with finite rate of innovation in the presence of noise," *IEEE Transactions on Signal Processing*, vol. 53, no. 8, pp. 2788–2805, 2005.

[36] J. Kusuma, A. Ridolfi, and M. Vetterli, "Sampling of communication systems with bandwidth expansion," in *Proc. IEEE International Conference on Communications (ICC)*, vol. 3, pp. 1601–1605, 2002.

[37] V. Y. Tan and V. K. Goyal, "Estimating signals with finite rate of innovation from noisy samples: A stochastic algorithm," *IEEE Transactions on Signal Processing*, vol. 56, no. 10, pp. 5135–5146, 2008.

[38] P. Shukla and P. L. Dragotti, "Sampling schemes for multidimensional signals with finite rate of innovation," *IEEE Transactions on Signal Processing*, vol. 55, no. 7, pp. 3670–3686, 2007.

[39] A. J. Coulson, "Maximum likelihood synchronization for OFDM using a pilot symbol: algorithms," *IEEE Journal on Selected Areas in Communications*, vol. 19, no. 12, pp. 2486–2494, 2001.

[40] U. Mengali, *Synchronization techniques for digital receivers*. Springer Science & Business Media, 2013.

[41] C. Carbonelli and U. Mengali, "Synchronization Algorithms for UWB Signals," *IEEE Transactions on Communications*, vol. 54, no. 2, pp. 329–338, 2006.

[42] F. Rana, "Graphene Terahertz Plasmon Oscillators," *IEEE Transactions on Nanotechnology*, vol. 7, no. 1, pp. 91–99, 2008.

[43] M. Dragoman, A. Muller, D. Dragoman, F. Coccetti, and R. Plana, "Terahertz antenna based on graphene," *Journal of Applied Physics*, vol. 107, no. 10, p. 104313, 2010.

[44] I. Llatser, C. Kremers, A. Cabellos-Aparicio, J. M. Jornet, E. Alarcón, and D. N. Chigrin, "Graphene-based nano-patch antenna for Terahertz radiation," *Photonics and Nanostructures-Fundamentals and Applications*, vol. 10, no. 4, pp. 353–358, 2012.

[45] M. Tamagnone, J. Gomez-Diaz, J. Mosig, and J. Perruisseau-Carrier, "Analysis and design of Terahertz antennas based on plasmonic resonant graphene sheets," *Journal of Applied Physics*, vol. 112, no. 11, p. 114915, 2012.

[46] J. Huang, *Reflectarray Antenna*. Wiley Online Library, 2005.

[47] W. Menzel, D. Pilz, and M. Al-Tikriti, "Millimeter-wave folded reflector antennas with high gain, low loss, and low profile," *IEEE Antennas and Propagation Magazine*, vol. 44, no. 3, pp. 24–29, 2002.

[48] T. Niu, W. Withayachumnankul, B. S.-Y. Ung, H. Menekse, M. Bhaskaran, S. Sriram, and C. Fumeaux, "Experimental demonstration of reflectarray antennas at Terahertz frequencies," *Optics express*, vol. 21, no. 3, pp. 2875–2889, 2013.

[49] E. Carrasco and J. Perruisseau-Carrier, "Reflectarray antenna at Terahertz using graphene," *IEEE Antennas and Wireless Propagation Letters*, vol. 12, pp. 253–256, 2013.

[50] P. Nayeri, M. Liang, R. A. Sabory-Garcia, M. Tuo, F. Yang, M. Gehm, H. Xin, and A. Z. Elsherbeni, "3D printed dielectric reflectarrays: low-cost high-gain antennas at sub-millimeter waves," *IEEE Transactions on Antennas and Propagation*, vol. 62, no. 4, pp. 2000–2008, 2014.

[51] N. Moraitis and P. Constantinou, "Indoor channel measurements and characterization at 60 ghz for wireless local area network applications," *IEEE Transactions on Antennas and Propagation*, vol. 52, no. 12, pp. 3180–3189, 2004.

[52] S. Priebe, M. Kannicht, M. Jacob, and T. Kurner, "Ultra Broadband Indoor Channel Measurements and Calibrated Ray Tracing Propagation Modeling at THz Frequencies," *IEEE Journal of Communications and Networks*, vol. 15, no. 6, pp. 547–558, 2013.

[53] H. J. Song, K. Ajito, A. Wakatsuki, Y. Muramoto, N. Kukutsu, Y. Kado, and T. Nagatsuma, "Terahertz wireless communication link at 300 ghz," in *IEEE Topical Meeting on Microwave Photonics, MWP*, pp. 42–45, Oct. 2010.

[54] Y. Choi, J.-W. Choi, and J. M. Cioffi, "A Geometric-Statistic Channel Model for THz Indoor Communications," *Journal of Infrared, Millimeter, and Terahertz Waves*, pp. 1–12, 2013.

[55] S. Priebe and T. Kurner, "Stochastic modeling of thz indoor radio channels," *IEEE Transactions on Wireless Communications*, vol. 12, no. 9, pp. 4445–4455, 2013.

[56] J. Jornet and I. Akyildiz, "Channel Modeling and Capacity Analysis for Electromagnetic Wireless Nanonetworks in the Terahertz Band," *IEEE Transactions on Wireless Communications*, vol. 10, no. 10, 2011.

[57] R. Piesiewicz, C. Jansen, D. Mittleman, T. Kleine-Ostmann, M. Koch, and T. Kurner, "Scattering analysis for the modeling of THz communication systems," *IEEE Transactions on Antennas and Propagation*, vol. 55, pp. 3002–3009, Nov. 2007.

[58] H. Ragheb and E. R. Hancock, "The Modified Beckmann–Kirchhoff Scattering Theory for Rough Surface Analysis," *Pattern Recognition (Elsevier) Journal*, vol. 40, no. 7, pp. 2004–2020, 2007.

[59] M. Jacob, S. Priebe, R. Dickhoff, T. Kleine-Ostmann, T. Schrader, and T. Kurner, "Diffraction in mm and sub-mm Wave Indoor Propagation Channels," *IEEE Transactions on Microwave Theory and Techniques*, vol. 60, no. 3, pp. 833–844, 2012.

[60] C. Jansen, S. Priebe, C. Moller, M. Jacob, H. Dierke, M. Koch, and T. Kurner, "Diffuse Scattering from Rough Surfaces in THz Communication Channels," *IEEE Transactions on Terahertz Science and Technology*, vol. 1, no. 2, pp. 462–472, 2011.

[61] C. Han and I. F. Akyildiz, "Distance-Aware Multi-Carrier (DAMC) Modulation in Terahertz Band Communication," *Proc. of IEEE International Conference on Communications (ICC)*, 2014.

[62] T. S. Rappaport *et al.*, *Wireless communications: principles and practice*, vol. 2. Prentice Hall PTR New Jersey, 1996.

[63] A. F. Molisch, "Ultrawideband Propagation Channels - Theory, Measurement, and Modeling," *IEEE Transactions on Vehicular Technology*, vol. 54, no. 5, pp. 1528–1545, 2005.

[64] R. C. Qiu, C. Zhou, and Q. Liu, "Physics-based pulse distortion for ultra-wideband signals," *IEEE Transactions on Vehicular Technology*, vol. 54, no. 5, pp. 1546–1555, 2005.

[65] J. M. Jornet and I. F. Akyildiz, "Femtosecond-Long Pulse-Based Modulation for Terahertz Band Communication in Nanonetworks," *IEEE Transactions on Communications*, vol. 62, no. 5, pp. 1742–1754, 2011.

[66] R. C. Daniels and R. W. Heath, "60 ghz wireless communications: emerging requirements and design recommendations," *IEEE Vehicular Technology Magazine*, vol. 2, no. 3, pp. 41–50, 2007.

[67] S. Gezici, Z. Sahinoglu, H. Kobayashi, and H. V. Poor, "Ultra-wideband impulse radio systems with multiple pulse types," *IEEE Journal on Selected Areas in Communications*, vol. 24, no. 4, pp. 892–898, 2006.

[68] Y.-P. Nakache and A. F. Molisch, "Spectral shape of uwb signals-influence of modulation format, multiple access scheme and pulse shape," *IEEE Vehicular Technology Conference*, vol. 4, pp. 2510–2514, 2003.

[69] W. D. Wu, C. C. Lee, C. H. Wang, and C. C. Chao, "Signal-to-Interference-Plus-Noise Ratio Analysis for Direct-Sequence Ultra-Wideband Systems in Generalized Saleh–Valenzuela Channels," *IEEE Journal of Selected Topics in Signal Processing*, vol. 1, no. 3, pp. 483–497, 2007.

[70] T. Keller and L. Hanzo, "Adaptive Multicarrier Modulation: A Convenient Framework for Time-frequency Processing in Wireless Communications," *Proceedings of the IEEE*, vol. 88, no. 5, pp. 611–640, 2000.

[71] K. Sathananthan and C. Tellambura, "Probability of Error Calculation of OFDM Systems with Frequency Offset," *IEEE Transactions on Communications*, vol. 49, no. 11, pp. 1884–1888, 2001.

[72] C. Y. Wong, R. S. Cheng, K. B. Lataief, and R. D. Murch, "Multiuser OFDM with Adaptive Subcarrier, Bit, and Power Allocation," *IEEE Journal on Selected Areas in Communications (JSAC)*, vol. 17, no. 10, pp. 1747–1758, 1999.

[73] H. ElSawy and E. Hossain, "On Stochastic Geometry Modeling of Cellular Uplink Transmission with Truncated Channel Inversion Power Control," *IEEE Transactions on Wireless Communications*, vol. 13, no. 8, pp. 4454–4469, 2014.

[74] D. Cassioli, M. Z. Win, F. Vatalaro, and A. F. Molisch, "Performance of Low-complexity RAKE Reception in a Realistic UWB Channel," in *IEEE International Conference on Communications, ICC*, vol. 2, pp. 763–767, 2002.

[75] T. Schneider, A. Wiatrek, S. Preußler, M. Grigat, and R.-P. Braun, "Link Budget Analysis for Terahertz Fixed Wireless Links," *IEEE Transactions on Terahertz Science and Technology*, vol. 2, no. 2, pp. 250–256, 2012.

[76] S. Gezici, H. Kobayashi, H. V. Poor, and A. F. Molisch, "Performance Evaluation of Impulse Radio UWB Systems with Pulse-based Polarity Randomization," *IEEE Transactions on Signal Processing*, vol. 53, no. 7, pp. 2537–2549, 2005.

[77] C. Lin and G. Y. Li, "Indoor Terahertz Communications: How Many Antenna Arrays Are Needed?," *IEEE Transactions on Wireless Communications*, vol. 14, no. 6, pp. 3097–3107, 2015.

[78] J. Lin and M. A. Weitnauer, "Pulse-level Beam-switching MAC with Energy Control in Picocell Terahertz Networks," in *Proc. IEEE GLOBECOM*, 2014.

[79] C. Han, A. O. Bicen, and I. F. Akyildiz, "Multi-Wideband Waveform Design for Distance-adaptive Wireless Communications in the Terahertz Band," *IEEE Transactions on Signal Processing*, vol. 64, no. 4, pp. 910–922, 2016.

[80] R. G. Cid-Fuentes, J. M. Jornet, I. F. Akyildiz, and E. Alarcón, "A receiver architecture for pulse-based electromagnetic nanonetworks in the terahertz band," in *Proc. of IEEE ICC*, pp. 4937–4942, 2012.

[81] I. Maravic, J. Kusuma, and M. Vetterli, "Low-sampling rate uwb channel characterization and synchronization," *IEEE Journal of Communications and Networks*, vol. 5, no. 4, pp. 319–327, 2003.

[82] J. Kusuma, I. Maravić, and M. Vetterli, "Sampling with finite rate of innovation: channel and timing estimation for UWB and GPS," in *Proc. IEEE International Conference on Communications (ICC)*, vol. 5, pp. 3540–3544, 2003.

[83] H. A. Asl, P. L. Dragotti, and L. Baboulaz, "Multichannel sampling of signals with finite rate of innovation," *IEEE Signal Processing Letters*, vol. 17, no. 8, pp. 762–765, 2010.

[84] I. Maravić and M. Vetterli, "Exact sampling results for some classes of parametric nonbandlimited 2-D signals," *IEEE Transactions on Signal Processing*, vol. 52, no. 1, pp. 175–189, 2004.

[85] Y. Hua and T. K. Sarkar, "Matrix pencil method for estimating parameters of exponentially damped/undamped sinusoids in noise," *IEEE Transactions on Acoustics, Speech and Signal Processing*, vol. 38, no. 5, pp. 814–824, 1990.

[86] H. Miao, K. Yu, and M. J. Juntti, "Positioning for NLOS propagation: Algorithm derivations and Cramer–Rao bounds," *IEEE Transactions on Vehicular Technology*, vol. 56, no. 5, pp. 2568–2580, 2007.

[87] I. Guvenc, S. Gezici, and Z. Sahinoglu, "Ultra-wideband range estimation: Theoretical limits and practical algorithms," in *Proc. of IEEE International Conference on Ultra-Wideband (ICUWB)*, vol. 3, pp. 93–96, 2008.

[88] Z. Tian and G. B. Giannakis, "BER Sensitivity to Mistiming in Ultra-Wideband Impulse Radios-Part I: Nonrandom Channels," *IEEE Transactions on Signal Processing*, vol. 53, no. 4, pp. 1550–1560, 2005.

[89] A. Rajeswaran, V. S. Somayazulu, and J. R. Foerster, "Rake performance for a pulse based UWB system in a realistic UWB indoor channel," in *Proc. of IEEE ICC*, vol. 4, pp. 2879–2883, 2003.

[90] Z. Shen, J. G. Andrews, and B. L. Evans, "Adaptive Resource Allocation in Multiuser OFDM Systems with Proportional Rate Constraints," *IEEE Transactions on Wireless Communications*, vol. 4, no. 6, pp. 2726–2737, 2005.

[91] W. Rhee and J. M. Cioffi, "Increase in Capacity of Multiuser OFDM System Using Dynamic Subchannel Allocation," *Proc. of IEEE Vehicular Technology Conference (VTC)*, vol. 2, pp. 1085–1089, 2000.

[92] Y. J. A. Zhang and K. B. Letaief, "An Efficient Resource-allocation Scheme for Spatial Multiuser Access in MIMO/OFDM Systems," *IEEE Transactions on Communications*, vol. 53, no. 1, pp. 107–116, 2005.

[93] I. C. Wong and B. L. Evans, *Resource Allocation in Multiuser Multicarrier Wireless Systems*. Springer, 2008.

[94] S. T. Chung and A. J. Goldsmith, "Degrees of Freedom in Adaptive Modulation: A Unified View," *IEEE Transactions on Communications*, vol. 49, no. 9, pp. 1561–1571, 2001.

[95] S. Koenig, D. Lopez-Diaz, J. Antes, F. Boes, R. Henneberger, A. Leuther, A. Tessmann, R. Schmogrow, D. Hillerkuss, R. Palmer, *et al.*, "Wireless sub-THz communication system with high data rate," *Nature Photonics*, vol. 7, no. 12, pp. 977–981, 2013.

[96] A. J. Seeds, H. Shams, M. J. Fice, and C. C. Renaud, "Terahertz photonics for wireless communications," *IEEE Journal of Lightwave Technology*, vol. 33, no. 3, pp. 579–587, 2015.

[97] S. Koenig, D. Lopez-Diaz, J. Antes, F. Boes, R. Henneberger, A. Leuther, A. Tessmann, R. Schmogrow, D. Hillerkuss, R. Palmer, *et al.*, "Wireless sub-THz communication system with high data rate enabled by RF photonics and active MMIC technology," in *IEEE Photonics Conference*, 2014.

[98] J. M. Jornet and I. F. Akyildiz, "Graphene-based plasmonic nano-transceiver for Terahertz band communication," in *IEEE European Conference on Antennas and Propagation (EuCAP)*, pp. 492–496, 2014.

[99] S. Falahati, A. Svensson, T. Ekman, and M. Sternad, "Adaptive Modulation Systems for Predicted Wireless Channels," *IEEE Transactions on Communications*, vol. 52, no. 2, pp. 307–316, 2004.

[100] K. B. Letaief and Y. J. Zhang, "Dynamic Multiuser Resource Allocation and Adaptation for Wireless Systems," *IEEE Wireless Communications Magazine*, vol. 13, no. 4, pp. 38–47, 2006.

[101] C. Wang, B. Lu, C. Lin, Q. Chen, L. Miao, X. Deng, and J. Zhang, "0.34-thz wireless link based on high-order modulation for future wireless local area network applications," *IEEE Transactions on Terahertz Science and Technology*, vol. 4, no. 1, pp. 75–85, 2014.

[102] T. Aulin, "A modified model for the fading signal at a mobile radio channel," *IEEE Transactions on Vehicular Technology*, vol. 28, no. 3, pp. 182–203, 1979.

[103] S. Qu and T. Yeap, "A three-dimensional scattering model for fading channels in land mobile environment," *IEEE Transactions on Vehicular Technology*, vol. 48, no. 3, pp. 765–781, 1999.

[104] Y. Z. Mohasseb and M. P. Fitz, "A 3-D spatio-temporal simulation model for wireless channels," *IEEE Journal on Selected Areas in Communications*, vol. 20, no. 6, pp. 1193–1203, 2002.

[105] K. Yasuko and S. Takamasa, "Terahertz-wave propagation model," *Journal of the National Institute of Information and Communications Technology*, vol. 55, no. 1, pp. 73–77, 2008.

[106] E. Torkildson, U. Madhow, and M. Rodwell, "Indoor millimeter wave MIMO: Feasibility and performance," *IEEE Transactions on Wireless Communications*, vol. 10, no. 12, pp. 4150–4160, 2011.

[107] C. Lin and G. Y. Li, "Adaptive Beamforming With Resource Allocation for Distance-Aware Multi-User Indoor Terahertz Communications," *IEEE Transactions on Communications*, vol. 63, no. 8, pp. 2985–2995, 2015.

[108] B. Sensale-Rodriguez, R. Yan, L. Liu, D. Jena, and H. G. Xing, "Graphene for reconfigurable Terahertz optoelectronics," *Proceedings of the IEEE*, vol. 101, no. 7, pp. 1705–1716, 2013.

[109] J. M. Dawlaty, S. Shivaraman, J. Strait, P. George, M. Chandrashekhar, F. Rana, M. G. Spencer, D. Veksler, and Y. Chen, "Measurement of the optical absorption spectra of epitaxial graphene from Terahertz to visible," *Applied Physics Letters*, vol. 93, no. 13, p. 131905, 2008.

[110] E. Carrasco, M. Tamagnone, and J. Perruisseau-Carrier, "Tunable graphene reflective cells for THz reflectarrays and generalized law of reflection," *Applied Physics Letters*, vol. 102, no. 10, p. 104103, 2013.

[111] C. Zhang, C. Han, and I. F. Akyildiz, "Three Dimensional End-to-end Modeling and Directivity Analysis for Graphene-based Antennas in the Terahertz Band," in *Proc. of IEEE Globecom*, 2015.

VITA

Chong Han received the Bachelor of Engineering degree with the highest honor in Electrical Engineering and Telecommunications from The University of New South Wales, Sydney, Australia, in 2011, and received the Master of Science degree in Electrical and Computer Engineering from Georgia Institute of Technology, Atlanta, USA, in 2012. He received the Ph.D. degree in School of Electrical and Computer Engineering from Georgia Institute of Technology, Atlanta, USA, in May 2016, under the supervision of Prof. Ian F. Akyildiz. He is a member of the IEEE. His current research interests include Terahertz band communication networks, Millimeter-wave systems, 5G Cellular Networks, Internet of Things, Internet of Nano-Things, and Electromagnetic Nanonetworks, focusing on channel modeling, physical layer design, and signal processing.